

Monolayer Behavior of Phenolic Lipids: Experimental and Computational Studies

Ying Zhao

A Thesis
in
The Department
of
Chemistry and Biochemistry

Presented in Partial Fulfillment of the Requirements
For the Degree of Master of Science at
Concordia University
Montreal, Quebec, Canada

February 2008

© Ying Zhao, 2008



Library and
Archives Canada

Published Heritage
Branch

395 Wellington Street
Ottawa ON K1A 0N4
Canada

Bibliothèque et
Archives Canada

Direction du
Patrimoine de l'édition

395, rue Wellington
Ottawa ON K1A 0N4
Canada

Your file Votre référence
ISBN: 978-0-494-40995-4
Our file Notre référence
ISBN: 978-0-494-40995-4

NOTICE:

The author has granted a non-exclusive license allowing Library and Archives Canada to reproduce, publish, archive, preserve, conserve, communicate to the public by telecommunication or on the Internet, loan, distribute and sell theses worldwide, for commercial or non-commercial purposes, in microform, paper, electronic and/or any other formats.

The author retains copyright ownership and moral rights in this thesis. Neither the thesis nor substantial extracts from it may be printed or otherwise reproduced without the author's permission.

AVIS:

L'auteur a accordé une licence non exclusive permettant à la Bibliothèque et Archives Canada de reproduire, publier, archiver, sauvegarder, conserver, transmettre au public par télécommunication ou par l'Internet, prêter, distribuer et vendre des thèses partout dans le monde, à des fins commerciales ou autres, sur support microforme, papier, électronique et/ou autres formats.

L'auteur conserve la propriété du droit d'auteur et des droits moraux qui protègent cette thèse. Ni la thèse ni des extraits substantiels de celle-ci ne doivent être imprimés ou autrement reproduits sans son autorisation.

In compliance with the Canadian Privacy Act some supporting forms may have been removed from this thesis.

While these forms may be included in the document page count, their removal does not represent any loss of content from the thesis.

Conformément à la loi canadienne sur la protection de la vie privée, quelques formulaires secondaires ont été enlevés de cette thèse.

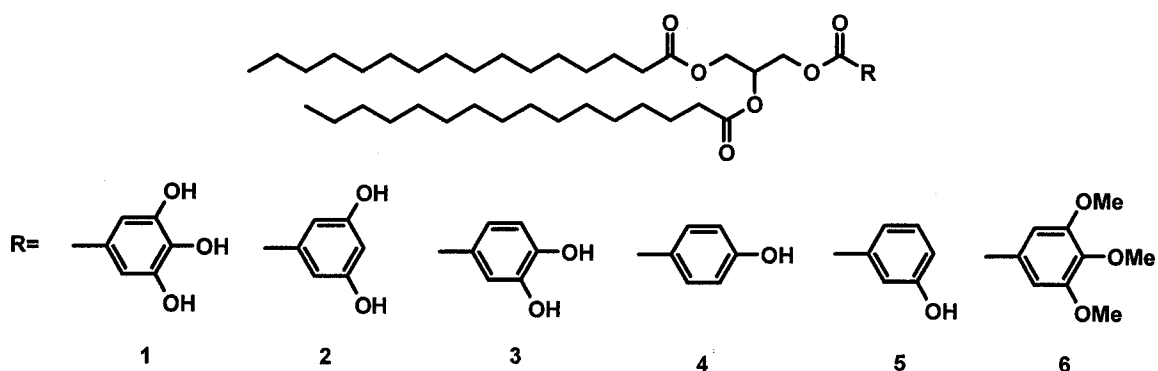
Bien que ces formulaires aient inclus dans la pagination, il n'y aura aucun contenu manquant.


Canada

Abstract

Monolayer Behavior of Phenolic Lipids: Experimental and Computational Studies Ying Zhao

The monolayer and bilayer behavior of 1,2-dipalmitoylgalloylglycerol (DPGG **1**) is thought to be governed by strong intermolecular hydrogen bonding. To probe this hypothesis, monolayers of DPGG and its analogs (**2-5**) with variation in the position and numbers of hydroxyl groups on the aromatic headgroup, and **6**, in which all the hydroxyl groups of **5** were replaced by methoxyl groups in order to disrupt the hydrogen bonds, were studied experimentally and computationally.



It was found that at 25°C, all phenolic lipids formed aggregates at the air/water interface even at very high molecular areas, which suggests strong interactions between the phenolic lipid headgroups. Moreover, isotherms of **2** showed a shift to larger molecular area compared to those of the other phenolic lipids. A *para*-OH group played an important role in the monolayer behavior of the phenolic lipids.

To rationalize the differences in the surface properties of the phenolic lipids that are caused by changing the substitution pattern on the aromatic headgroup, the interactions between small model phenolic esters in the gas phase was studied with

density-functional theory. The carbonyl group involved configuration had the lowest total energy for all the phenolic lipid headgroup dimers. Aggregation of the phenolic lipid headgroups was energetically favorable. The preferred conformation of the full DPGG molecule had two non-interacting side chains, and in order to change into the conformation for the solid state monolayer, in which the two side chains were aligned, an energy barrier of about $5.5 \text{ kcal mol}^{-1}$ needed to be overcome.

Acknowledgement

This thesis would not have been finished without support, guidance and help from my supervisors Dr. Heidi M. Muchall and Dr. Christine E. DeWolf. I thank their encouragement when I was not confident in myself. I thank them for the support on all the conferences I attended. I thank them for giving me a long vacation in summer of 2006. And I thank them for being my referees when I was looking for a job.

I thank Dr. Rolf Schmidt for trainings on Langmuir film balance, Brewster angle microscopy, AFM, endnote, and a lot of other softwares. I also thank him for the fruitful discussions on my project. I am so grateful for his always being around so that whenever I had questions, I could solve them with a timely manner.

I thank Lei Zhang, Elena Ivanova, Dr. Quadir K. Timerghazin, Dr. Robert Mawhinney, Dr. Denise Koch, Pratibha Malla, Petrina Kamya for their help on computational chemistry know-how. Without all their help, I would not have obtained that many results from the computational simulations. I also thank Erick Gonzalez and Nancy Austin for their help on lab instrument setups.

I thank my committee members, Dr. Gilles H. Peslherbe and Dr. Louis A. Cuccia for their questions and their comments, as well as their encouragements on my work. It was their questions that forced me thinking while I was working.

I thank Dr. Sébastien Robidoux for his training on NMR instrument.

I thank Dr. Ann M. English for the convenience she provided to me to use FTIR and MS.

I thank my boss at Nanometrix Inc., Mr. Juan Schneider, for the convenience he provided to me to correct my thesis and meet with my supervisors while I was working.

Table of Contents

Chapter 1. Introduction.....	1
1.1. 1,2-Dipalmitoylglycerol (DPGG) and Langmuir Monolayers.....	1
1.2. Hydrogen Bonding	7
1.3. Computational Chemistry in the Study of Monolayers and Hydrogen Bonding ...	10
1.4. Objectives.....	14
Chapter 2. Methods	17
2.1. Instruments.....	17
2.1.1. Langmuir Film Balance	17
2.1.2. Brewster Angle Microscopy (BAM)	18
2.2. Method and Materials for the Monolayer Study	20
2.3. Spectroscopy	20
2.4. Calculations.....	21
Chapter 3. Monolayer Behavior of Phenolic Lipids: Experimental Study.....	22
3.1. Introduction	22
3.2. Influence of Headgroup Structure on the Monolayer Behavior of Phenolic Lipids	23
3.2.1. Monolayer Behavior of Phenolic Lipids at 25 °C.....	23
3.2.1.1. Isotherms.....	23
3.2.1.2. BAM images	27
3.2.2. Monolayer Behavior of Phenolic Lipids at 38 °C.....	30
3.2.2.1. Isotherms.....	30
3.2.2.2. BAM Images.....	32

3.3. Comparison of the Monolayer Behavior of the Enantiomerically Pure DPGG with Racemic DPGG	35
3.4. Conclusions	41
Chapter 4. Spectroscopic, Computational and Experimental Study on the Phenolic	
Lipids: from Solution to the Air/Water Interface.....	42
4.1. Introduction	42
4.2. Results and Discussion.....	43
4.2.1. Monolayer Behavior of Phenolic Lipids upon Equilibration.....	43
4.2.2. IR Study	48
4.2.3. NMR Study	50
4.2.4. Preference of Aggregation	54
4.2.5. Preference of Hydrogen Bonding to Like Molecules or Water	55
4.3. Conclusions	57
Chapter 5. Computational Investigation of Small Assemblies of Substituted Model	
Phenols	58
5.1. Introduction	58
5.2. Selection of Model Chemistry	58
5.2.1. Comparison of Calculated Spectroscopic Properties and Geometry Information with Available Experimental Data	59
5.2.2. Location of Intermolecular and Intramolecular Hydrogen Bonds.....	65
5.3. Small Assemblies of Model Phenolic Esters	71
5.3.1. Headgroup Structure in Model Methyl Esters	72
5.3.2. Dimers.....	75

5.3.2.1. Methyl Esters	76
5.3.2.2. Propyl and Hexyl Esters.....	80
5.3.3. Trimers	80
5.3.3.1. Methyl Esters	82
5.3.3.2. Propyl and Hexyl Esters.....	84
5.4. Comparison between the Configurations of Dimers and Trimers Obtained from PM3 and B3LYP/6-31G(d)	87
5.5. Simulation of the Entire DPGG Molecule	90
5.5.1. Construction of DPGG.....	90
5.5.2. Verification of Stabilising Interactions.....	94
5.6. Conclusions	97
Chapter 6. Conclusions and Future Work	99
6.1. Conclusions	99
6.2. Future Work	100
Appendix A. BAM Images (Refer to the Attached CD)	107
Appendix B. Tables for Model Chemistry Selection.....	115
Appendix C. Internal Coordinates, Total Energies and Free Energies for Benchmark Molecules (Refer to the Attached CD)	123
Appendix D. Total Energy, Free Energy and Configurations for Model Ester Dimers and Trimers	124
Appendix E. Z-Matrix Files for Dimers and Trimers for Model Esters (Refer to the Attached CD)	144

Appendix F. Sample Calculation of the Energy Cost to Erect the Side Chains for the	
Phenolic Lipids	145

List of Figures

Figure 1. Molecular structure of DPGG.....	1
Figure 2. Molecular structure of DPPC and DPPE.....	3
Figure 3. Schematic presentation of a compression isotherm.....	5
Figure 4. Contour plot of the electron density for two hydrogen-bonded water molecules.	14
Figure 5. Chemical structures of phenolic lipids (n-hydroxybenzoic acids) (1-5) and the methoxy substituted analog (6).....	15
Figure 6. Schematic diagram of a Langmuir film balance.....	17
Figure 7. Schematic diagram of Brewster angle microscopy.	19
Figure 8. Schematic illustration of the reflection change before and after spreading of a monolayer.	19
Figure 9. π -A Isotherms of phenolic lipids on water at 25°C.....	26
Figure 10. BAM images of phenolic lipids (as indicated) at different surface pressures.	28
Figure 11. Temperature effect on phenolic lipid monolayers.....	31
Figure 12. BAM images of phenolic lipids at 38°C.....	33
Figure 13. Molecular structure of HETA.....	34
Figure 14. Isotherms of enantiomerically pure and racemic DPGG at 25°C.....	36
Figure 15. BAM images of enantiomerically pure DPGG and racemic DPGG at 25°C..	37
Figure 16. Morphology changes in the monolayer of enantiomerically pure DPGG with increasing equilibration time.	38
Figure 17. Effect of equilibration on monolayer behavior of enantiomerically pure DPGG.....	39

Figure 18. BAM images of enantiomerically pure DPGG with 10 minutes of equilibration at different surface pressures.	40
Figure 19. BAM images of enantiomerically pure DPGG at different surface pressures at 33°C.	40
Figure 20. π -A isotherms and BAM images of racemic DPGG monolayer with and without 16 hours of equilibration.....	45
Figure 21. Typical BAM image of DP-3,4,5-MBG (6) after 16 hours of equilibration. .	46
Figure 22. π -A isotherms and BAM images of DP-3,4,5-MBG monolayer with and without 45 hours of equilibration.....	47
Figure 23. IR spectra of DP-3,5-HBG (3) (2 mM).	49
Figure 24. ^1H NMR spectrum of DPGG (8 mM in CDCl_3).	51
Figure 25. ^1H NMR spectrum of DPGG.	51
Figure 26. ^1H NMR spectrum of the OH signal of DPGG at different concentrations. ...	52
Figure 27. Dimer and trimer configuration for 3,4,5-OH-Me most likely to occur at the air water interface optimized with B3LYP/6-31G(d).	54
Figure 28. The choices for a phenol molecule to hydrogen bond with another phenol molecule or with a water molecule.	56
Figure 29. The choices for a <i>p</i> -hydroxy benzoic acid hexyl ester molecule to hydrogen bond with another ester molecule or with a water molecule.	56
Figure 30. Relative differences between the calculated and experimental geometrical parameters for phenol.	60
Figure 31. Relative differences between the three calculated and experimental rotational constants for phenol for various model chemistries.	61

Figure 32. Orientation of the two phenol monomers in the dimer from ref. 75.	62
Figure 33. Relative differences between the calculated and experimental geometrical parameters of the phenol dimer.	62
Figure 34. Relative differences between experimental and calculated rotational constants for the phenol dimer.....	63
Figure 35. Relative orientation of phenol and water molecules in the complex.....	64
Figure 36. Relative differences between the calculated and experimental geometrical parameters and three rotational constants for the phenol–water complex.....	64
Figure 37. Proposed phenol trimer configuration by Mikami et al. from ref. 77.	65
Figure 38. The network of bonding interactions (molecular graph) for phenol, the phenol dimer and catechol from B3LYP/6-31G(d).	66
Figure 39. Relative difference between phenol monomer and dimer atomic properties (H12) calculated with different model chemistries.....	68
Figure 40. The hydrogen bonded isomer of catechol (left) and its rotamer (right).	70
Figure 41. Relative difference between atomic properties of catechol and its isomer calculated with different model chemistries.	70
Figure 42. Possible conformers for two–OH and three–OH headgroup systems.	72
Figure 43. Energy differences for methyl ester conformations with the methyl group <i>trans</i> (left) or <i>cis</i> (right) to the aromatic ring.	73
Figure 44. Methyl ester conformers for molecules with one OH group.	74
Figure 45. Methyl ester conformers for molecules with two OH groups.	74
Figure 46. Methyl ester conformers for the molecule with three OH groups.	75
Figure 47. Dimer configurations for 3-OH-Me and 4-OH-Me.	77

Figure 48. Dimer configurations for 3,4-OH-Me, 3,5-OH-Me and 3,4,5-OH-Me.	79
Figure 49. Dimer configurations for 3,4,5-OH-Me(c) (left) and 3,5-OH-Me(b) (right). .	80
Figure 50. Trimer configurations for 3-OH-Me and 4-OH-Me.	82
Figure 51. Trimer configurations for 3,4-OH-Me and 3,5-OH-Me.	83
Figure 52. Trimer configurations for 3,4,5-OH-Me.	84
Figure 53. Chain length and conformation effect on the relative energy change of 3,4-OH trimers.	85
Figure 54. Geometrical change in 3,4,5-OH-alkyl (a and b in Figure 52) with extending of the side chain from one to six carbon atoms.	85
Figure 55. Relative energy changes due to side chain length increase in 3,4,5-OH-alkyl(a) and (b).	86
Figure 56. Conformation change of one <i>para</i> -OH group in 3,4,5-OH-Me trimers (a) left and (d) right.	87
Figure 57. Constituent parts of the DPGG molecule.	91
Figure 58. Relative energies (kcal mol ⁻¹) for the 180° and 90° conformations of 3,4,5- OH-Et from B3LYP/6-31G(d).	91
Figure 59. Potential energy profile for a twist of the O1-C1-C2-O2 torsional angle in DPGG from B3LYP/6-31G(d).	93
Figure 60. DPGG conformations from B3LYP/6-31G(d) and PM3.	93
Figure 61. Molecular graphs for the 3,4,5-OH-Me monomer and its dimer 3,4,5-OH- Me(b).	95
Figure 62. C-H...H and/or C=O...H interactions in a 3,4,5-OH-Pr dimer and a shortened DPGG molecule.	96

List of Tables

Table 1. Summary of the typical bond energy (kcal mol ⁻¹), bond distance (Å) and angle (degrees) of hydrogen bonds for A-H...B from refs. 10 and 11.....	8
Table 2. Chemical shifts δ (ppm) and integration ratios for the hydroxyl protons in the phenolic lipids at different concentrations in CDCl ₃	53
Table 3. Electron density ρ (au) and Laplacian $\nabla^2\rho$ (au) at the bond critical point of the O-H12...O interaction in the phenol dimer calculated with different model chemistries	67
Table 4. Electron density ρ (au) and Laplacian $\nabla^2\rho$ (au) at the bond critical point of the intramolecular hydrogen bond in catechol calculated with different model chemistries	69
Table 5. Relative energies (kcal mol ⁻¹) for chain lengths of increasing size for 3,4,5-OH-alkyl dimers calculated with B3LYP/6-31G(d).....	81
Table 6. Relative energies (kcal mol ⁻¹) for dimers of 3,4,5-OH-Me from B3LYP/6-31G(d) and PM3..	88
Table 7. Relative energies (kcal mol ⁻¹) for trimers of 3,4,5-OH-Me from B3LYP/6-31G(d) and PM3..	89
Table 8. Relative energies (kcal mol ⁻¹) for trimers of 3,4,5-OH-Hex from B3LYP/6-31G(d) and PM3.	90
Table 9. Electron density ρ (au) and Laplacian $\nabla^2\rho$ (au) at selected bond critical points for the weak interactions in the 3,4,5-OH-Me dimer..	95

List of Symbols

A	Molecular area
E	Total energy or atomic energy
ΔE	Relative energy
G	Free energy
ΔG	Relative free energy
ΔH	Relative enthalpy
M	Dipolar polarization
n	Refractive index
N	Atomic population
<i>p</i>	<i>para</i>
p	Pressure
q	Charge
r_H	Radius of hydrogen atom involved in hydrogen bond
r_O	Radius of oxygen atom involved in hydrogen bond
T	Temperature
T_m	Temperature for “gel-to-lamellar” transition
α	Angle of incidence
β	Angle of refraction or the angle between O(H ₂ O)-O(phenol) and the median of the angle HOH (water)
δ	Chemical shift
ϕ	Angle between O(H ₂ O)-O(phenol) and H on the OH of phenol

k	Boltzmann constant
λ	Wavelength
ν	Stretching vibration
π	Surface pressure
γ	Surface tension of a surface after spreading of a monolayer or Angle between C-O(phenol) and O(H ₂ O)
γ_0	Surface tension of clean surface
$\rho(r)$	Electron density
$\nabla^2\rho(r)$	Laplacian of the electron density

List of Abbreviations

AIM	Atoms in molecules
BAM	Brewster angle microscopy
B3LYP	Becke's three parameter hybrid exchange/Lee-Yang-Parr correlation functional
BCP	Bond critical point
DFT	Density-functional theory
DHO	Dihydroxyoctadecanoate
DLPC	1,2-Dilignoceroyl-glycerol-3-phosphacholine
DMSO	Dimethyl sulfoxide
DPGG	1,2-Dipalmitoylgalloylglycerol
DP-3-HBG	Dipalmitoyl-3-hydroxybenzoylglycerol
DP-4-HBG	Dipalmitoyl-4-hydroxybenzoylglycerol
DP-3,4-HBG	Dipalmitoyl-3,4-dihydroxybenzoylglycerol
DP-3,5-HBG	Dipalmitoyl-3,5-dihydroxybenzoylglycerol
DP-3,4,5-MBG	Dipalmitoyl-3,4,5-methoxybenzoylglycerol
DPPC	1,2-Dipalmitoylphosphatidylcholine
DPPE	1,2-Dipalmitoylphosphatidylethanolamine
DTGS	Deuterated triglycine sulfate
FT-IR	Fourier transform infrared
G	Gaseous phase
H-bond	Hydrogen bond
HETA	N-(β -hydroxyethyl)tridecanoic acid amide

Hex	Hexyl
HF	Hartree-Fock
C	Condensed phase
LE	Liquid expanded phase
IR	Infrared
Me	Methyl
MP2	Møller-Plesset perturbation theory of second order
NBD	7-Nitro-2-1,3-benzoxadiazol-4-yl
NMR	Nuclear Magnetic Resonance
OH	Hydroxyl
PBE	Perdew-Burke-Ernzerhof
<i>p</i> -polarized	Plane polarized
PE	Phosphatidylethanolamine
PES	Potential energy surface
PM3	Parameterized Method number 3
Pr	Propyl
RCP	Ring critical point

Chapter 1. Introduction

1.1. *1,2-Dipalmitoylgalloylglycerol (DPGG) and Langmuir Monolayers*

DPGG, which was first synthesised and characterised by Pollastri et al.¹ in 2000, is a diacyl glycerol-based lipid with a phenolic headgroup. The molecular structure of DPGG is as shown in Figure 1.

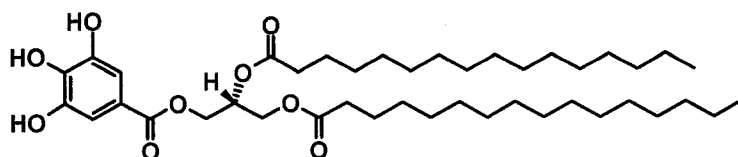


Figure 1. Molecular structure of DPGG.

As a recently synthesised molecule, the properties of DPGG are not well understood, and its potential uses are still being explored.¹ Its structure as a combination of lipid with gallic acid headgroup suggests it can be used in some of the applications of surfactants and polyphenols.

The first application of surfactants can be traced back to at least 2300 years ago,² and now main applications of surfactants lie in the field of detergency, emulsification, lubrication, petroleum recovery and pharmaceuticals. The properties and applications of surfactants are determined by the balance between the hydrophilic and hydrophobic portions of the molecules. Therefore, a surfactant may perform well in some applications but less well in some others depending on their surface tension reducing capability, foaming capacity, solubility in different solvents, detergency power, and critical micelle concentration.² As a water-insoluble surfactant, DPGG can form Langmuir monolayers at

the air/water interface, and monolayers and multilayers of DPGG can be transferred onto different substrates, such as mica, glass or silica, to be further characterized by surface chemistry. The property of DPGG as a surfactant also suggests that it can be used to tether biological molecules to different substrates for study and medical uses.³

In addition, as a compound with more than one hydroxyl group attached to an aromatic ring, a monolayer of DPGG can resemble the surface of polyphenol. Polyphenols are known to have synthetic, medicinal and industrial value as they can prevent the formation of free radicals in biological systems,^{4, 5} chelate metal ions⁶ and bind with biological molecules, such as proteins.⁶

DPGG has a variety of potential uses. Proposed applications for DPGG so far include bio-sensing applications and biocompatible coatings.¹

Before we can make good use of this synthetic lipid, we first need to understand its properties. Bilayer properties for DPGG were studied by Pollastri et al.¹ and were compared with those of 1,2-dipalmitoylphosphatidylcholine (DPPC) and 1,2-dipalmitoylphosphatidylethanolamine (DPPE), which are molecules having the same side chains and glycerol backbones but different headgroups from DPGG (the structures of DPPC and DPPE are shown in Figure 2). DPGG bilayers showed a very narrow fluid separation and a very high T_m (69.3°C) for the “gel-to-lamellar” transition.¹ While the narrow fluid separation was explained by interbilayer hydrogen bonding via water bridges, the high T_m was explained by potential lateral H-bonding (hydrogen-bonding) between the neighboring DPGG molecules. The main endothermic transition for DPGG occurring at high temperature means that there are strong attractive interactions between neighboring molecules that fight against the expansion of the monolayers, and hence require high

energy to break them. Most membrane lipids with the same side chains have much lower T_m than DPGG, for example, T_m for DPPC is only 41°C .¹ DPGG and other molecules, including some cerebrosides and phosphatidylethanolamines (PEs), that exhibit high T_m , have one thing in common: the ability to form hydrogen bonds between neighboring molecules. As DPGG has hydroxyl groups on its headgroup, the strong attractive lateral interactions between DPGG neighboring molecules are most likely hydrogen bonds.¹

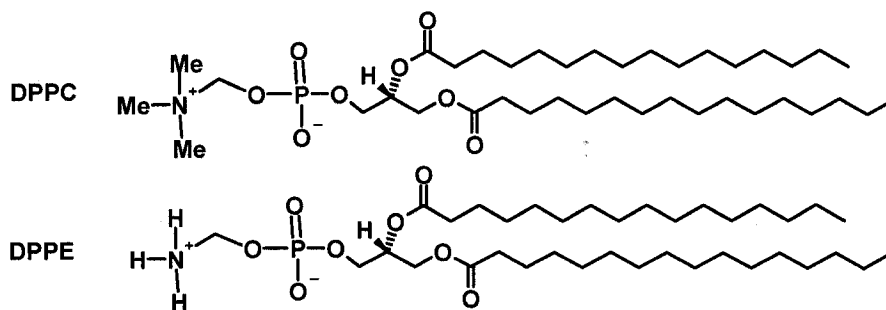


Figure 2. Molecular structure of DPPC and DPPE.

Lateral H-bonding can be systematically studied using a Langmuir monolayer model system. A Langmuir monolayer is an insoluble layer of an organic material, with thickness of one-molecule, spread onto an aqueous subphase with the hydrophilic groups oriented towards the water phase and the hydrophobic chains oriented towards the air phase.

When a monolayer is spread onto the air/water interface, there is a decrease of surface tension because the amphiphiles orient with the hydrophilic parts in water and the hydrophobic part in air, which is energetically favorable and less water molecules have to be present at the surface. The surface pressure (π) of a Langmuir monolayer is the

lowering of surface tension due to the presence of a Langmuir monolayer and can be obtained by the following equation:⁷

$$\pi = \gamma_0 - \gamma$$

where γ_0 is the surface tension of the clean surface and γ is the surface tension of the surface after spreading of a monolayer.

The variation of surface pressure (π) with the surface area (A) is represented by π - A isotherms. π - A isotherms can be regarded as the two-dimensional equivalent of the p - V curves for three dimensional systems. When a three-dimensional gas is compressed, it condenses into a liquid and then into a solid. Each phase is progressively less compressible, with changes in the extent of ordering. Similarly, a pseudo two-dimensional film (monolayer) also shows different physical states depends on the ordering of the constituent molecules, which in turn depends on lateral forces between the constituent molecules. Besides interactions between the headgroups of the molecules, the most common lateral forces between molecules are non van der Waals forces between the chains, which are maximized when neighboring molecules align with one another. Although van der Waals forces are weak, chains with 8-20 or more carbon atoms can contribute as much as tens of kilojoules per mole to the interaction.⁸ The three general states of monolayers, namely the gaseous, liquid expanded and condensed phases, are illustrated in the schematic π - A isotherm in Figure 3.

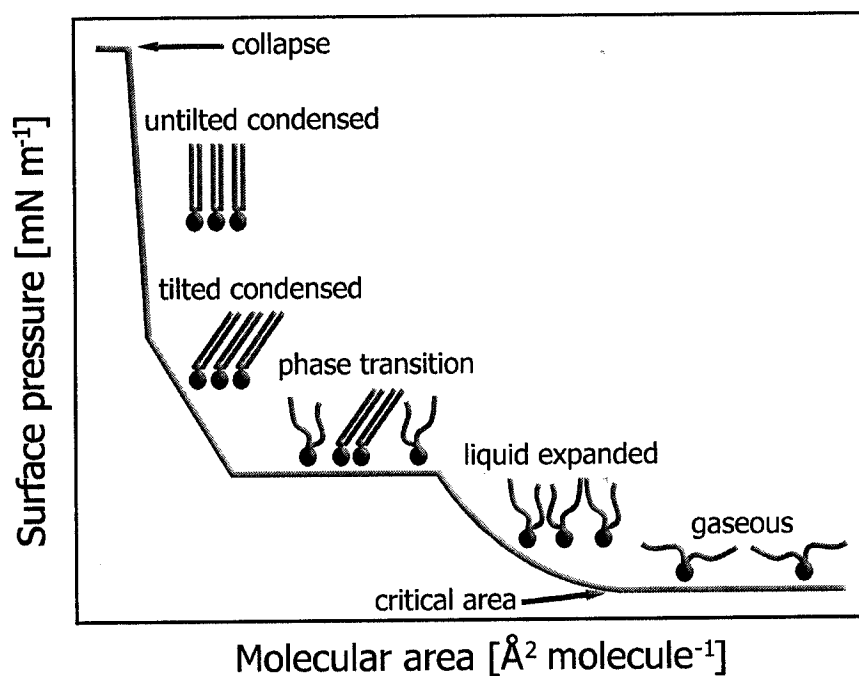


Figure 3. Schematic presentation of a compression isotherm.

At large molecular areas, the constituent molecules of a monolayer are considered to be far away from each other so that interactions between them are negligible. Therefore, constituent molecules can move about the surface separately and independently. Ideal gaseous films, which consist of molecules of negligible size without any lateral adhesion between them, obey an ideal gas law for two-dimensional systems, $\pi \cdot A = \kappa \cdot T$ (where κ is the Boltzmann constant). In this case, the π -A curve would be a rectangular hyperbola.⁷

Compression of gaseous state monolayers can result in a transition from gaseous phase to liquid expanded (LE) phase. The transition, however, occurs at such low pressures that a phase transition plateau corresponding to the coexistence of these two phases is not discernable in Figure 3. At the end of the gaseous phase to LE transition,

monolayers show significant increase in surface pressure with the decrease of surface area. Therefore, the point at which the pressure begins to rise discernibly is known as the critical area of the monolayer. Liquid expanded films are fluid and coherent, with the average distance between molecules much larger than those for bulk liquids.⁹

Unlike the transition from gaseous phase to LE phase which takes place at very low pressure, the transition from LE to condensed (C) phase can occur at higher surface pressures and usually appears as a plateau on the π -A isotherm (refer to Figure 3). During the transition, molecules start to pack closely, and eventually when the monolayer reaches the condensed phase, the surface pressure begins to increase rapidly. In condensed monolayers, with the decreasing of surface area occupied by each constituent molecule, the monolayer has to gradually reduce the tilt angle of the side chains of its constituent molecules, and the physical state of the monolayer can eventually turn from a tilted condensed phase to an untilted condensed phase. Molecules in an untilted condensed film pack closely. It is observed that for straight-chain fatty acids, each molecule occupies a limiting area of 0.20-0.22 nm² at the air/water interface.⁷ Compression beyond the limiting area will cause collapse or buckling of the film. It is noteworthy that some monolayers may show direct transition from gaseous phase to condensed phase, or only show gaseous phase and liquid expanded phase (a condensed phase cannot be achieved).

As mentioned above, the physical state of a monolayer depends on the lateral cohesive forces between the constituent molecules, which in turn depend on the geometry and orientation of the molecules. The following factors will, in principle, favor the

formation of a LE film: 1) bulkier headgroups; 2) more than one polar group; 3) not all-trans hydrocarbon chains; 4) branched hydrocarbon chains.⁷

The monolayer behavior of DPGG has been studied by Schmidt et al.³ with a Langmuir monolayer model system. Many unusual properties were observed for DPGG compared to common phospholipids, such as DPPC, including the formation of aggregates at high molecular areas, an increase in surface pressure at constant surface area, slow film equilibration, an extreme surface pressure gradient, and high film rigidity. All the unusual properties of the DPGG monolayer led to the proposition of a lateral H-bonding network between DPGG headgroups.

1.2. Hydrogen Bonding

Hydrogen bonding plays an important role in chemistry and biology. Since it was first described in 1902 by Werner¹⁰ and first termed as "hydrogen bond" in 1931 by Pauling,¹¹ research in hydrogen bonding for various has boomed. By definition, a hydrogen bond is a hydrogen atom involved in a donor-acceptor attractive interaction.¹¹
¹² Although the strength of hydrogen bonds is moderate (between the range of covalent bonds and van der Waals interactions), they are sufficient to direct molecular assembly. They are directional and reproducible.¹⁰ Hydrogen bonds are classified, by Jeffery in 1997,¹¹ into strong, moderate and weak H-bonds. Table 1 summarises the parameters for strong, moderate and weak hydrogen bonds.^{10, 11}

Molecules with the ability to form hydrogen bonds can form monolayers. Although it is commonly accepted that the domain shape of a condensed phase of a monolayer is principally governed by the competition between dipole-dipole interactions and line

tension,¹³ the situation becomes more complicated when hydrogen bonds are involved. Numerous groups have studied hydrogen bonding between the headgroups of the amphiphiles in monolayer systems, some of them have studied the H-bonding between the amphiphile headgroups computationally.

Table 1. Summary of the typical bond energy (kcal mol⁻¹), bond distance (Å) and angle (degrees) of hydrogen bonds for A-H...B from refs. 10 and 11.

Bond Parameter	Strong hydrogen bonds	Moderate hydrogen bonds	Weak hydrogen bonds
Bond energy	15-40	4-15	<4
H...B	1.2-1.5	1.5-2.2	2.2-3.2
A...B	2.2-2.5	2.5-3.2	3.2-4.0
$\theta(\text{A-H}\cdots\text{B})$	175-180	130-180	90-150
Example	$[\text{N}\cdots\text{H}\cdots\text{O}]^+$	$\text{O-H}\cdots\text{O-H}$	$\text{C-H}\cdots\text{O}$

Wang et al.¹⁴ studied methyl and ethyl esters of 2,3-dihydroxy fatty acids. They suggested that the observed elongated aggregates were caused by directional intermolecular H-bonds. The FT-IR spectrum of the monolayer transferred at 22 mN m⁻¹ showed a band appearing at 1728 cm⁻¹ corresponding to the C=O bond stretching vibration, while this band appeared at 1737 cm⁻¹ for the amphiphile in chloroform solution, which suggested the existence of intermolecular hydrogen bonding between the headgroups of neighboring molecules in the transferred monolayer. Differences in the morphology caused by both changing the side chain length and the headgroup structure were explained by the competition between the intermolecular hydrogen bonding and the

van der Waals interaction in the domination of the aggregation process. That is, when hydrogen bonds dominated, elongated domains were formed, while when van der Waals interactions were dominant, rigid and large aggregates were formed, which happened with the molecules with longer side chains (16 carbon atoms).

Chen et al.¹⁵ studied the monolayer behavior of 2,3-disubstituted methyl octadecanoate computationally. Monolayers were built by allowing maximum H-bonding between the headgroups. It was found that the methyl-2,3-dihydroxyoctadecanoate (DHO) molecules can hydrogen bond with up to four like molecules since a hydroxyl group can serve as both proton acceptor and proton donor, which results in the formation of a 2D H-bond network. The intermolecular H-bond between DHO molecules stabilise the aggregates by balancing steric repulsions, leading to a stable DHO monolayer which was observed experimentally. When one of the hydroxyl groups on DHO is replaced by a fluorine, the balance between the H-bonding and the steric repulsion was broken since fluorine can only act as a proton acceptor, hence the resulting monolayer is less stable. 3D collapse structure was observed experimentally by BAM for the fluorine replaced molecules.

Dreger et al.¹⁶ studied the influence of the position of a methyl group on the monolayer stability of methyl octadecanoates with amide groups integrated into the alkyl chain. They simulated the headgroup of the amphiphiles in density-functional theory (DFT) calculations. They claimed that in the LE phase, the amide group of the amphiphile formed two hydrogen bonds with subphase water molecules, while in the condensed phase, the amides formed one hydrogen bond with subphase water molecule and an intermolecular hydrogen bond with a like amphiphile. Therefore, by rotating the

headgroup along the N-C bond, the enthalpy difference between the LE and condensed phase conformers was calculated. The sequence of enthalpy differences (ΔH) calculated for four methyl-substituted octadecanoates agreed well with experimental results.

Thirumoorthy et al.¹³ studied the influence of electrostatic interactions on the domain shapes of monoglycerol amphiphiles with different headgroup, including monoglycerol amide, ether, ester and amine. They claimed that the variations in headgroup structure change domain shapes drastically and electrostatic interactions play an important role in the mesoscopic domain sizes and shapes. Ab initio calculations based on the Hartree-Fock (HF) method were employed in their work to optimize monomer and dimer configurations of the amphiphiles and to study their dimerisation energy. They found the dimerisation energy to follow the sequence of ether < ester < amine < amide, which explained well, except for the amine, the domain shape for the monoglycerol amphiphiles observed experimentally. The high dimerisation energy for the amine was explained by the enhanced importance of intermolecular hydrogen bonding.

These examples suggest that a systematic study can be used to probe the H-bonding between DPGG headgroups, and a computational study will be useful in understanding the H-bonding patterns between the headgroups.

1.3. Computational Chemistry in the Study of Monolayers and Hydrogen Bonding

With the availability of supercomputers, computational chemistry is becoming a more and more useful and reliable tool in studying structures, energies and physical properties of systems of various sizes. With a proper selection of model systems,

researchers have solved many complicated problems that have not yet been solved experimentally. For example, the geometry of N-sulfinylamines ($R-N=S=O$) has drawn researchers' interest for a long time¹⁷⁻²⁰ Several compounds in this family have finally been confirmed as being syn-configured experimentally by X-ray diffraction.²¹ In a computational study on aromatic N-sulfinylamines with ortho hydrogen atoms, intramolecular C-H \cdots O anti-hydrogen bonds between the NSO and the ortho hydrogen atom were found, characterised by a shortening of the C-H bond and a blue shift of its stretching frequency.²² Experimental evidence for this weak interaction is not yet available.

In recent years, great efforts have been put in the simulation of lipid monolayers. Traditional simulation of monolayers was done by molecular dynamics simulations using coarse-grained models.²³ The amphiphiles are modelled as stiff chains with a rod-like part attached to a head segment, free to move in lateral directions but confined into a planar surface by a harmonic potential.²³ The coarse-grained model, developed by Feller et al., was used to simulate two lipid monolayers separated by a layer of water. The thickness of the water layer was chosen so that little interaction was anticipated between the two monolayers.²⁴ Larson et al. modified the model developed by Feller and co-workers by applying a wall potential instead of using a bilayer, with side chains of the amphiphiles interacting with each other.²⁴ This model was also adopted by Alper et al. in a simulation of a DMPC monolayer.^{25, 26}

Molecular dynamics simulations, however, cannot give insight into the detailed interactions between the side chains or the headgroups of the amphiphiles. In order to study how changing the headgroup structure influences the surface behavior of the

amphiphilic molecules, electronic structure methods are needed. Electronic structure methods are based on quantum mechanics. By solving the Schrödinger equation ($H\Psi = E\Psi$), the energy and related properties of a molecule can be obtained.²⁷ The exact solution of the Schrödinger equation, however, is not possible for multi-electron molecules. Electronic structure methods therefore make compromises between computational accuracy and cost by using approximations.²⁷ The methods using experiment-derived parameters are known as semiempirical methods (e.g. Parameterized Method number 3 - PM3) and those using only physical constants are called ab initio methods (e.g. Hartree-Fock-HF, Møller-Plesset Perturbation theory of second order - MP2). Methods from density-functional theory (e.g. Becke's three parameter hybrid exchange/Lee-Yang-Parr correlation functional - B3LYP) compute the energy as a function of the electron density²⁷ and have become popular because they often have the accuracy of more sophisticated ab initio methods at a much lower computational cost.

Electronic structure theory is widely used in the simulation of monolayers of amphiphiles. Besides the studies on hydrogen bonding in monolayers by Dreger et al.,¹⁶ Thirumoorthy et al.¹³ and Chen et al.¹⁵ as summarised in section 1.2, computational simulations were also used in studying the thermodynamic characteristics of monolayers. Vysotsky et al. simulated 2D cluster formation with 2-7 monomers of fatty alcohols with 8-16 carbon-atom side chains using the semiempirical method PM3.²⁸ They found that the calculated enthalpy, entropy and Gibbs' free energy had a linear relationship with the number of methylene groups in the alcohol. A thermodynamic model was established based on the assumption of an equilibrium between the oligomers (dimers to tetramers) and larger clusters. The calculated results agreed very well with the experimental ones.

They suggested that the liquid state of a monolayer was made up of monomers and oligomers, and that the aggregation degree increased with an increase of the chain length. Vysotsky et al. also simulated the formation of 2D⁺ clusters (dimers to tetramers) of carboxylic acids (5-15 carbon atoms in the chain) at the air/water interface using semiempirical methods, and calculated geometries and thermodynamic characteristics.²⁹ They found that spontaneous aggregation could take place for chains larger than 13 carbon atoms, while for less than 11, decomposition of the aggregates was energetically favorable. When the chains contain 8 to 13 carbon atoms, the formation of trimers was most likely to occur.

For the identification and characterisation of hydrogen bonds, the quantum theory of Atoms in Molecules (AIM) is a powerful tool.³⁰ It has been successfully used to characterise H-bonds varied in strength in a wide variety of molecular systems.³¹⁻³⁸ With AIM, the topology of the electron density (ρ) is analysed. A hydrogen bond is identified through the presence of a “bond critical point (BCP)” between the interacting nuclei (as shown in Figure 4), a critical point that has one positive and two negative curvatures of the electron density (a saddle point). It has been shown that the electron density at such a hydrogen BCP has a value within the range of 0.002 to 0.04 au,³⁹ its second derivative, the Laplacian ($\nabla^2\rho$) is in the range of 0.015 to 0.15 au³⁹ and there is a mutual penetration of the hydrogen and the acceptor atom. Besides these topological properties, integrated properties of the electron density are also affected upon hydrogen bonding, namely there is an increase in the net positive atomic charge (loss of charge) on H, an energetic destabilisation of the hydrogen atom, a decrease in its dipolar polarisation and a decrease

in its atomic volume.³⁰ Integration is performed over the volume bordered by interatomic surfaces (shown in green in Figure 4).

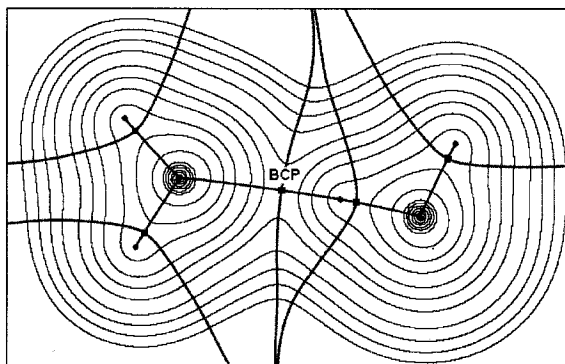


Figure 4. Contour plot of the electron density for two hydrogen-bonded water molecules. The hydrogen bond critical point is labelled. Interatomic surfaces are shown as green lines.

1.4. Objectives

The purpose of this project is to probe the lateral H-bonding between DPGG headgroups and its effect on monolayer behavior. To do this, we compare the monolayer behavior of DPGG (1) with its analogs with different placement and number of hydroxyl groups on the headgroup (Figure 5), namely dipalmitoyl-3,5-dihydroxybenzoylglycerol (DP-3,5-HBG) (2), dipalmitoyl-3,4-dihydroxylbenzoylglycerol (DP-3,4-HBG) (3), dipalmitoyl-4-hydroxylbenzoylglycerol (DP-4-HBG) (4), dipalmitoyl-3-hydroxybenzoylglycerol (DP-3-HBG) (5). In the extreme case of dipalmitoyl-3,4,5-methoxybenzoylglycerol (DP-3,4,5-MBG) (6), all three hydrogen atoms in the hydroxyl groups of DPGG are replaced with methyl groups in order to completely disrupt the hydrogen bonding network if it does exist.

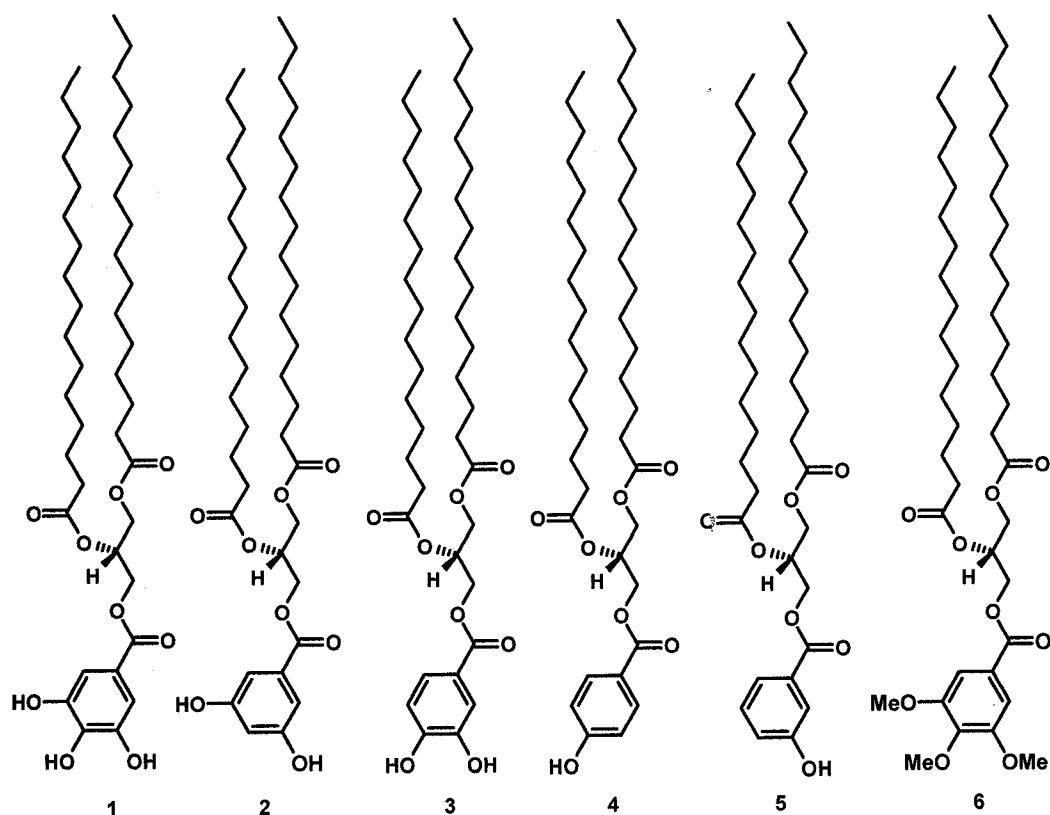


Figure 5. Chemical structures of phenolic lipids (n-hydroxybenzoic acids) (**1-5**) and the methoxy substituted analog (**6**).

The isotherms and morphology of racemic phenolic lipid monolayers at the air/water interface, through Langmuir film balance and Brewster angle microscopy (BAM), are compared to understand the headgroup structure on the monolayer behavior of the racemic phenolic lipids. Changes in temperature and period of time allowed for monolayer equilibration at the air/water interface are performed to better understand the interactions between the lipid molecules. Moreover, in order to determine if the lipids are hydrogen bonded with each other in the spreading solution, FT-IR (Fourier transform infrared) and ^1H NMR (proton nuclear magnetic resonance) spectroscopic studies are

performed. The influence of chirality on the DPGG monolayer is also included in this study.

A computational study is done on the gas phase interactions of phenolic lipid headgroups and their small assemblies (dimers and trimers) to understand their possible configurations to form hydrogen bonds in the gas phase. Hydrogen bonds between phenolic lipid headgroups are located through the electron density and verified by evaluating atomic properties of H and O atoms according to established theory. The full DPGG molecule is simulated and the potential energy curves are generated to find the most stable configuration.

Chapter 2. Methods

2.1. Instruments

2.1.1. Langmuir Film Balance

A schematic diagram of a Langmuir film balance is shown in Figure 6. The Langmuir film balance consists of a fabricated teflon trough, one (for the asymmetric compression mode) or two (for the symmetric compression mode) moveable barrier(s), and a Wilhelmy plate. The teflon trough is filled with the aqueous subphase. Spreading of amphiphilic materials at the air/water surface will create a monolayer (if space allows) with known area and number of molecules. This is usually achieved by pre-dissolving the amphiphiles in a solvent, ejecting small amounts from a micrometer syringe at various points on the liquid surface, and allowing evaporation of the solvent. The surface area of the monolayer can be changed by the movable barrier(s). The surface tension of the subphase with or without a monolayer can be measured by the Wilhelmy plate.

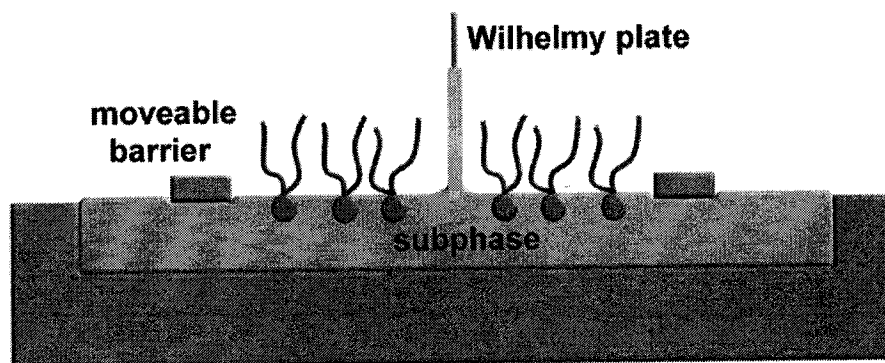


Figure 6. Schematic diagram of a Langmuir film balance.

2.1.2. Brewster Angle Microscopy (BAM)

BAM is an optical technique that can be used to visualise the surface morphology of monolayers. The biggest advantage of optical techniques in surface study is that they do not require direct contact with the samples so that they can provide “real time” images, which reflect the morphology of the films.

David Brewster, a Scottish Physicist of the early 19th century, discovered that when light moves between two media with different refractive indices, *p*-polarised light (with respect to the interface) was not reflected at a specific incident angle.⁴⁰ This angle is known now as the Brewster angle, which can be calculated as follows:

$$n = \frac{\sin \alpha}{\sin \beta} = \frac{\sin \alpha}{\sin(90 - \alpha)} = \tan \alpha$$

where *n* is the refractive index of the medium, α is the angle of incidence and β is the angle of refraction.

BAM was developed in 1991 by H  non and Meunier (French) and H  nig and M  bius (German). This technique makes good use of the zero reflectance at the Brewster angle of an air/water interface or dielectric substrate for polarised light.⁴¹

As shown in Figure 7, laser light (wavelength = 532 nm) is polarised by a filter to produce *p*-polarised light. By introducing the *p*-polarised light at the Brewster angle (as shown by the above equation, the Brewster angle for air/water is 53.15  ) before spreading the monolayer at the air/water interface, there is no reflection from the water surface, and the background of the BAM image is then completely dark. After spreading of a monolayer, 53.15   is no longer the Brewster angle for this interface. Therefore, light is

reflected (see Figure 8). A condensed phase of the monolayer will result in high contrast images of the film because it has the largest difference in refractive index from that of water (as compared to liquid and gaseous phases). In the case that the amphiphilic molecules have the side chains tilted in different directions or arranged in non-hexagonal arrangements, anisotropic domains will form, resulting in BAM images with different darkness levels within the same domain.

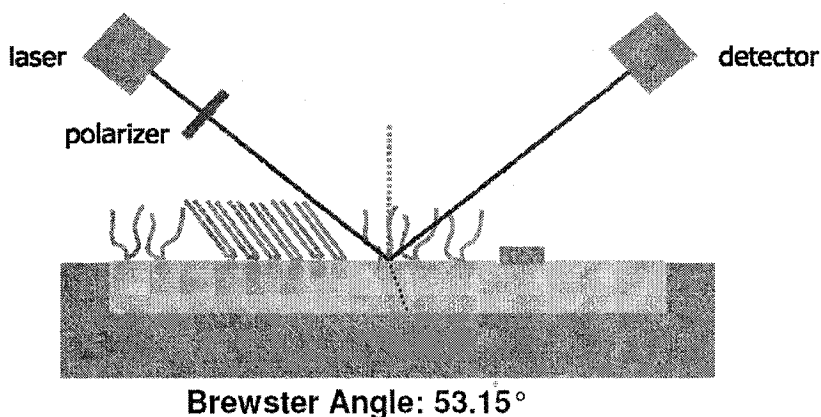


Figure 7. Schematic diagram of Brewster angle microscopy.

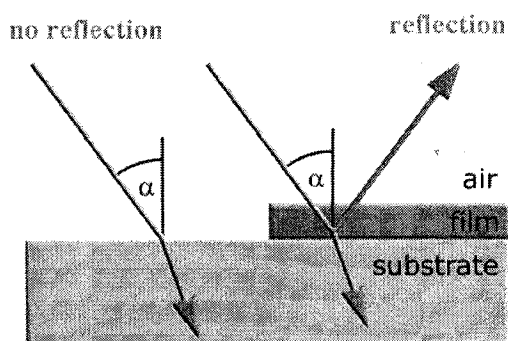


Figure 8. Schematic illustration of the reflection change before and after spreading of a monolayer.

2.2. Method and Materials for the Monolayer Study

Enantiomerically pure (R-configured) DPGG was purchased from Avanti Polar Lipids Inc. (Alabaster, AL), and was used without further purification (for the structure refer to (1) of Figure 5). Racemic phenolic lipids were prepared by Schmidt et al. according to their published method.⁴² Ultrapure water with a resistivity of $18.2 \text{ m}\Omega \text{ cm}^{-1}$ was obtained from an EasyPure II LF system (Barnstead, Dubuque, IA). Except where mentioned otherwise, all the experiments were performed with the racemic compounds.

Monolayers of phenolic lipids were spread using a Hamilton 50 μL syringe from chloroform solutions with a concentration of 0.8 mM and using a volume of 30 μL on a subphase of ultra-pure water ($\text{pH} = 5.3\text{-}6.3$ at 25°C). Surface pressure-area isotherms were obtained with a compression speed of $5 \text{ cm}^2 \text{ min}^{-1}$ (which corresponds to $0.058 \text{ \AA}^2 \text{ molecule}^{-1} \text{ s}^{-1}$ for a spreading volume of 30 μL of a 0.8 mM phenol lipid solution) using a Langmuir film balance (Nima Technology Ltd., Coventry, U.K.) equipped with a filter paper Wilhelmy plate. All isotherms were obtained with symmetric compression immediately after spreading.

BAM images were obtained using an I-Elli2000 ellipsometer (Nanofilm Technology GmbH, Göttingen, Germany) with a green laser ($\lambda = 532 \text{ nm}$) of 50 mW intensity. A $20\times$ magnification was used with a $1\mu\text{m}$ lateral resolution for all images. BAM images were obtained using a laser output of 50% at the Brewster angle for water.

2.3. Spectroscopy

IR studies were done using a Nicolet Magna-IR550 spectrometer (Thermo Electron Corporation, USA) equipped with Whatman FT-IR purge gas generator. Deuterated

triglycine sulfate (DTGS) KBr typed detector was used, which provides a spectral window of 6000 to 350 cm^{-1} . The beamsplitter and plates of the cells were made of KBr. CHCl_3 was used as the solvent.

The ^1H NMR study was done using an Oxford NMR300 (Varian Corporation, USA) with a radio frequency of 300 MHz at room temperature. The solvent used was CDCl_3 . Spectra were referenced to the CHCl_3 signal at 7.26 ppm. Signals are labelled with b (broad), vb (very broad) and o (hidden/overlap).

2.4. Calculations

All electronic structure calculations were carried out using GAUSSIAN 98⁴³ or GAUSSIAN 03.⁴⁴ Calculations employed the semiempirical PM3,⁴⁵ ab initio Hartree-Fock (HF)⁴⁶ and Møller-Plesset perturbation theory of second order (MP2),⁴⁶ and the density-functional theory functionals Becke's three parameter hybrid exchange/Lee-Yang-Parr correlation functional (B3LYP)^{47, 48} and the 1996 "parameter-free" density-functional of Perdew-Burke-Ernzerhof (PBE0).^{49, 50} All geometries were fully optimised, except where stated otherwise. Frequency calculations were performed within the rigid rotor/harmonic oscillator approximation, to determine the nature of the stationary points and to obtain free energies. Atomic properties of H atoms, including the atomic energy, population, dipole moment and atomic volume, are calculated with the program PROAIMV of the AIMPAC series of programs.⁵¹ Radii of H and O atoms are calculated using the program PROFIL, also of AIMPAC. Molecular graphs are plotted, and electron densities and Laplacian values are determined, from AIM2000.^{52, 53} Molecules are plotted with Molekel.⁵⁴

Chapter 3. Monolayer Behavior of Phenolic Lipids:

Experimental Study

3.1. Introduction

Amphiphiles can form monolayers at the air/water interface because of their surface activity due to their molecular hydrophilic-hydrophobic balance; too great a weight on either part makes a monolayer unstable.⁵⁵ Small changes in the ratio between the hydrophilic part and the hydrophobic part of the amphiphiles bring about significant changes in the surface morphology and the phase behavior of monolayers.⁵⁶ Systematic changes in the intermolecular interactions can be achieved by introducing side chains with different length in different positions or by changing the polar groups on the headgroups.

Many studies have examined the influence of changing both the hydrophobic part and the hydrophilic parts of molecules on monolayer properties. For example, lengthening of the alkyl chain for either phospholipids or polymers increases the van der Waals interactions between side chains, resulting in a shift of the phase transitions of isotherms to lower pressures,^{14, 55, 57-61} an increase in ordering in two dimensions,^{14, 55, 57-61} as well as significant morphological changes.^{14, 60, 61} Changing the size or functional groups on the headgroups can also have dramatic influence on the monolayer behavior of amphiphiles. Numerous studies have confirmed the influence of headgroup structure of amphiphilic molecules on their monolayer properties.^{14, 15, 62, 63} Weidemann. et al.⁶³ compared the surface behavior of DPP(Me)E, DPP(Me₂)E and DPPC (DPP(Me)₃E) with

those of DPPE (DPPH₃E) to understand the influence of headgroup size on phospholipid monolayers. They found that changing the size of the headgroup changed the shape of the condensed phase domains as larger headgroups hinder the chains from erection. As a result, they found dendritic domains for DPP(Me)E and DPPE, but not for DPP(Me)₂E and DPPC. Since dendritic growth results from anisotropic line tension, loss of dendritic structure in the larger headgroup systems means the side chains are more disordered. The order of collapse pressures for the four lipids they studied was DPPC > DPP(Me)₂E > DPP(Me)E > DPPE, which was also due to the size change of the headgroup. For molecules with large headgroups, as DPPC and DPP(Me)₂E, no complete erection of the side chains could be achieved.

The monolayer behavior of DPGG is thought to be governed by a lateral hydrogen bonding network.³ In this study, we compare the monolayer behavior of DPGG with that of phenolic lipids with different placement and number of hydroxyl groups on the headgroup (Figure 5). The isotherms and morphology of phenolic lipid monolayers at the air/water interface at different temperatures are compared to understand the influence of headgroup structure on the monolayer behavior of phenolic lipids.

3.2. Influence of Headgroup Structure on the Monolayer Behavior of phenolic Lipids

3.2.1. Monolayer Behavior of phenolic Lipids at 25 °C

3.2.1.1. Isotherms

Isotherms of the phenolic lipids at 25°C are shown in Figure 9. It shows that headgroup alterations do have an influence on the isotherms of phenolic lipid monolayers. Except for DP-3,4,5-MBG, the only compound without any OH group on the aromatic ring, all the phenolic lipid monolayers appear to show isotherms with a direct transition from gaseous phase to condensed phase at 25°C while DP-3,4,5-MBG films show a LE phase at large molecular areas and low pressures. Whether or not a monolayer shows direct transition from gaseous phase to condensed phase depends on factors including temperature, size of the headgroup, interactions between the headgroup and van der Waals interactions between the side chains.^{14, 16, 62, 64} Generally, lower temperature, smaller headgroup, stronger attractive interactions between headgroups, longer (or more) saturated side chain(s) favor the direct transition for a monolayer from gaseous phase to condensed phase. Many other lipids also showed the G-C direct transition at room temperature, for example 1,2-dilignoceroyl-glycerol-3-phosphacholine (DLPC; C24)⁵⁸ due to the long side chains, and diacylphosphatidylethanolamine^{62, 65} due to hydrogen bonding between the headgroups.

Because the DP-3,4,5-MBG molecule has the same side chains as the other phenolic lipids and all the isotherms were collected at the same temperature, the LE-LC plateau on the isotherm of the DP-3,4,5-MBG monolayer can be explained by the

following possible reasons. First the interaction between the headgroup of the methoxyl compound is not as strong as those of the lipids with OH groups. OH groups can form $O\cdots H-O$ hydrogen bonds with each other, which is a fairly strong interaction, while OCH_3 groups cannot form the same kind of hydrogen bonds. The disruption of the lateral $O\cdots H-O$ hydrogen bonds between the headgroups replaces the stronger hydrogen bonding with much weaker interactions. As a result, the DP-3,4,5-MBG molecules are less constrained by the neighboring molecules and they have more flexibility at the surface. In addition the methyl groups are bulkier than H atoms. Consequently, the methyl groups prevent the constituent molecules of DP-3,4,5-MBG monolayer to closely pack at low pressures. The monolayer behavior of DP-3,4,5-MBG may be the result of the combination of both of these factors. Therefore, side chains of DP-3,4,5-MBG molecules do not interact with each other effectively, hence its isotherm shows a liquid expanded phase at low surface pressures.

The isotherm of DP-3,5-HBG is shifted to much larger molecular areas ($60 \text{ \AA}^2 \text{ molecule}^{-1}$ compared to $50 \text{ \AA}^2 \text{ molecule}^{-1}$ for DPGG isotherm) which may be caused by the different patterning of lateral hydrogen bonds between the phenolic lipid headgroups. Except for DP-3,5-HBG, all the other phenolic lipids show similar condensed phase molecular areas despite a large variation in headgroup size. The isotherm of DP-3-HBG has a slightly larger critical area than that of DP-4-HBG, which again suggests that due to the different position of the OH group on the headgroup, the orientation of the lipid molecules is different at the air/water interface. The larger critical area of the DP-3-HBG isotherm suggests that a DP-3-HBG molecule occupies a larger space at the air/water

interface than a DP-4-HBG molecule, which maybe caused by DP-3-HBG molecules tilting more than the DP-4-HBG molecules.

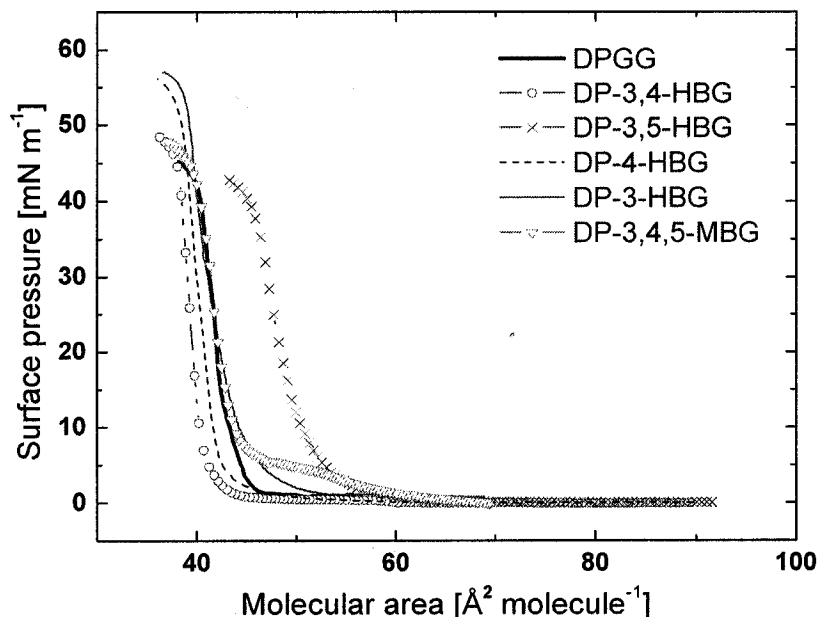


Figure 9. π -A Isotherms of phenolic lipids on water at 25°C.

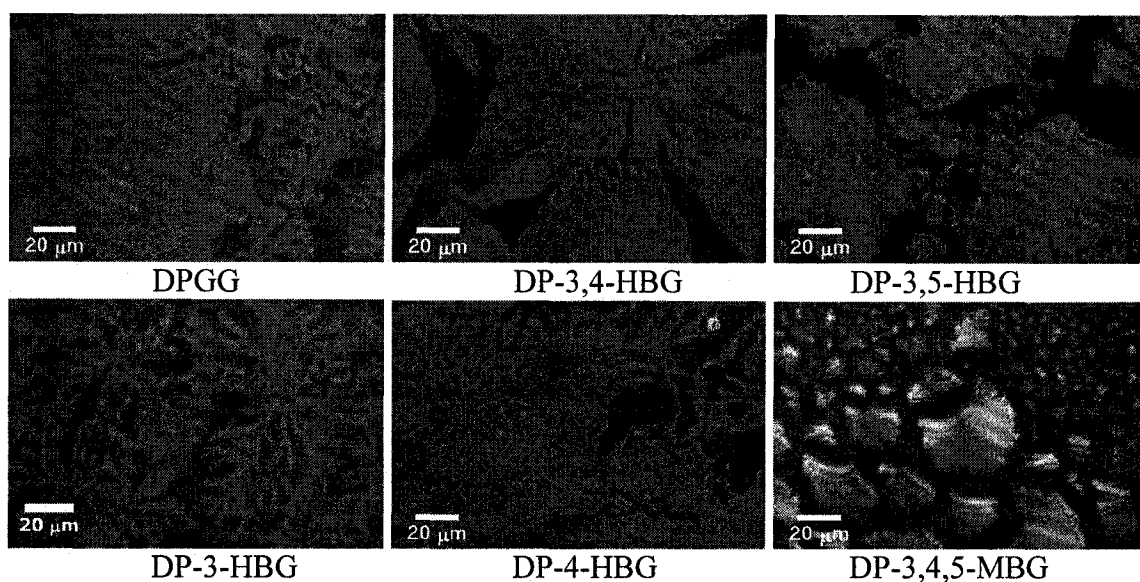
The larger collapse pressures of DP-4-HBG and DP-3-HBG compared to those of the other phenolic lipids indicate that the DP-4-HBG and DP-3-HBG monolayers are more stable than those of the other phenolic lipids. The collapse pressure of all the lipids studied is DP-4-HBG and DP-3-HBG (55 mN m^{-1}) > DPGG; DP-3,4-HBG; DP-3,4,5-MBG (50 mN m^{-1}) > DP-3,5-HBG (45 mN m^{-1}). This is contradictory to that was observed by Weidemann et al.⁶³ where larger headgroups had higher collapsing surface pressures. This indicates that headgroup size is not the only factor that influences the collapse pressure of phenolic lipids. Interactions between the headgroups also play an

important role on the collapse pressure for molecules that interact strongly with neighboring molecules.

3.2.1.2. BAM images

BAM images of the phenolic lipid monolayers are shown in Figure 10. It shows that in all cases, a condensed phase has already formed at zero surface pressure and very large surface areas (130 cm^2 , average area for each molecule at the surface is about 90 \AA^2). DP-3,4,5-MBG monolayer also forms islands of condensed phases although its isotherm shows a LE-C plateau. The presence of the plateau despite the existence of aggregation cannot easily be explained and warrants further investigation. The aggregation is probably caused by the van der Waals interactions between the side chains plus weak interactions between the headgroups, including weak hydrogen bonding, van der Waals interactions and possible π -stacking. Moreover, the size of condensed phase domains formed at the air/water interface for all the phenolic lipids is quite different from each other. It is unusual to see, for DPGG, DP-3,4-HBG, DP-4-HBG and DP-3,5-HBG, such large extensive aggregation yielding entire regions of condensed phase rather than just small domains, especially at such high molecular areas. Domain sizes for DP-3,4,5-MBG are much smaller than for the other phenolic lipids with -OH groups on the aromatic ring. The shape of the condensed phase domains for DP-3,4,5-MBG are also significantly different from those for the other phenolic lipids. Since all the compounds have already formed aggregates immediately after being spread, compression results only in the movement and interaction of the aggregates.

(a) Surface pressure $\pi = 0 \text{ mN m}^{-1}$ (after spreading without any compression, surface area is 130 cm^2 , $90 \text{ \AA}^2 \text{ molecule}^{-1}$)



(b) Surface pressure $\pi = 5 \text{ mN m}^{-1}$

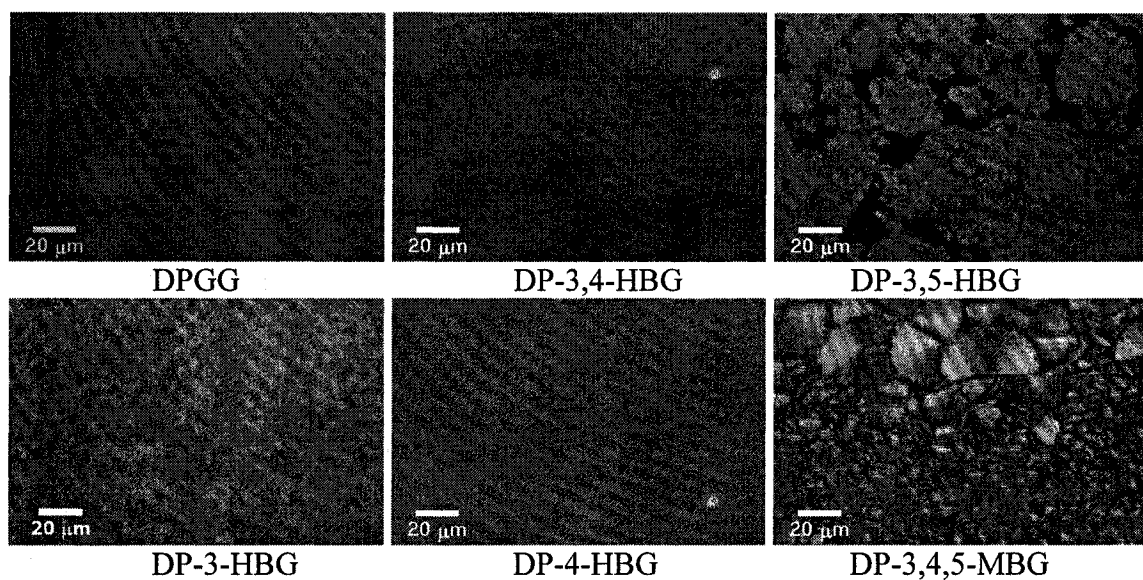


Figure 10. BAM images of phenolic lipids (as indicated) at different surface pressures.

The BAM images for DPGG, DP-3,4-HBG, and DP-4-HBG are very similar with each other for all surface pressures. Dark spots shown in DPGG, DP-3,4-HBG and DP-4-

HBG BAM images at 5 mN m^{-1} (Figure 10) are holes not completely disappeared yet due to the monolayer not being very compact. At higher surface pressures, DPGG, DP-3,4-HG and DP-4-HBG all exhibit smooth isotropic phases as shown in Appendix A. According to Kato et al.,⁶⁶ the shape and texture of the domain is determined by quite a few factors, including line tension between the phases, subphase temperature, compression speed, orientation of the molecules, interactions between the alkyl chains (mainly the van der Waals interaction), and interactions between the headgroups. The similarity in the BAM images for the three phenolic lipids with *p*-hydroxyl groups suggests the similar orientation of their molecules and interaction between the side chains and headgroups. Lack of anisotropy suggests the low tilt angle of phenolic lipid molecules with *p*-hydroxyl groups. DP-3-HBG clearly exhibited dendritic structures at 0 mN m^{-1} (Figure 10). According to Weidemann et al., dendritic structures are caused by an anisotropic line tension, which indicates a crystalline state of the monolayer.⁶³ However, the crystalline state of the DP-3-HBG monolayer quickly changes into the anisotropic domains as shown in Figure 10 (b) when the surface pressure is 5 mN m^{-1} . Actually, this fast change of domain morphology occurs even before compression when the surface pressure is 0 mN m^{-1} , and it starts with the disappearing of the dendritic arms and appearing of bright spots. Monolayers of DP-3,5-HBG and DP-3,4,5-MBG monolayers also exhibit anisotropic phases, which indicate that the side chains tilt to different directions within a domain. The anisotropic phases for DP-3,5-HBG are not easy to see at low temperatures but become more evident at higher temperature as will be discussed later. The domain shape of DP-3,4,5-MBG is very similar to that of L-DPP(Me₂)E observed by Weidemann et al.⁶³ except that DP-3,4,5-MBG does not have any continuous

changes of orientation within a domain. Domains for L-DPP(Me₂)E have lines to separate dark and bright boundaries whereas the lines continuously shifted with the rotation of the analyzer. This phenomenon was not observed for DP-3,4,5-MBG. The anisotropy is associated with tilted domains, which corresponds nicely with the isotherm shifts for DP-3-HBG, DP-3,5-HBG and DP-3,4,5-MBG since more highly tilted molecules occupy a greater area at the interface.

3.2.2. Monolayer Behavior of Phenolic Lipids at 38 °C

Temperature plays an important role on the nature of monolayers. By increasing the temperature of the monolayer systems, more kinetic energy is provided. Hence the mobility of the molecules is increased, molecules interact with each other less effectively and a LE phase may appear or shift to higher pressures compared to at room temperature.

3.2.2.1. Isotherms

A comparison of the isotherms obtained at 25°C and 38°C for each of the compounds is given in Figure 11. This figure shows that DPGG, DP-3,4-HBG and DP-4-HBG have very similar isotherms at both 25°C and 38°C although there are differences in the surface pressure for the loss of the LG phase at 38°C, which has the following order: DP-4-HBG > DP-3,4-HBG > DPGG. This ordering indicates the interactions between DPGG headgroups are strongest and those between DP-4-HBG headgroups are weakest, which makes sense because there are three hydroxyl groups on DPGG compared to the one hydroxyl group on DP-4-HBG. The similarity in isotherms of DPGG, DP-3,4-HBG and DP-4-HBG at both 25°C and 38°C indicates that the *para*-hydroxyl group is very important to the monolayer behavior of the phenolic lipids.

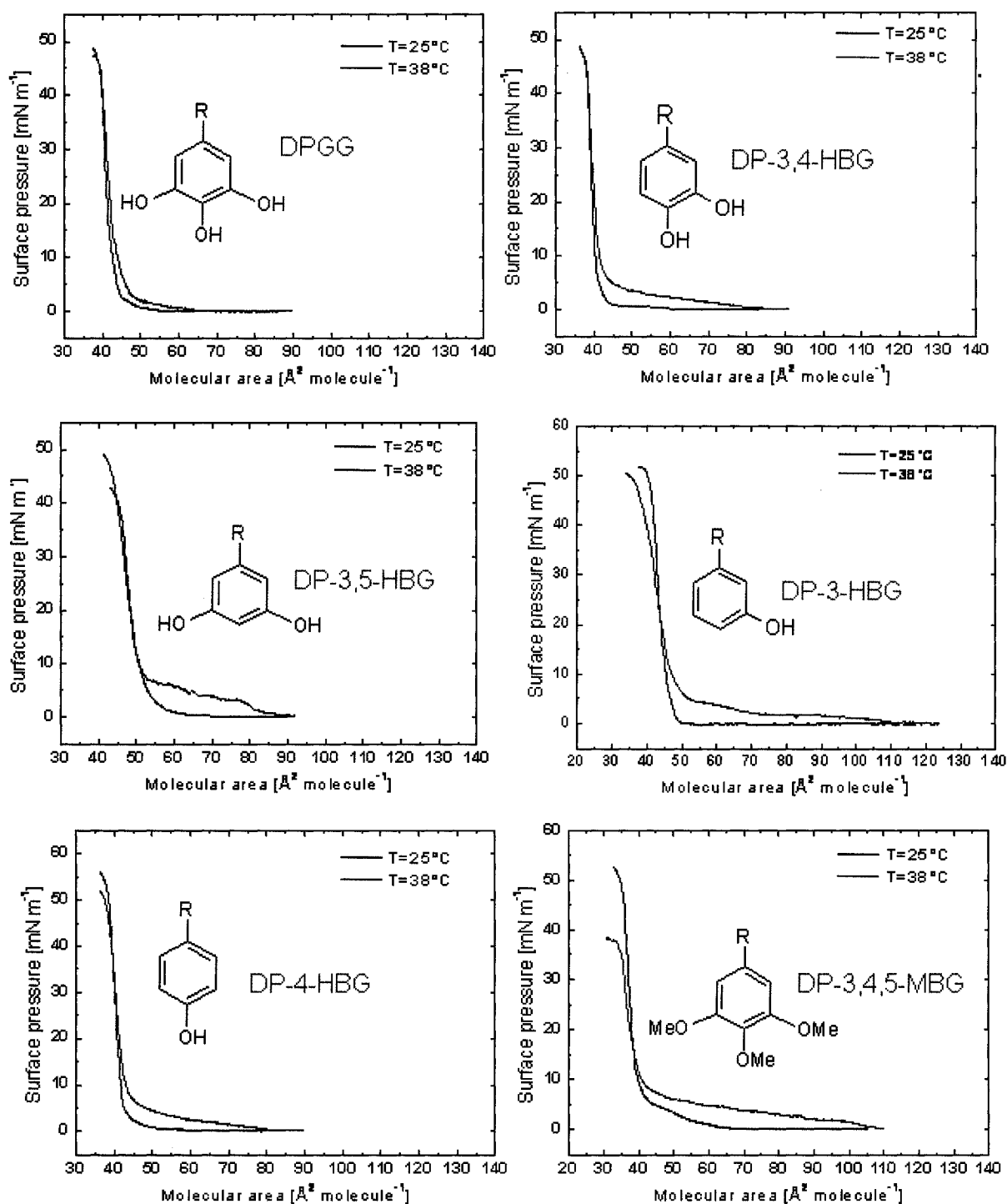


Figure 11. Temperature effect on phenolic lipid monolayers.

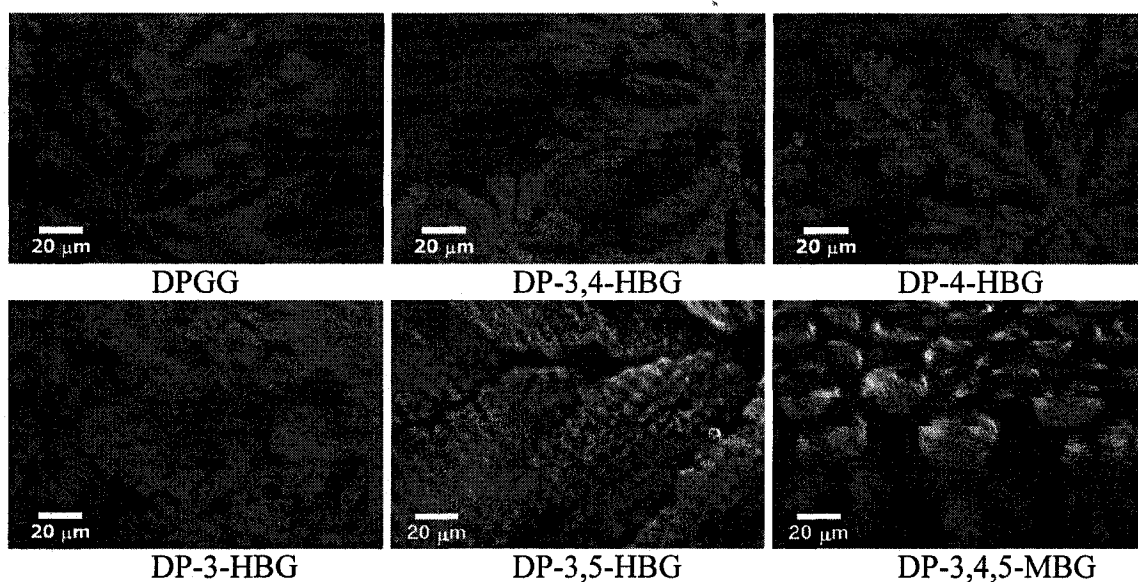
The isotherm of DP-3-HBG at 38°C differs from those of DPGG, DP-3,4-HBG and DP-4-HBG in a longer LE phase and an increased compressibility of the monolayer. The

isotherm of DP-3,5-HBG at 38°C still has a larger critical area than all the other phenolic lipids with more distinct plateau region. The isotherm of DP-3,4,5-MBG at 38°C has the collapse pressure occurring at much lower value (39 mN m^{-1}) compared to at 25°C (53 mN m^{-1}). This large change in collapse pressure also indicates that DP-3,4,5-MBG is affected most by a temperature increase, these suggest the DP-3,4,5-MBG molecules are less constrained by the neighboring molecules and interactions between its headgroups are weak. DP-3,5-HBG, DP-3-HBG and DP-4-HBG also show some decrease in collapse pressure whereas those of DPGG and DP-3,4-HBG do not, suggesting that the DPGG and DP-3,4-HBG have stronger interactions between their headgroups.

3.2.2.2. BAM Images

As mentioned above, increasing temperature can increase the mobility of molecules, therefore, molecules interact less efficiently with each other and a LE phase will appear. This is reflected in BAM images, where smaller and more fluid-like domains are expected than at lower temperatures. BAM images for all the phenolic lipids at 38°C with a surface pressure of 2 mN m^{-1} are summarised in Figure 12. For a surface pressure of 0 mN m^{-1} , DP-3,4,5-MBG did not show any aggregates, in contrast to the other lipids, which suggests the weak interaction between the constituent molecules.

(a) Surface pressure is 2 mN m^{-1}



(b) Surface pressure is 5 mN m^{-1}

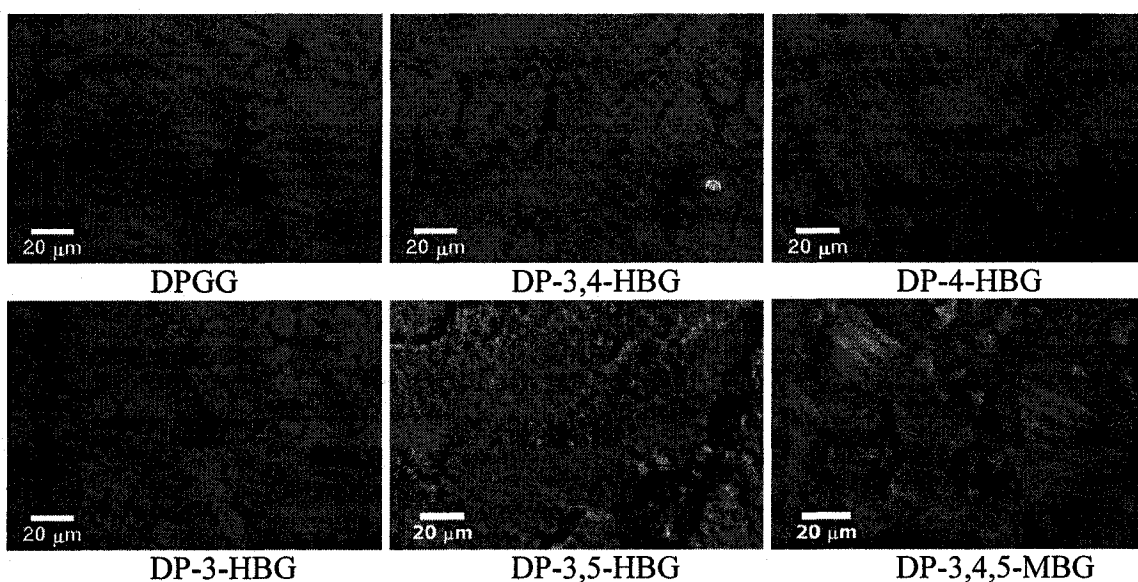


Figure 12. BAM images of phenolic lipids at 38°C .

Figure 12 shows that at 38°C , DPPG, DP-3,4-HBG and DP-4-HBG, phenolic lipids with similar isotherms (Figure 9) and BAM images (Figure 10) at 25°C , still have very

similar BAM images at 38°C, although the aggregates look more fluid and show branched domains. DP-3-HBG shows domains with similar shape to those of DPGG, DP-3,4-HBG and DP-4-HBG, but the domain sizes are smaller. The branched domains for DPGG, DP-3,4-HBG, DP-3-HBG and DP-4-HBG may originate from intermolecular interactions that are highly directional.¹⁴ According to Wang et al.,¹⁴ rigid and large aggregates are formed with a domination of van der Waals interactions between the side chains over hydrogen bonding between the headgroups. Increasing temperature breaks van der Waals interactions more readily than hydrogen bonds, therefore, at higher temperatures, hydrogen bonds, which are more directional, dominate and elongated structures form. The domain shape of DPGG, DP-3,4-HBG, DP-3-HBG and DP-4-HBG at 38°C is very similar to that of N-(β-hydroxyethyl)tridecanoic acid amide (HETA) (structure of HETA is shown in Figure 13) obtained by Vollhardt et al.,⁶⁷ which also has the ability to form H-bonds. Another similarity between BAM images of the four phenolic lipids and those of HETA is the coexistence of the branched domains with smaller, nearly round, domains (not shown in Figure 12; see Appendix A (10)). As Vollhardt mentioned,⁶⁷ the branched domains with thick arms (usually six) connected to a compact center indicate fluidity of the monolayers. Moreover, reflections of all the domains of the four phenolic lipids and HETA are homogeneous, indicating the alkyl chains are normal to the subphase or at least with a low tilt angle.

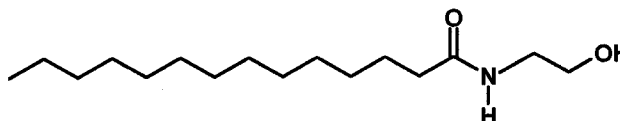


Figure 13. Molecular structure of HETA.

As at 25°C, BAM images of DP-3,5-HBG and DP-3,4,5-MBG still differ from those of the three pyhenolic lipids with *para*-OH groups. DP-3,5-HBG forms large anisotropic blocks, suggesting that side chains of DP-3,5-HBG tilt to different directions with space in between the domains. DP-3,4,5-MBG monolayer begins to show some dendritic structures when the temperature is increased to 38°C, which disappear when the surface pressure is increased to 5 mN m⁻¹. For this molecule, when the surface pressure is 0 mN m⁻¹, there are not any visible aggregates formed, which confirms the weaker interaction between its headgroups. The other lipids all showed aggregates immediately after spreading; for DPGG, DP-3,4-HBG, DP-3-HBG and DP-4-HBG, their aggregates exhibit thinner branches at 0 mN m⁻¹ than at 2 mN m⁻¹. Again this low aggregation despite plateau in isotherm needs further investigation. DP-3,5-HBG exhibits similar sized domains at both surface pressures. Images for all the molecules studied are shown in Appendix A.

3.3. Comparison of the Monolayer Behavior of the Enantiomerically Pure DPGG with Racemic DPGG

It has been observed that amphiphiles with headgroups including amino acids, amides, phosphates and glycerol derivatives showed different extents of chiral effects onto their monolayer behaviors.⁶⁸ These were illustrated by the different isotherms and film morphologies of the two enantiomers for some species, including for example N-stearoylserine methyl ester, N- α -palmitoylthreonine, 1-stearylamine glycerol and DPPC.⁶⁸ Differences in the isotherms and film morphologies between the two enantiomers also led to differences in the isotherms and film morphologies of the enantiomerically pure compounds compared to their racemic mixtures.

In this section, the monolayer behavior of enantiomerically pure DPGG will be compared with that of racemic DPGG to verify if there are any chiral effects for this newly synthesized phenolic lipid.

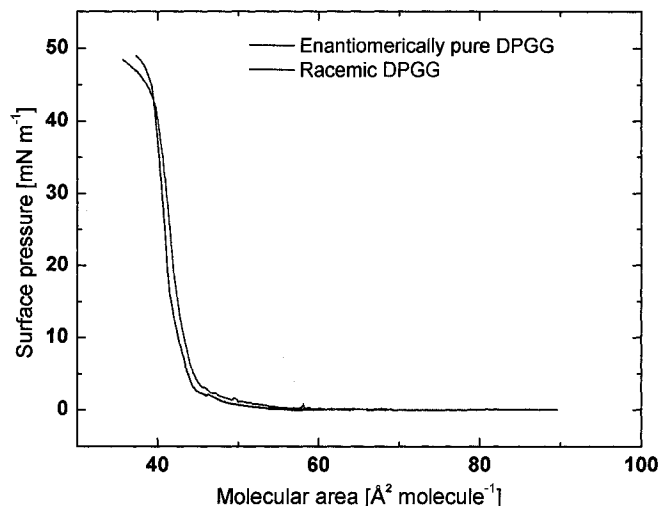
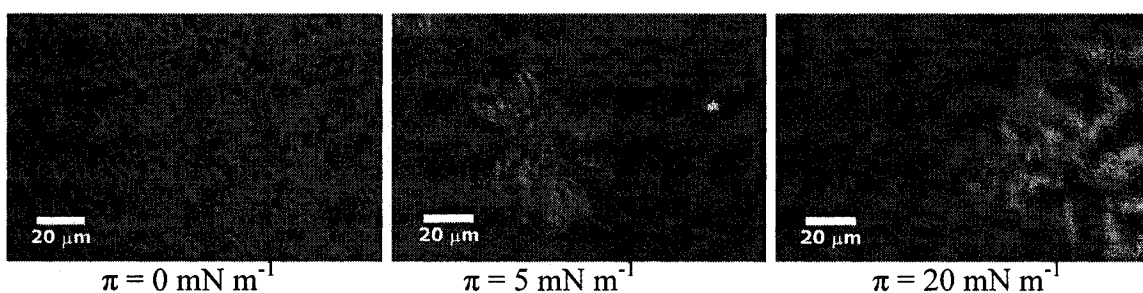


Figure 14. Isotherms of enantiomerically pure and racemic DPGG at 25°C.

The isotherms of enantiomerically pure DPGG and racemic DPGG at 25°C are shown in Figure 14. It shows both exhibit the same isotherm within experimental error. This result is contradictory to that obtained by James Fairbairn.⁶⁹ He observed that the isotherm for racemic DPGG shifted to a larger molecular area by 15 Å²·molecule⁻¹, and it was explained by a heterochiral preference causing more efficient packing. The contradiction between these results can be explained by different experimental conditions. For the results in this thesis, the isotherms were obtained by compressing the monolayer immediately after the spreading, while earlier the monolayer was permitted to sit uncompressed for 5 minutes. Due to an equilibration effect for the enantiomerically pure DPGG, the isotherm shifts to larger molecular area as will be described later.

1) Enantiomerically pure DPGG



2) Racemic DPGG

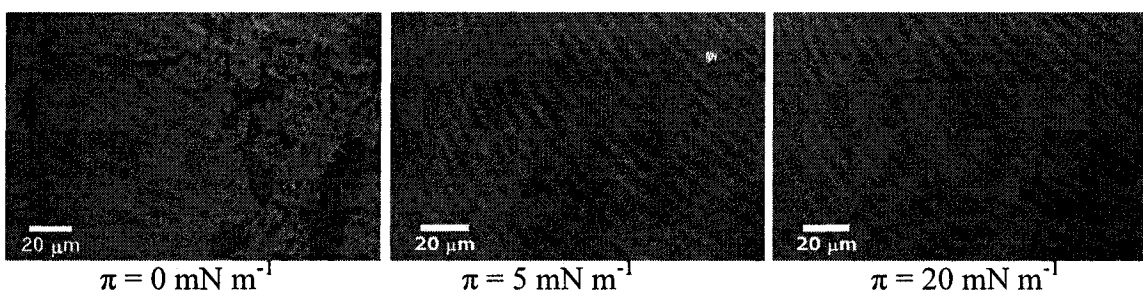


Figure 15. BAM images of enantiomerically pure DPGG and racemic DPGG at 25°C; monolayers were compressed right after spreading.

BAM images for both enantiomerically pure and racemic DPGG are shown in Figure 15. It shows that the enantiomerically pure DPGG monolayer exhibits dendritic structures after spreading of the solution at the air/water interface (the image was taken immediately after spreading), while racemic DPGG shows compact structures at a surface pressure of 0 mN m⁻¹. With compression, enantiomerically pure DPGG starts to show coexistence of some unusual anisotropic domains with smooth structures surrounding them (as shown in the images for surface pressures of 5 mN m⁻¹ and 20 mN m⁻¹), while the racemic DPGG monolayer only exhibits smooth, isotropic structures.

An interesting phenomenon about the anisotropic aggregates for enantiomerically pure DPGG is that their size and number increases with an increase in equilibration time (the period of time the monolayer is allowed to sit at the air/water surface after spreading prior to compression). Figure 16 shows the effect of equilibration on the monolayer behavior of enantiomerically pure DPGG.

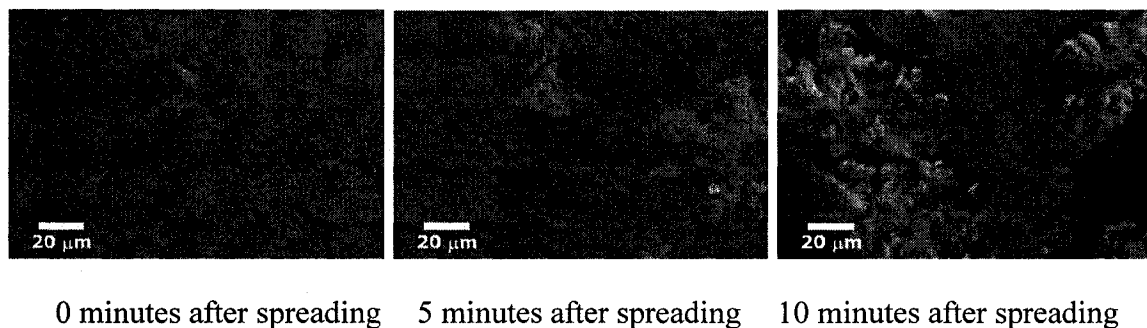


Figure 16. Morphology changes in the monolayer of enantiomerically pure DPGG with increasing equilibration time (without compression).

The anisotropic aggregates shift the isotherm of enantiomerically pure DPGG to larger molecular areas as shown in Figure 17. This indicates that the anisotropic domains occupy larger areas than the smooth structures. This may be explained by an increased tilting of the side chains to different directions. The same period of equilibration was allowed for the racemic DPGG monolayers, but no anisotropic aggregates were observed, and the isotherm did not change.

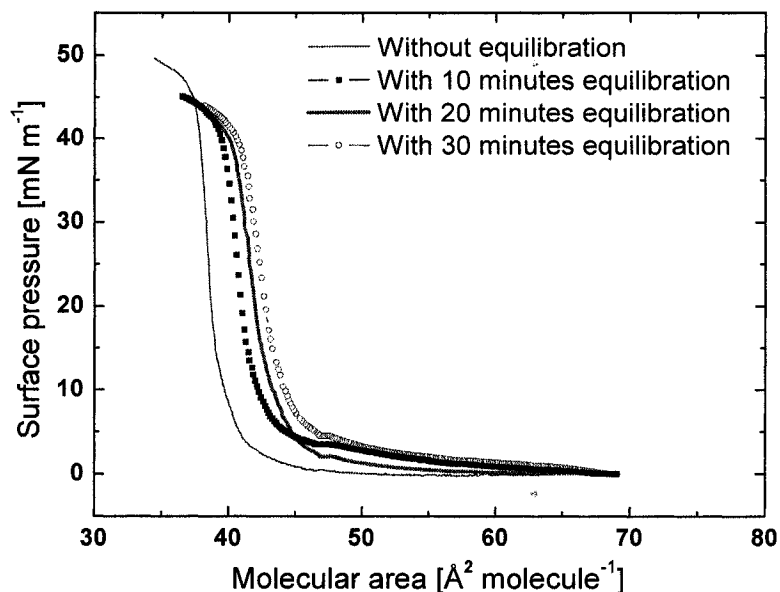


Figure 17. Effect of equilibration on monolayer behavior of enantiomerically pure DPGG.

BAM images at different surface pressures are shown in Figure 18 for the enantiomerically pure DPGG monolayers equilibrated for 10 minutes. A comparison between Figure 15 (a) and Figure 18 shows that equilibration favors the formation of the anisotropic domains, which indicates that the rearrangement of the enantiomerically pure DPGG molecules at the air/water interface is slow, possibly due to strong H-bonding hindering rearrangement. The reason and mechanism for the formation of the anisotropic aggregates in the monolayer of enantiomerically pure DPGG is still not clear. One possible reason is that enantiomerically pure DPGG packs differently at the air/water interface compared to the racemic mixture.⁶⁸

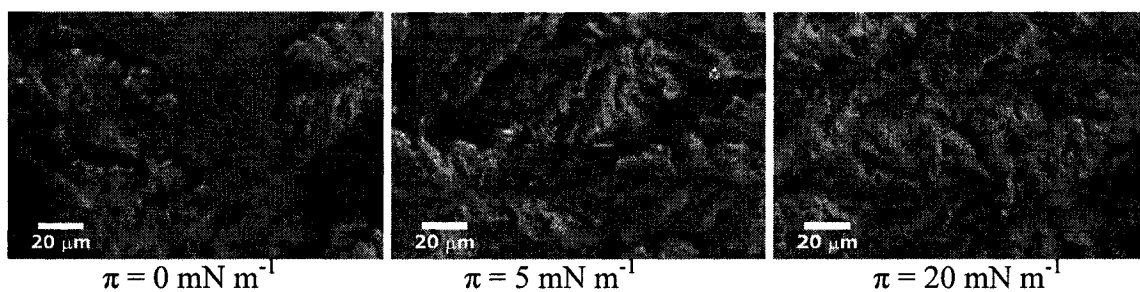


Figure 18. BAM images of enantiomerically pure DPGG with 10 minutes of equilibration at different surface pressures.

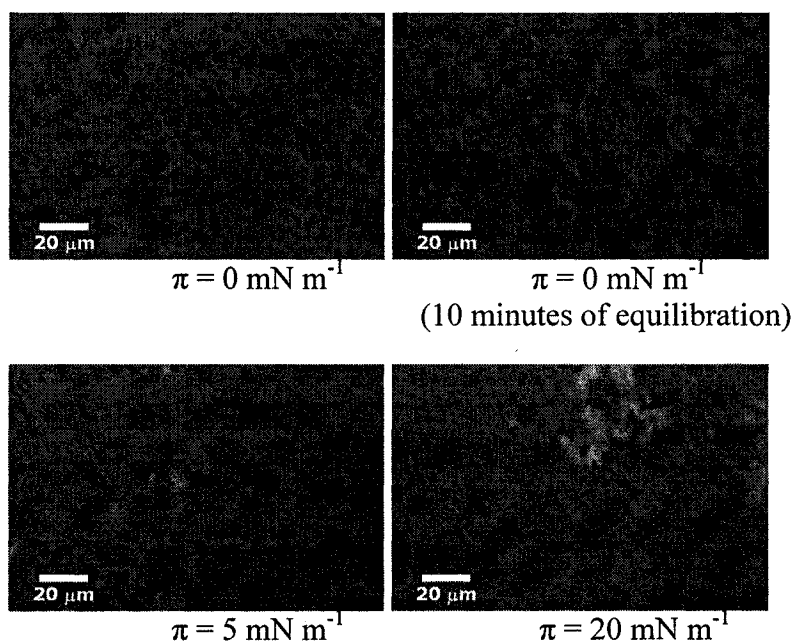


Figure 19. BAM images of enantiomerically pure DPGG at different surface pressures at 33°C .

Another interesting phenomenon of the anisotropic domains observed for enantiomerically pure DPGG is that at higher temperatures, they decrease in size and amount for the same period of equilibration as shown in Figure 19. It shows that at 33°C ,

10 minutes of equilibration do not create visible anisotropic domains as at lower temperatures. At different surface pressures, small anisotropic domains in the monolayer are observed, but the amount and size are decreased. As discussed previously, the increased temperature provides more kinetic energy to the system and the mobility of molecules increases. Packing of the molecules to form the anisotropic domains therefore becomes harder.

3.4. Conclusions

All the phenolic lipids show direct transitions from gaseous phase to condensed phase upon compression at room temperature. Replacing the H atoms in the OH group with methyl groups results in a LE-LC plateau on the isotherm. This may be a result from the disruption of the lateral hydrogen bonding. The *para*-OH group is critical to the monolayer properties of the phenolic lipids. Its removal may cause different patterns of the lateral hydrogen bonds and hence a different orientation of the phenolic lipids at the air/water interface.

Isotherms of enantiomerically pure DPGG shifts to larger molecular area upon equilibration. Its BAM images exhibit anisotropic aggregates whose formation is more favored at lower temperatures and longer equilibration periods.

Chapter 4. Spectroscopic, Computational and Experimental Study on the Phenolic Lipids: from Solution to the Air/Water Interface

4.1. Introduction

In the monolayer study of the phenolic lipids, we found aggregates when the surface areas were far larger than the critical areas of the monolayers (see Figure 9 and Figure 10 (b)). We suspect that the phenolic lipids have already formed intermolecular hydrogen bonds in the spreading solution. In order to probe the hydrogen bonding in the phenolic lipid solutions, studies were performed using IR and ^1H NMR spectroscopies.

Every bond has a frequency of vibration, and IR is a sensitive method to measure the vibration frequencies. A free O-H stretch usually appears at $3650\text{-}3600\text{ cm}^{-1}$ as a sharp, weak peak.⁷⁰ Upon hydrogen bonding, the vibrational motion of hydrogen atoms is more restrained¹¹ and the O-H stretching band becomes a strong and broad peak between 3400 and 3300 cm^{-1} .⁷⁰ Hydrogen bonds can be intermolecular or intramolecular, and intermolecular hydrogen bonds are concentration dependent. A very concentrated solution may only show a broad peak from 3400 to 3300 cm^{-1} . When alcohol or phenol solutions are continuously diluted, the broad peak corresponding to intermolecular hydrogen bonds will be decreased significantly, and a sharp peak will appear at 3600 cm^{-1} , which corresponds to the “free” O-H stretch.⁷⁰

As IR detects vibrations of bonds, NMR senses spin state changes. ^1H NMR can show chemical shifts for the protons in O-H groups with a broad range of absorption

positions. Hydrogen bonds deshield a proton, which results in the chemical shift moving downfield. Therefore, a high diluted solution may show hydroxyl protons between 0.5 to 1.0 ppm, while in a more concentrated solution, the absorption could occur between 4 to 5 ppm.⁷⁰

The phenolic molecules at the air water interface have one more option. Besides intermolecular hydrogen bonds and interactions with like molecules, they can also form hydrogen bonds with subphase water molecules. To address this, the total and free energies of the phenol-water complex and the phenol dimer have been calculated. Differences in interaction can be judged from total and free energy differences when compared to the monomeric systems.

In principle, the phenolic lipids could be hydrogen bonded to each other in the spreading solution and hydrogen bonded to water molecules once spread. It seems reasonable to assume that such a change in hydrogen bonding is not instantaneous, but rather takes time. This was tested by allowing different equilibration periods for the phenolic lipid monolayers. Isotherm and film morphology changes were recorded by Langmuir film balance and BAM.

4.2. Results and Discussion

4.2.1. Monolayer Behavior of Phenolic Lipids upon Equilibration

Studies on monolayers usually allow an equilibration period of 10 to 30 minutes for the evaporation of the spreading solvent and the equilibration of the amphiphiles. Some special cases even allow 60 minutes of evaporation and equilibration.⁷¹ In order to verify if different periods of equilibration have effects on the monolayer behavior of phenolic

lipids, the isotherms and film morphologies of the phenolic lipid monolayers equilibrated with different periods of time are compared.

Ten minutes of equilibration was allowed for all the phenol lipids during which time there were no changes in the isotherms and surface morphologies of the phenolic lipid monolayers. 30 minutes of equilibration was tested for racemic DPGG, and there were no changes in the isotherms, nor in the surface morphologies. In order to give the monolayer sufficient of time to equilibrate, racemic DPGG was allowed to equilibrate overnight (16 hours). The level of the water subphase did change with time, but after equilibration overnight, there was still enough water to keep the monolayer at the surface between the two barriers. Water was added to the subphase (from behind the barriers) in order to take the BAM images and collect the isotherm. Isotherms and BAM images for racemic DPGG with 16 hours of equilibration are summarised in Figure 20.

The isotherms in Figure 20 show that the equilibrated DPGG monolayer is more compressible than the non-equilibrated one. A plateau normally associated with the LE-LC transition is observed on the isotherm for the racemic DPGG monolayer with 16 hours of equilibration. In addition, the surface pressure of the equilibrated DPGG monolayer lifts-off at larger surface areas compared with that of the DPGG monolayer without any equilibration.

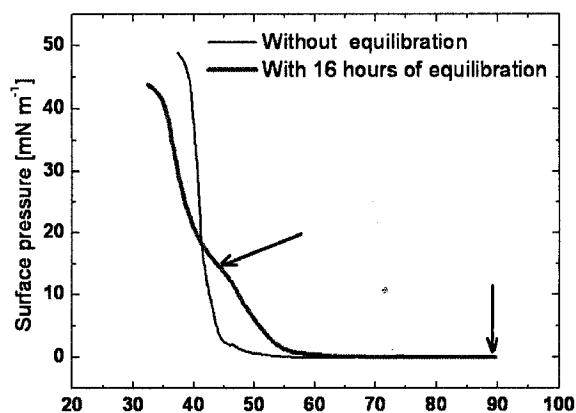


Figure 20. π -A isotherms and BAM images of racemic DPGG monolayer with and without 16 hours of equilibration. (left: without equilibration, $\pi = 0 \text{ mN m}^{-1}$; middle: 16 hours of equilibration, $\pi = 0 \text{ mN m}^{-1}$; right: $\pi = 15 \text{ mN m}^{-1}$.)

The BAM images in Figure 20 show that after 16 hours of equilibration, the DPGG monolayer has large aggregates in addition to many small ones, which are not present without any equilibration. The BAM image for the monolayer at the plateau (the right image in Figure 20) shows the formation of white spots among the small aggregates, which correspond to the formation of 3D solid phases. When the surface pressure reaches 20 mN m^{-1} where the monolayer starts the condensed phase, the white spots are abundant between the large aggregates (data not shown), which was not observed with the DPGG monolayers without any equilibration at the same surface pressure. The formation of 3D

solid phases means less molecules remained at the air/water interface, which agrees well with the isotherm that has a small molecular area for the condensed phase of the monolayer. All this evidence indicates that the molecules rearrange at the air/water interface with time. The rearrangement may be driven by the balance of interactions of the amphiphile with the subphase and with like molecules. It is likely that the lateral hydrogen bonding between the headgroups is broken and is replaced with the hydrogen bonding between the headgroup and the subphase water molecules. That the change of the isotherms and the morphologies of the phenolic lipids only take place with long periods of equilibration indicates that the rearrangement of the molecules at the air/water interface to reach an equilibrium is a very slow process.

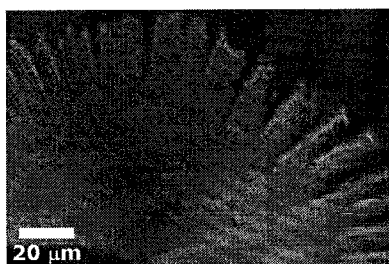


Figure 21. Typical BAM image of DP-3,4,5-MBG (6) after 16 hours of equilibration ($\pi = 0 \text{ mN m}^{-1}$).

Since long equilibration is time consuming, racemic DPGG and DP-3,4,5-MBG were selected as representatives with and without hydrogen bonds between the headgroups; hence 16 hours of equilibration was also performed with DP-3,4,5-MBG. Figure 21 shows a combination of small aggregates with a fan-shaped aggregate, with its round edge split. The splits at the edge were not seen for the DP-3,4,5-MBG monolayers without equilibration. In addition, different-sized fan-shaped aggregates were observed

and some of them are much larger than the aggregates observed without any equilibration.

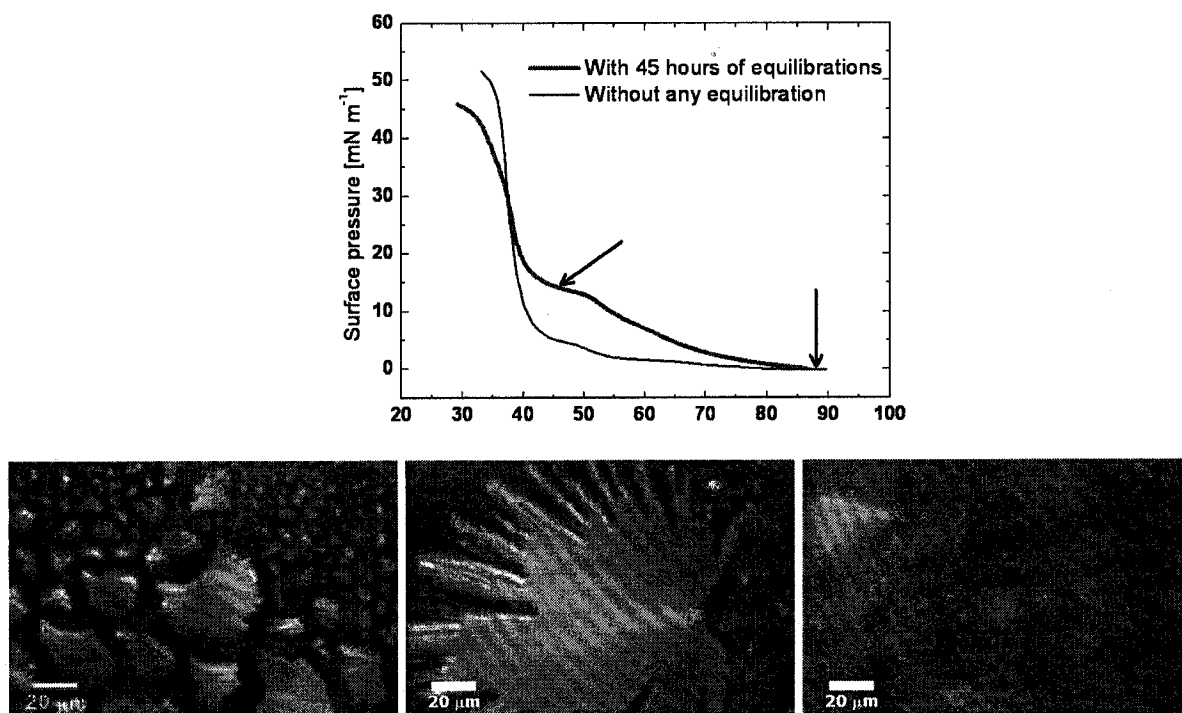


Figure 22. π -A isotherms and BAM images of DP-3,4,5-MBG monolayer with and without 45 hours of equilibration. (left: without equilibration, $\pi = 0 \text{ mN m}^{-1}$; middle: 45 hours of equilibration, $\pi = 0 \text{ mN m}^{-1}$; right: $\pi = 15 \text{ mN m}^{-1}$.)

After 16 hours of equilibration, an even longer period of time (2 nights, 45 hours in total) was allowed before compression in order to check if there are any difference in surface morphology with 16 hours and 45 hours of equilibration. Water was added from behind the barriers regularly in order to keep reasonable water levels. Isotherms and BAM images for DP-3,4,5-MBG with 45 hours of equilibration are summarised in Figure

22. The surface morphology of DP-3,4,5-MBG did not show any pronounced difference between 16 hours and 45 hours equilibration.

It is surprising to know that DP-3,4,5-MBG also showed changes in both its isotherm and film morphology after a long period of equilibration because for this molecule, no H-bonding between the headgroups are possible. However, the changes of the DP-3,4,5-MBG film upon equilibration are not completely unexpected because DP-3,4,5-MBG also formed aggregates at a surface pressure of 0 mN m^{-1} due to van der Waals interactions between the hydrocarbon side chains, possible weak C-H...O H-bonds and π -stacking interactions. Comparing Figure 22 with Figure 21, BAM images show that DPGG exhibits collapse material at the plateau, while DP-3,4,5-MBG does not, and it shows coalescence to condensed phase. The changes in isotherms and BAM images for DP-3,4,5-MBG are very similar to those for racemic DPGG: a more pronounced plateau at higher surface pressures and coexistence of large and small domains, which suggests that upon spreading, the molecules prefer interacting with the subphase water molecules because the oxygen atoms on the headgroup can form hydrogen bonds with the subphase water molecules, which drives the rearrangement of DP-3,4,5-MBG molecules at the air/water interface.

4.2.2. IR Study

All phenolic lipid molecules except for DP-3,4,5-MBG possess hydroxyl group(s) on the aromatic ring, therefore, we expect peaks in the IR spectrum in the O-H stretching region ($3650\text{-}3100 \text{ cm}^{-1}$). If the hydroxyl groups are hydrogen bonded, we can find broad bands between $3400\text{-}3300 \text{ cm}^{-1}$. If the hydroxyl groups are not hydrogen bonded, they

will appear in the IR spectra as sharp bands around 3600 cm^{-1} . This spectroscopic window is particularly attractive, because it is usually unobstructed by other vibrational bands. Unfortunately, proper dilution studies could not be performed because the bands for the saturate solution of the lipids in chloroform are already small. Subtle changes in band shape upon dilution are not reliable when the bands are that small. In addition, due to the sometimes fast evaporation of the chloroform from the cell, we cannot give accurate concentrations.

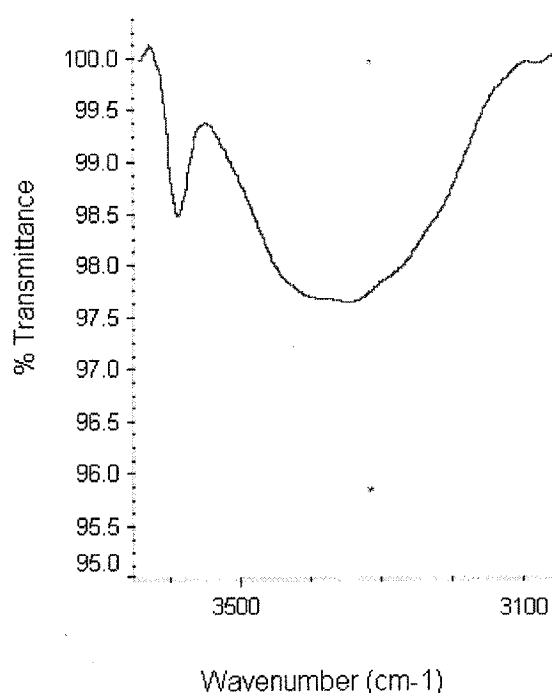


Figure 23. IR spectra of DP-3,5-HBG (**3**) (2 mM).

Except for DP-3,4,5-MBG with its methoxyl groups, the IR spectra for all phenolic lipids show bands for both hydrogen bonded and non-bonded OH groups. As expected, besides unassociated hydroxyl groups, there is also association at these concentrations (around 2 mM). For DPGG and DP-3,4-HBG, we cannot distinguish between inter- and

intramolecular hydrogen bonding, but a prototypical spectrum is shown for DP-3,5-HBG in Figure 23. The broad band at 3300cm^{-1} has to be attributed to an intermolecular O-H...O interaction, as the positions of the OH groups do not allow for an intramolecular interaction.

4.2.3. NMR Study

Unlike the rather well-defined frequencies at which O-H stretching vibrations can be found in the IR, hydroxyl protons in the ^1H NMR spectrum show a wide range of chemical shifts (0.5-5 ppm).⁷⁰ In addition, signals are often broad. This, combined with the fact that one hydroxyl proton integrates for 1 whereas the one signal for most methylene protons of the two chains integrates for 48, can make the detection of the OH signal difficult or even impossible. However, as a technique that can potentially provide us with useful information on hydrogen bonding, we collected ^1H NMR spectra for all the phenolic lipids.

As we have observed when we prepared IR samples, the limited solubility of the racemic phenol lipids make the OH signal difficult to detect. However, the solubility of the enantiomerically pure DPGG is much better than that of the racemic DPGG and the concentration can reach up to 8 mM.

A typical NMR spectrum for enantiomerically pure DPGG (concentration is 8 mM) is shown in Figure 24, and Figure 25 shows the ^1H NMR spectrum of DPGG in a MeOD and CDCl_3 mixture (MeOD: CDCl_3 was 10:1).

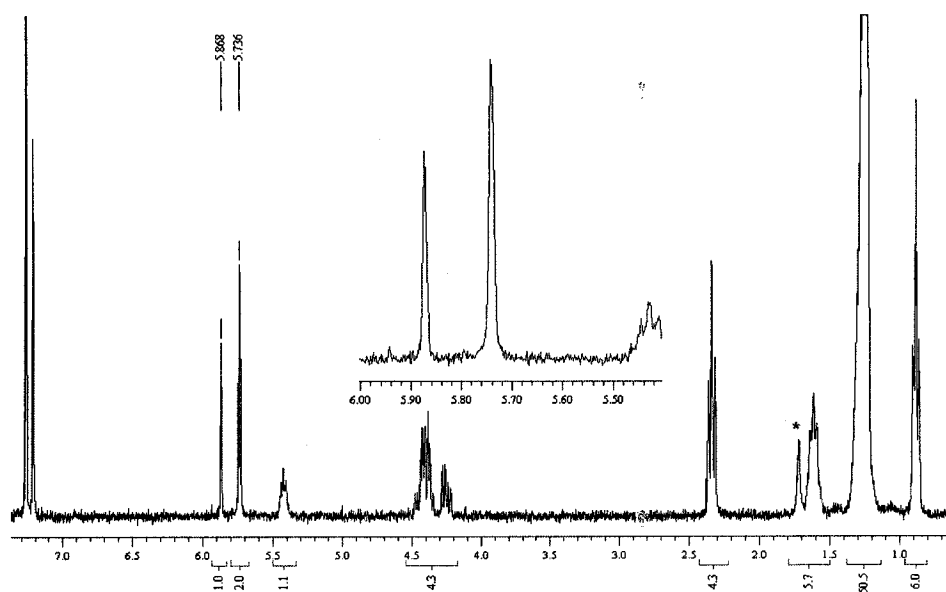


Figure 24. ^1H NMR spectrum of DPGG (8 mM in CDCl_3). (signal “*” is due to traces of water.)

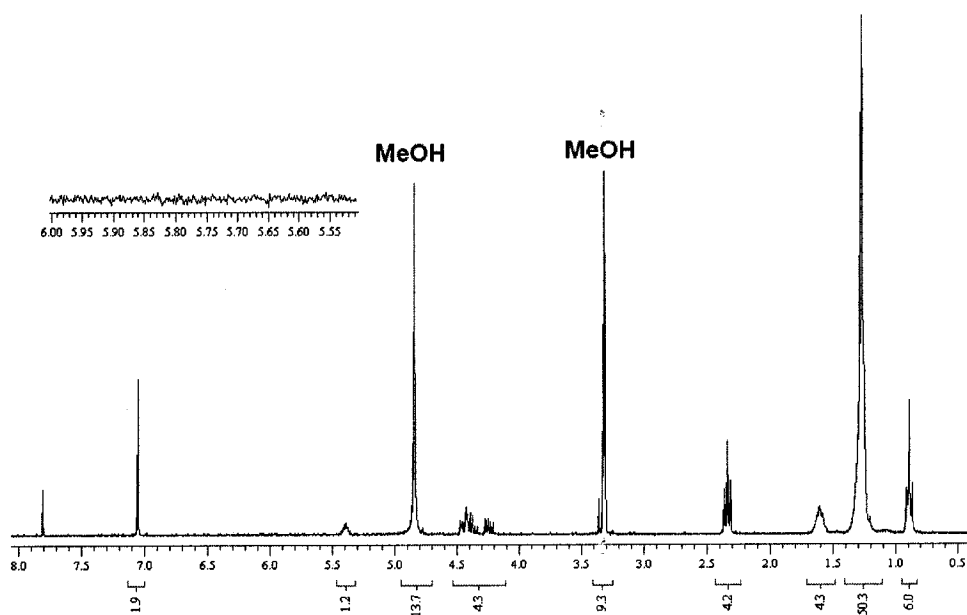


Figure 25. ^1H NMR spectrum of DPGG. (8 mM in $\text{MeOD}:\text{CDCl}_3 = 10:1$.)

In Figure 24, there are two signals with chemical shifts of 5.87 and 5.74 ppm and an integration ratio of 1:2. These signals are not present in Figure 25 (see inset), confirming that they arise from those hydroxyl protons, and that all three hydroxyl hydrogens can be exchanged with deuterium.

Figure 26 shows the change in the OH signals upon dilution from 8 mM to 0.8 mM. While the two OH singlets in spectrum (a) basically do not shift, their intensity decreases in (b) and a new signal appears at higher field (5.55 ppm). This new singlet can be attributed to free, i.e. non-hydrogen bonded, hydroxyl groups.

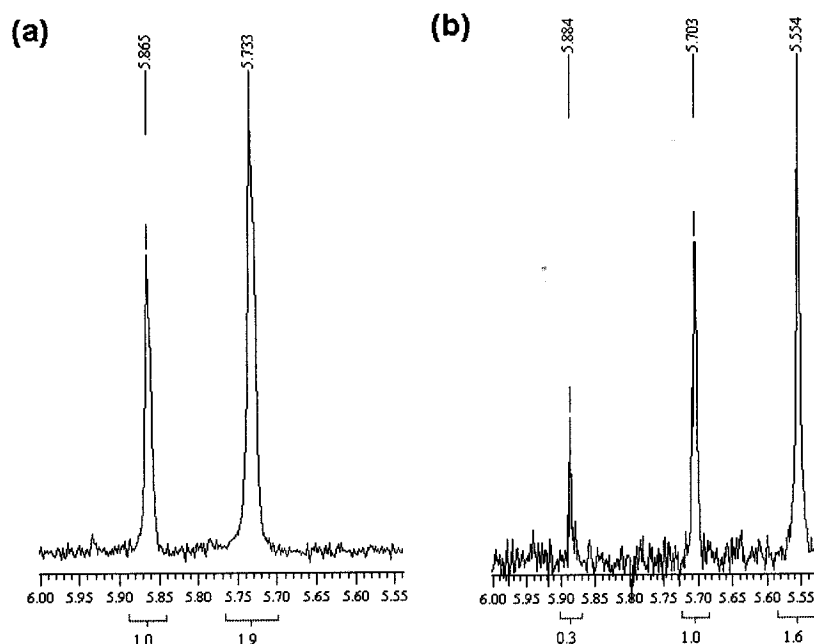


Figure 26. ^1H NMR spectrum of the OH signal of DPGG at different concentrations. (a. 8 mM; b. 0.8 mM.)

Since 0.8 mM is the concentration used in the monolayer studies, this study clearly shows that DPGG molecules are indeed partly hydrogen bonded with each other already in the spreading solution.

Table 2. Chemical shifts δ (ppm) and integration ratios for the hydroxyl protons in the phenolic lipids at different concentrations in CDCl_3 . ("b" indicates broad; "o" indicates overlapped.)

		# of OH signals	δ	Integral ratio
Enantiomerically pure DPGG	8 mM	2	5.87 : 5.73	1:2
	0.8 mM	3	5.88 : 5.70 : 5.55	0.3:1.0:1.6
Racemic DPGG	1 mM	1	5.71 (b)	---
DP-3,4-HBG	4 mM	2	6.25 (b) : 5.93	0.7:1.0
	2 mM	2	6.19 (b) : 5.85	0.7:1.1
	0.8 mM	1	5.90 (b) : 5.84	Overlapping
DP-3,5-HBG	8 mM	1	5.91 (b)	2.1
	4 mM	1	5.40 (o)	1.8
DP-4-HBG	4 mM	1	5.45	1.1
	2 mM	1	5.45	1.0
DP-3-HBG	4 mM	1	5.30 (b)	0.8

Table 2 summarises the hydroxyl proton chemical shifts for DPGG and the other phenolic lipids. As shown in this table, DP-3,4-HBG has two OH proton signals, while all other racemic phenolic lipids have only one signal. Some of the peaks are broad; and some are overlapped, which makes integration impossible. All OH proton signals shift to higher field upon dilution. Racemic DPGG, in principle, should have the same number of signals in the ^1H NMR spectrum as enantiomerically pure DPGG when no optically active solvent is used, but it showed a broad peak with an integral of 2.6 for the three OH protons, which is not expected. While some studies report differences in solubility

between the pure enantiomers and their racemate for strongly hydrogen bonded solids,⁷² one report by Ushio et al.⁷⁴ showed distinct differences in IR and NMR spectra as well as X-ray diffraction patterns for racemic and enantiomerically pure suplatast tosilate, a dimethylsulphonium compound with anti-asthma properties.

4.2.4. Preference of Aggregation

As shown in Chapter 3, aggregate formation between phenolic lipids is observed at very large molecular area ($90 \text{ \AA}^2 \text{ molecule}^{-1}$). IR and ^1H NMR spectra also confirmed that phenolic lipid molecules have already H-bonded with each other in the spreading solution. In order to understand the preference of aggregation for the phenolic lipids, the DPGG molecule is selected as a representative for a computational study. Its headgroup interactions are studied by analysing its dimerisation and trimerisation energy.

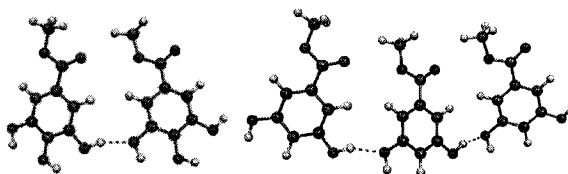


Figure 27. Dimer and trimer configuration for 3,4,5-OH-Me most likely to occur at the air water interface optimized with B3LYP/6-31G(d).

Dimer and trimer configurations for an abbreviated DPGG headgroup (termed 3,4,5-OH-Me) possible at the air/water interface and optimised with the B3LYP/6-31G(d) model chemistry are shown in Figure 27. The dimer total energy is $6.6 \text{ kcal mol}^{-1}$ lower than that of the sum of two monomers, while the trimer total energy is equally $6.1 \text{ kcal mol}^{-1}$ lower than that of the sum of a dimer and a monomer, which indicates that the

formation of aggregates between the headgroups is favorable, and binding energies seem to be additive.

In order to know the effect of side chain length on the dimerisation and trimerisation energy, 3,4,5-OH-Pr (with a 3-carbon side chain) and 3,4,5-OH-Hex (with a 6-carbon side chain) were studied. The dimerisation energy for 3,4,5-OH-Pr is $9.8 \text{ kcal mol}^{-1}$, and the addition of the third monomer is favorable by $6.7 \text{ kcal mol}^{-1}$. For 3,4,5-OH-Hex, the energies are $7.4 \text{ kcal mol}^{-1}$ and $9.8 \text{ kcal mol}^{-1}$ respectively. Although these energies do not show the trend of an increase with increasing length of the side chains (probably due to small changes of the configurations), in all cases, dimers and trimers are favorable, which indicates the favorable formation of aggregates. This agrees well with the experimental results of pre-aggregation in the spreading solution and aggregation formed at high molecular areas before equilibration.

4.2.5. Preference of Hydrogen Bonding to Like Molecules or Water

As shown by the above results, we can assume that phenolic lipids have formed hydrogen bonds in the spreading solution. Now the question is, whether the headgroups will form hydrogen bonds with water molecules instead when the solutions are spread at the air/water interface. In order to answer this question, we chose two model systems for the phenolic lipids: phenol and the *p*-hydroxyl benzoic acid hexyl ester. The two possible interactions in the phenol case are shown in Figure 28.

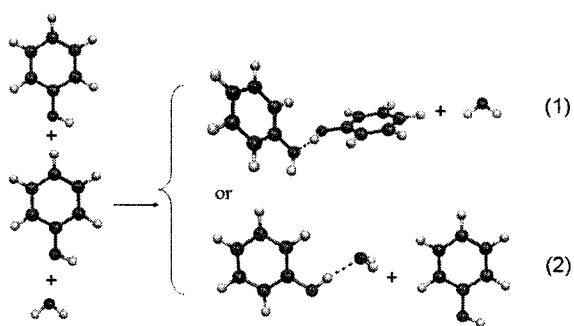


Figure 28. The choices for a phenol molecule to hydrogen bond with another phenol molecule or with a water molecule.

Calculations with the B3LYP/6-31G(d) model chemistry show that (1) with the phenol dimer plus water is 2.2 kcal mol⁻¹ higher in total energy, and 3.3 kcal mol⁻¹ higher in free energy than (2) with the phenol-water complex plus phenol.

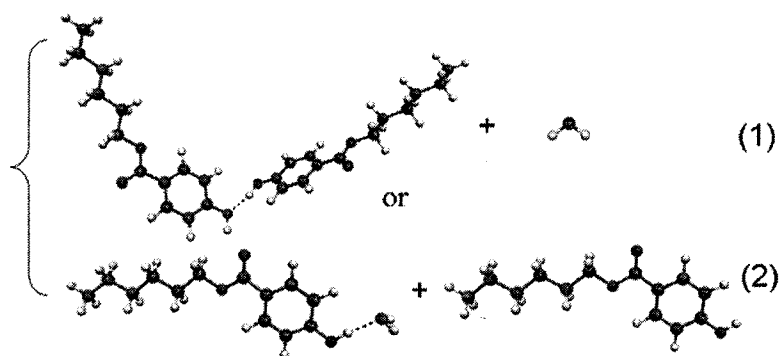


Figure 29. The choices for a *p*-hydroxy benzoic acid hexyl ester molecule to hydrogen bond with another ester molecule or with a water molecule.

The hexyl ester with its interactions is shown in Figure 29. With +3.2 kcal mol⁻¹ for total energy and +5.5 kcal mol⁻¹ for free energy, the ester interaction with water is even

more favorable, indicating that the longer the side chains, the more favorable the interaction with water will be. Assuming that these two small models represent DPGG and the other phenolic lipids adequately, the phenolic lipids seem to favor hydrogen bonds with water molecules instead with another lipid molecule after they are spread at the air/water interface. This fits well with what was observed in the equilibration study of the typical phenolic lipids.

4.3. Conclusions

The experimental study of a typical phenolic lipid monolayer showed that given enough equilibration time, the phenolic lipids rearrange, which results in significant changes in the shape of the isotherms and some changes in their BAM images.

Hydrogen bonds in dilute solutions are apparent from IR spectra, but in particular ^1H NMR spectra showed that, upon dilution to the target concentration of 0.8 mM, the hydroxyl signals shifted to a higher field with low field signal still present. All observations indicate that there are hydrogen bonds between the phenolic lipid molecules in the spreading solutions.

The computational study showed that dimerisation and trimerisation of the phenolic lipid headgroups are energetically favorable and the binding energies seem to be additive. In addition, although the lipids hydrogen bond with each other, after spreading at the air/water interface, they rearrange to form hydrogen bonds with subphase water molecules, thus confirming the hypothesis drawn from the equilibration times.

Chapter 5. Computational Investigation of Small Assemblies of Substituted Model Phenols

5.1. Introduction

Our experimental studies showed that phenolic lipids, with structures as shown in Figure 5, behaved differently at the air/water interface, especially the phenolic lipid with two *meta* hydroxyl groups (DP-3,5-HBG), whose isotherms shifted to a larger molecular area, and Brewster angle microscopy images differ significantly from those of the other phenolic lipids. Since all the phenolic lipids have exactly the same side chains, the only possible reason causing these differences should be the interactions between the headgroups. Two groups working on the bilayer and monolayer behavior of DPGG (1) explained the unusual properties of this molecule through H-bonding between its headgroups.^{1, 3} It is possible that the difference in the monolayer behavior of the other phenolic lipids is also caused by hydrogen bonding. In order to test this hypothesis, we calculated interactions between the phenolic lipid molecules by allowing H-bonding between the hydroxyl groups. Considering the computational capacity and cost, and the fact that the differences in the monolayer behavior is solely due to the headgroup region, we simplified the systems by only taking the aromatic headgroup of the lipids with a reasonable chain length.

5.2. Selection of Model Chemistry

Selection of the model chemistry, i.e. the method and the basis set, is based on both the consideration of computational cost and quality of the results. The quality of the

results is judged through comparison of calculated spectroscopic properties and geometrical information with available experimental data from the literature, as well as through verification of H-bonds in known systems. We are particularly interested in whether the inexpensive semiempirical PM3 method shows an adequate performance, as it would be the method of choice for larger assemblies of larger model systems later.

5.2.1. Comparison of Calculated Spectroscopic Properties and Geometry Information with Available Experimental Data

Phenol, the phenol dimer and the phenol-water complex are used to benchmark the model chemistries. Comparisons with experimental results are done for calculated geometries and rotational constants of phenol and the phenol dimer and for phenol-water complex geometries. The semiempirical PM3, ab initio HF and MP2, and the density-functional theory functionals B3LYP and PBE0 are tested. For B3LYP, the basis set size is varied.

All the calculated and experimental values for geometries and rotational constants can be found in Tables in Appendix B. Figure 30 shows the performance of the selected model chemistries on the geometrical parameters of phenol. Raw data can be found in Table B1 of the Appendix. Relative differences have been calculated using microwave data as shown in Table B1 of the Appendix and have been plotted so that a positive value indicates an overestimation by the model chemistry.

As expected, in general, errors are larger for the PM3 and HF methods, especially for parameters that involve atoms of interest for H-bonding (O and H) of the hydroxyl group. The performance is much improved for MP2 and density-functional theory

methods. Again as expected, the basis set dependence of the relative differences for B3LYP is not pronounced, but certain trends can be seen. For example, including polarisation functions on hydrogen atoms (as in the 6-31G(d,p) basis set) decreases the difference for the O-H distance, and therefore indicates a better description of the hydroxyl group. In contrast, including diffuse functions on the heavy atoms (as for 6-31+G(d, p)) leads to a larger difference in the C-O-H bond angle and is therefore counterproductive.

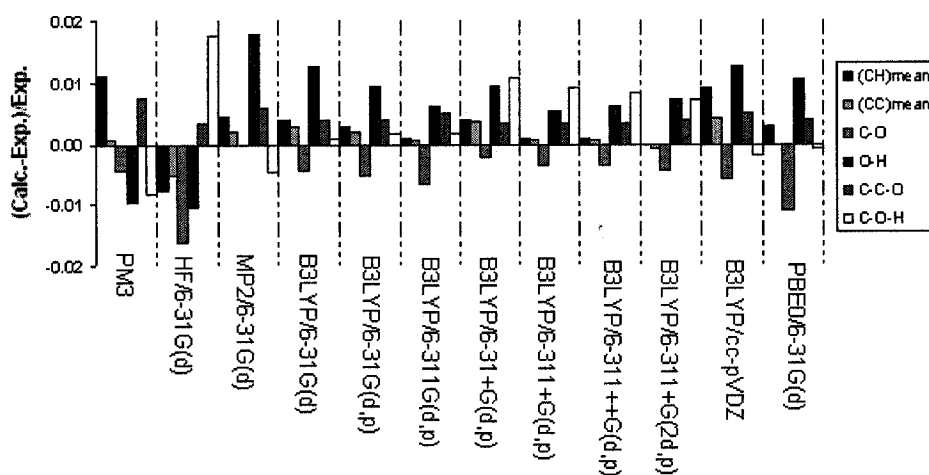


Figure 30. Relative differences between the calculated and experimental geometrical parameters for phenol. (see Appendix B Table B1 for values.)

Figure 31 shows the performance of the same model chemistries for the three rotational constants of phenol, with the raw data given in Table B2 of the Appendix. The overall conclusions are similar to those above. The performance of the HF method is worst. MP2 as the computationally most expensive method shows a very good

performance, but especially that of the relatively small B3LYP/6-31G(d) model chemistry is noteworthy, probably due to a fortuitous cancellation of errors.

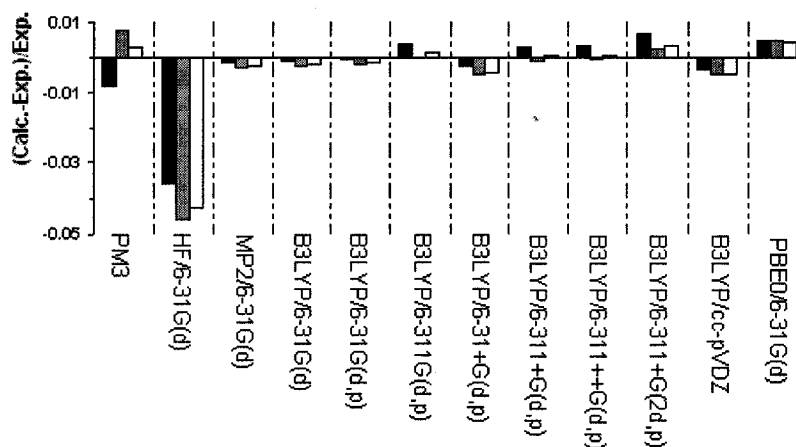


Figure 31. Relative differences between the three calculated and experimental rotational constants for phenol for various model chemistries. (■A, ▒B, □C, see Appendix B Table B2 for values.)

The hydrogen-bonded phenol dimer configuration from ref. 75 is shown in Figure 32. Figure 33 has the relative differences for its geometrical parameters (raw data in Table B3 of the Appendix B) and Figure 34 has the relative differences for the rotational constants (raw data in Table B4 of the Appendix B). For HF, MP2, B3LYP and PBE0, the conclusions are similar to those for Figures 30 and 31 above. In particular, B3LYP/6-31G(d) performs no worse than the larger basis sets. PM3, on the other hand, determines an O1-O2-C7-C8 dihedral angle (Figure 33) that is too large (50° instead of the experimental 15°). This torsion does not seem to lead to a dramatic change in terms of rotational constants (Figure 34), though, because all model chemistries, including PM3, show a similar performance, that for the expensive MP2 being best.

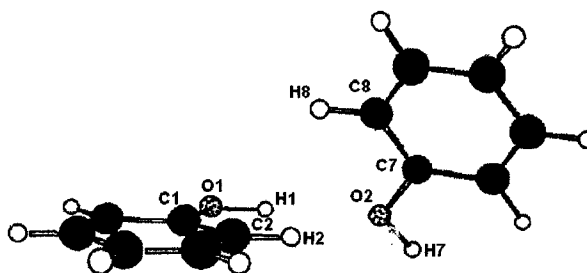


Figure 32. Orientation of the two phenol monomers in the dimer from ref. 75. (from microwave spectroscopy.)

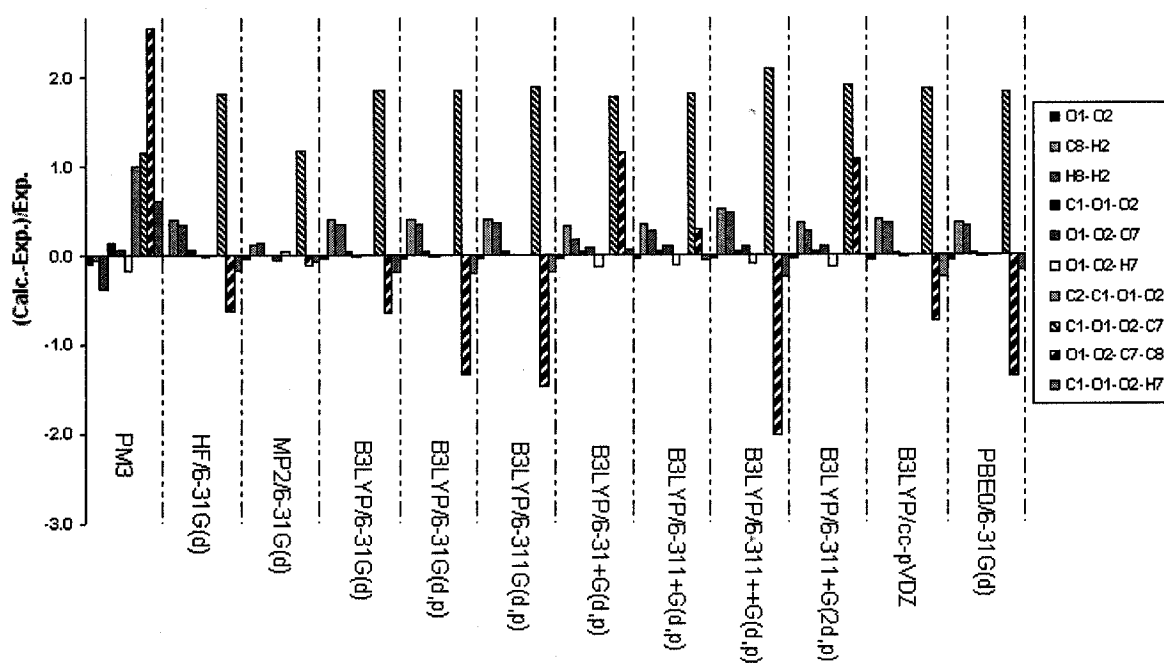


Figure 33. Relative differences between the calculated and experimental geometrical parameters of the phenol dimer. (see Appendix B Table B3 for values.)

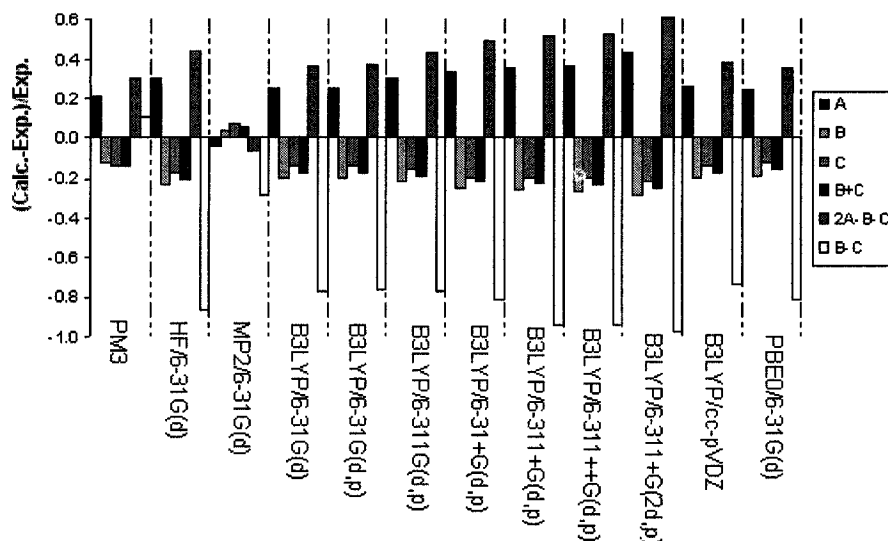


Figure 34. Relative differences between experimental and calculated rotational constants for the phenol dimer. (see Appendix B Table B4 for values.)

Figure 35 shows the geometrical arrangement for the phenol-water complex. As shown, ϕ is the angle between O(H₂O)-O(phenol) and H on the OH of phenol (the deviation from linearity). β is the angle between O(H₂O)-O(phenol) and the median of the HOH angle (water). γ is the angle between C-O(phenol) and O(H₂O). Figure 36 has the relative differences for the geometrical parameters and rotational constants (raw data in Table B5 of the Appendix B). Figure 36 shows that all the selected model chemistries perform well in the calculation of all geometrical parameters except ϕ . B3LYP/cc-pVDZ gives a much smaller value of 1.1° compared to the microwave data of 5.0°, but both values can still be considered small. B3LYP/6-31G(d) has the best results among the selected model chemistries, while including diffuse functions improves the calculation of β but worsens that for ϕ . In terms of rotational constants, all model chemistries perform well, including PM3.

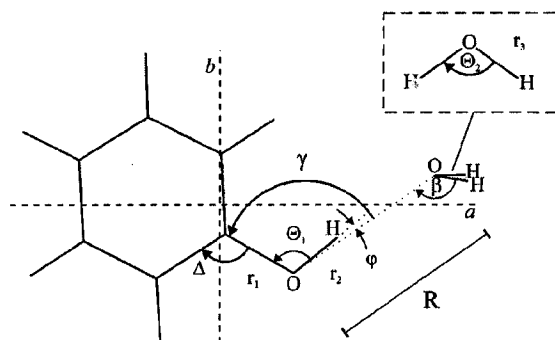


Figure 35. Relative orientation of phenol and water molecules in the complex from ref.

76.

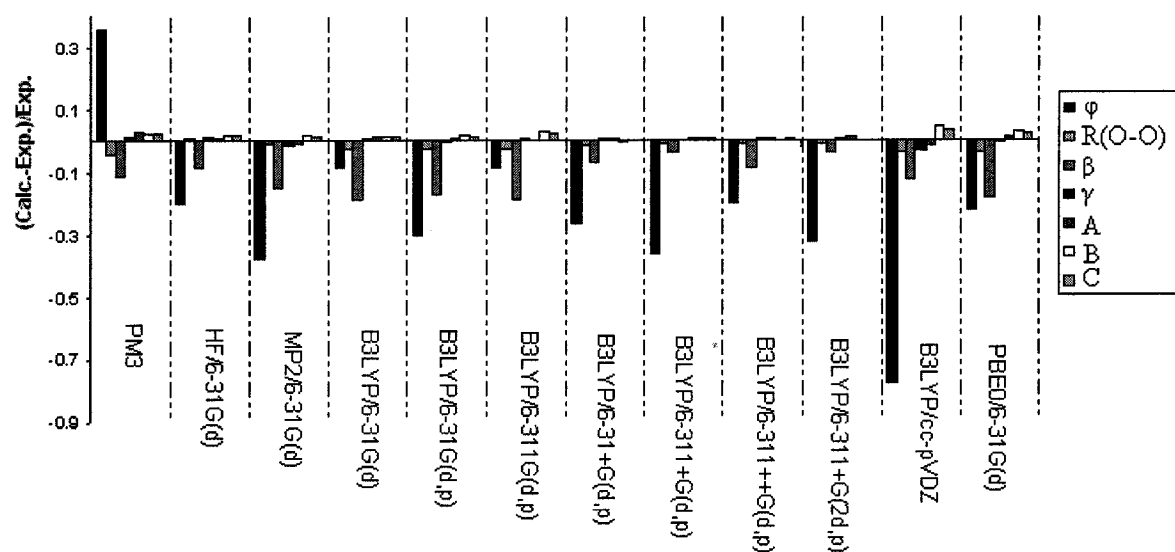


Figure 36. Relative differences between the calculated and experimental geometrical parameters and three rotational constants for the phenol–water complex. (See Appendix B Table B5 for values.)

From the presented data, it seems that B3LYP will be a good method to use for our intended studies. The 6-31G(d) basis set, in particular, also seems a good choice, even

though, in principle, polarization functions on hydrogen atoms should be used when H-bonding is studied. We will focus on this problem next.

5.2.2. Location of Intermolecular and Intramolecular Hydrogen Bonds

Intermolecular hydrogen bonding between phenol molecules is well accepted by all chemists. Mikami et al. verified hydrogen bonding in phenol dimers and phenol trimers in their IR and Raman spectroscopic studies.⁷⁷ Meanwhile, they stated the configuration of the phenol trimer is cyclic as shown in Figure 37.

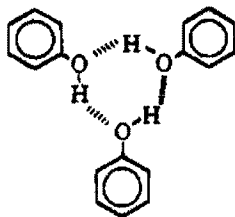


Figure 37. Proposed phenol trimer configuration by Mikami et al. from ref. 77.

An intramolecular hydrogen bond between the two hydroxyl groups in the catechol (1,2-dihydroxylbenzene) molecule was suggested from microwave^{78, 79} and FT-IR studies.^{80, 81} In a microwave study by Onda et al., r_s coordinates of the hydrogen atoms in the two hydroxyl groups were compared with those from three ab initio optimised structures and coincided well with the structure that had an intramolecular hydrogen bond.⁷⁸ FT-IR studies by Foti et al. showed two sharp equal intensity bands in the O-H stretching vibration region at 3615.0 cm^{-1} and 3569.6 cm^{-1} , which correspond to the “free” O-H and the intramolecularly H-bonded O-H, respectively. Upon addition of a small amount of a hydrogen bond acceptor, e.g. DMSO, the “free” O-H band shifted 400 cm^{-1} lower in frequency, but the intramolecularly H-bonded one did not.^{80, 81} The

difference in the two O-H bands' behaviors suggested an intramolecular H-bond in catechol. The next check is, therefore, to see which basis set reproduces the intermolecular H-bonding between two phenol molecules and the intramolecular H-bond between the two hydroxyl groups in catechol.

We have used the quantum theory of Atoms in Molecules to locate all BCPs, which is giving all interactions between atoms, and from this have constructed the molecular graphs (the network of bonding interactions) for phenol, its dimer and catechol in Figure 38.

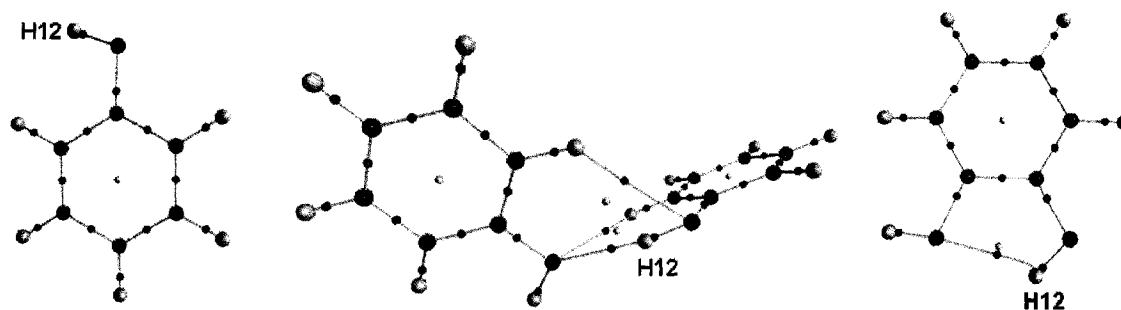


Figure 38. The network of bonding interactions (molecular graph) for phenol, the phenol dimer and catechol from B3LYP/6-31G(d). (Bond critical points are given as small red spheres.)

As can be seen, for phenol the network of bonds is recovered, while for the phenol dimer, in addition, weak bonding interactions are also uncovered. The dimer is stabilised by the expected hydrogen bond, but two additional C-H \cdots O interactions are also found. Because they are expected to be energetically much less important than the O-H \cdots O interaction, they will not be studied further here. Catechol, as shown in Figure 38, possesses an intramolecular H-bond.

The bond critical point for the O-H...O interaction in the phenol dimer is found with all basis sets used, and Table 3 gives those basis sets with the electron density and Laplacian values found at the BCP.

Table 3. Electron density ρ (au) and Laplacian $\nabla^2\rho$ (au) at the bond critical point of the O-H12...O interaction in the phenol dimer calculated with different model chemistries

	ρ	$\nabla^2\rho$
B3LYP/6-31G(d)	0.0280	0.0224
B3LYP/6-31G(d,p)	0.0269	0.0199
B3LYP/6-311G(d,p)	0.0261	0.0251
B3LYP/6-31+G(d,p)	0.0260	0.0193
B3LYP/6-311+G(d,p)	0.0247	0.0238
B3LYP/6-311++G(d,p)	0.0249	0.0239
B3LYP/6-311+G(2d,p)	0.0280	0.0224
B3LYP/cc-pVDZ	0.0275	0.0251
PBE0/6-31G(d)	0.0290	0.0238
MP2/6-31G(d)	0.0269	0.0220

According to the experimental study performed by Ranganathan et al., typical O-H...O hydrogen bonds have their electron density at the bond critical point within 0.03-0.39 $\text{e}\text{\AA}^{-3}$ (0.0044-0.0578 au).⁸² Table 3 shows that all model chemistries provide values for the electron density within the typical O-H...O hydrogen bond range. Meanwhile, the Laplacian values calculated by all model chemistries fall within Bader's range for hydrogen bonds from 0.015 to 0.15 au.³⁰ MP2/6-31G(d), as an expensive but more

accurate method, is included in Table 3 for comparison. As shown in Table 3, B3LYP/6-31G(d) provides results very close to MP2/6-31G(d). In general, adding polarisation to hydrogen atoms decreases the electron density, but as expected, the overall changes are not large.

Figure 39 shows the relative difference between phenol monomer and dimer atomic properties calculated for H12 (Figure 38) with different model chemistries (raw data in Table B6 of the Appendix B), and in accord with Table 3, there is not a large basis set dependence in the data.

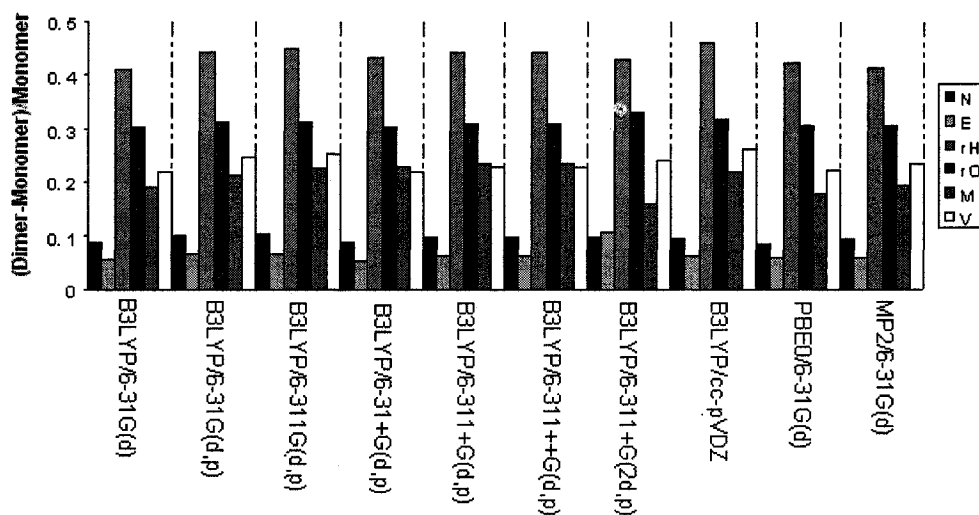


Figure 39. Relative difference between phenol monomer and dimer atomic properties (H12) calculated with different model chemistries. (N: atomic population; E: atomic energy; r_H : radius of hydrogen atom involved in hydrogen bond; r_O : radius of oxygen atom involved in hydrogen bond; M: dipolar polarisation; V: atomic volume.)

In contrast, not all model chemistries used show the bond critical point for the O-H...O interaction in catechol as given in Table 4. A larger basis set in terms of polarisation functions, B3LYP/6-31+G(2df,pd), is included for comparison, but it does not show a bond critical point for the O-H...O interaction either.

Table 4. Electron density ρ (au) and Laplacian $\nabla^2\rho$ (au) at the bond critical point of the intramolecular hydrogen bond in catechol calculated with different model chemistries

	ρ	$\nabla^2\rho$
B3LYP/6-31G(d)	0.0183	0.0201
B3LYP/6-31G(d,p)	0.0184	0.0201
B3LYP/6-311G(d,p)	No bond critical point	
B3LYP/6-31+G(d,p)	0.0172	0.0199
B3LYP/6-311+G(d,p)	No bond critical point	
B3LYP/6-311++G(d,p)	No bond critical point	
B3LYP/6-311+G(2d,p)	No bond critical point	
B3LYP/cc-pVDZ	0.0192	0.0208
PBE0/6-31G(d)	0.0192	0.0215
B3LYP/6-31+G(2df,pd)	No bond critical point	

As Table 4 shows, all selected model chemistries give electron densities within Ranganathan et al.'s typical O-H...O hydrogen bond range (0.0044-0.0578 au)⁸² and the Laplacian within Bader's hydrogen bond range (0.015-0.15 au).³⁰ As expected, the electron density at the BCP of the intramolecular H-bond in catechol (Table 3) is lower than that at the BCP of the intermolecular H-bond in the phenol dimer (Table 4), because

the interaction is more strained in catechol. For many model chemistries, no BCP is found due to the small increase in O-H...O distance, which causes coalescence of the BCP and the ring critical point (RCP) (compare their proximity in Figures 38 or 40).

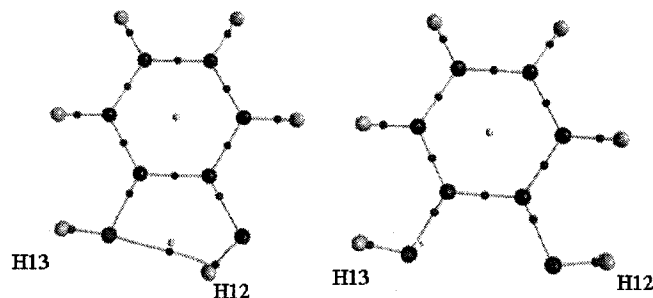


Figure 40. The hydrogen bonded isomer of catechol (left) and its rotamer (right).

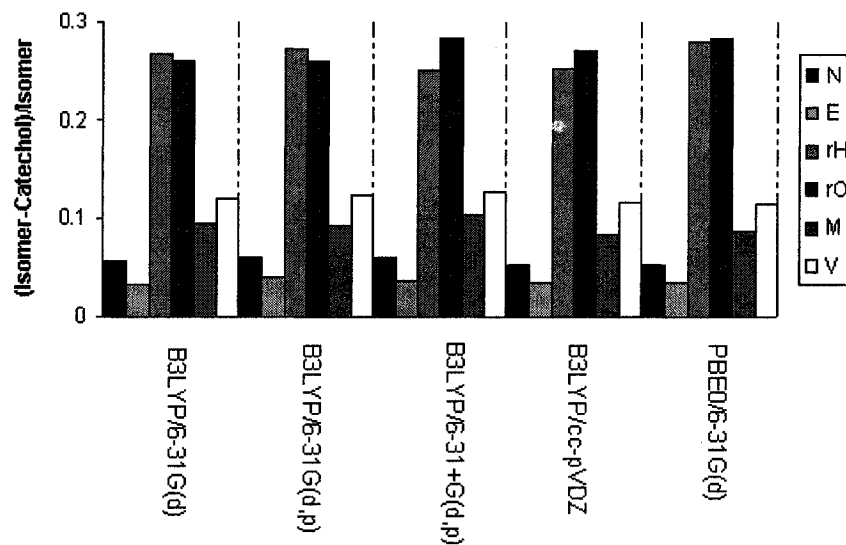


Figure 41. Relative difference between atomic properties of catechol and its isomer calculated with different model chemistries. (N: atomic population; E: atomic energy; r_H : radius of hydrogen atom involved in the hydrogen bond; r_O : radius of oxygen atom involved in hydrogen bond; M: dipolar polarisation; V: atomic volume.)

To evaluate the changes in the atomic properties upon intramolecular H-bonding, the catechol rotamer from Figure 40 was chosen for the “non-interacting” hydrogen atom. Figure 41 shows the relative difference between atomic properties of H12 in catechol and its isomer calculated with different model chemistries (raw data in Table B7 of the Appendix B). Similar to Figure 39, Figure 41 also shows that there are no significant differences between the results obtained from different model chemistries, and as for the electron densities in Tables 3 and 4, values in Figure 39 are larger than those in Figure 41.

Overall, B3LYP/6-31G(d) emerges as a viable model chemistry. Therefore, the B3LYP/6-31G(d) model chemistry is used in this study to calculate small assemblies of phenolic esters and entire lipid molecules.

5.3. Small Assemblies of Model Phenolic Esters

The purpose of simulating small assemblies of the phenol lipid headgroups is to understand their gas phase interaction and to identify assemblies that are feasible at the air/water interface. Results were obtained with B3LYP/6-31G(d).

The focus is on small phenol esters. First, the conformations of the monomer methyl esters are explored. Then dimers and trimers are constructed to evaluate possible hydrogen bonding patterns. Propyl and hexyl esters are included to test for effects of the growing chain length. Configurations of the dimers and trimers without any imaginary frequencies are compared in terms of the free energy (ΔG) and zero point energy corrected total energy (ΔE) (for trimers with six carbon atoms, only total energies are compared because frequency calculations were computationally too demanding. Finally, the results at the B3LYP/6-31G(d) level are compared to those obtained with PM3. This

approach represents only the initial steps in a much larger computational study that includes explicit water molecules as well as longer chains and even the dual chains of the glycerol backbone. These issues will be addressed in Chapter 6.

In the following, a notation code is used for the model esters, in which the position of a hydroxyl group is given by a number, followed by OH for hydroxyl, followed by Me, Pr, or Hex for a methyl, propyl or hexyl ester, respectively. Thus, 3,4,5-OH-Me denotes methyl 3,4,5-trihydroxybenzoate (gallic acid methyl ester), a methyl ester with three hydroxyl groups in 3-, 4- and 5- position.

5.3.1. Headgroup Structure in Model Methyl Esters

Starting with the smallest headgroups, i.e. only the aromatic ring and hydroxyl group(s), compounds with two or three hydroxyl groups have two conformations each, shown in Figure 42.

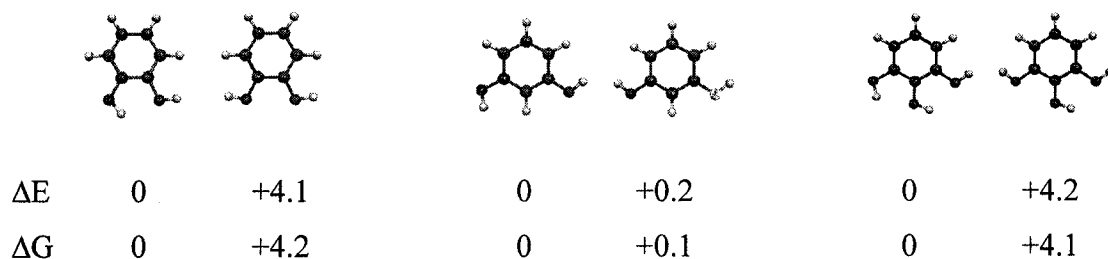


Figure 42. Possible conformers for two-OH and three-OH headgroup systems. Relative energies in kcal mol⁻¹.

For catechol (1,2-dihydroxybenzene) and the molecule with three hydroxyl groups (1,2,3-trihydroxybenzene), the free energy differences of 4.2 kcal mol⁻¹ and 4.1 kcal mol⁻¹ indicate the conformer with the lower energy has a population >99.99%. In contrast, for

1,3-dihydroxybenzene, the small free energy difference of 0.1 kcal mol⁻¹ indicates an almost 1:1 distribution (55:45). Despite the small difference in energy, the conformer with the higher population is selected to build the esters.

In order to construct methyl esters, a -COOMe group needs to be added to the headgroups. Two different configurations, *cis* and *trans*, are possible for an ester and Figure 43 shows the energy difference between the *cis* and *trans* forms for 3,4,5-OH-Me. In accord with data on other esters,⁸³ the *trans* configuration is 11.9 kcal mol⁻¹ lower in total energy and 11.8 kcal mol⁻¹ lower in free energy, therefore, all esters will be constructed with the *trans* configuration.

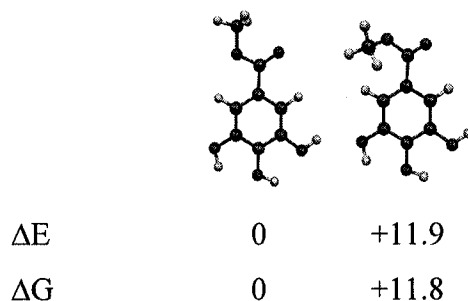


Figure 43. Energy differences for methyl ester conformations with the methyl group *trans* (left) or *cis* (right) to the aromatic ring. Relative energies in kcal mol⁻¹.

Figure 44 shows that even for the methyl esters of the monohydroxybenzenes, there is more than one conformer. For 3-OH-Me (methyl ester, OH in 3-position), the conformers are 44%:26%:16%:14% populated while there is an almost equal population for 4-OH-Me. The configurations with the largest population are selected to construct dimers and trimers.

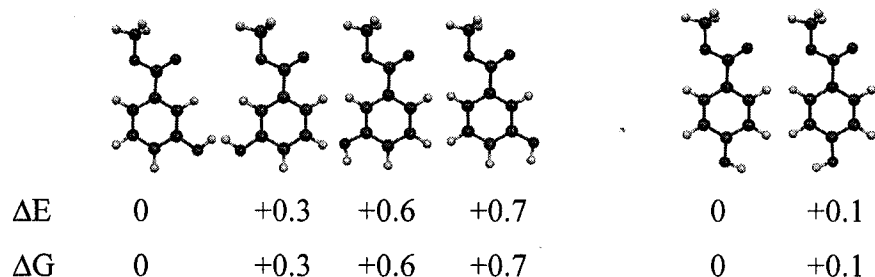


Figure 44. Methyl ester conformers for molecules with one OH group. Relative energies in kcal mol⁻¹.

Figure 45 shows possible conformers for molecules with two OH groups. The conformers for 3,4-OH-Me are 55%:28%:10%:7% populated. For 3,5-OH-Me, the conformer with the lower free energy has a population of 66%.

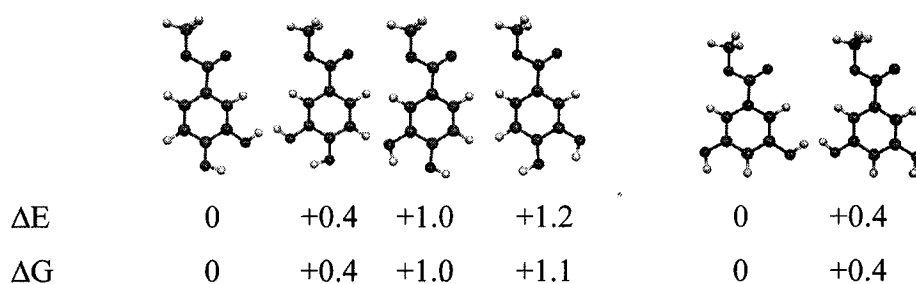


Figure 45. Methyl ester conformers for molecules with two OH groups. Relative energies in kcal mol⁻¹.

Similar to 3,5-OH-Me, for the molecule with three OH groups, there are two possible ester forms, which are shown in Figure 46. The free energy difference of 0.4 kcal mol⁻¹ between the two conformers indicates a population of 66% for the conformer with the lower free energy, again similar to 3,5-OH-Me.

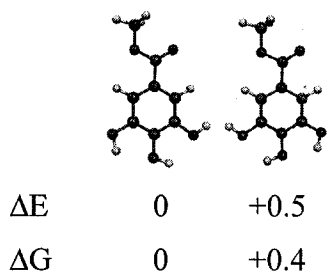


Figure 46. Methyl ester conformers for the molecule with three OH groups. Relative energies in kcal mol⁻¹.

For all methyl esters, ΔE values are very similar to ΔG values, indicating that differences in entropy are negligible. Even though we have calculated equilibrium compositions for the methyl esters, these should not be given too much importance as they can change easily when water is involved (as it is in the experiments).

5.3.2. Dimers

The most stable methyl esters from 5.3.1 have been chosen to construct the dimers. The potential energy surfaces for the dimers of the methyl esters have not been explored fully or systematically. Rather, different plausible orientations were chosen and their geometries fully optimised. Many “intuitive” orientations were in fact not minima. Frequency calculations showed all assemblies to be minima, except where indicated otherwise. The chains in the optimized methyl ester dimers were then extended for propyl and hexyl esters. In the Figures, dashed lines correspond to H-bonds as plotted from Molekel.

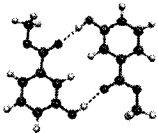
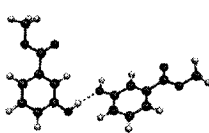
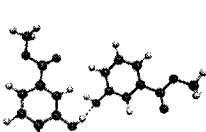
5.3.2.1. Methyl Esters

Possible dimer configurations for 3-OH-Me and 4-OH-Me are shown in Figure 47. It shows that for 4-OH-Me, the H-bonding pattern involving the carbonyl group (configuration (a)) is 3.3 kcal mol⁻¹ lower in total energy and 3.2 kcal mol⁻¹ lower in free energy than the side-on configuration (configuration (b)), which gives a population of the former of 99.6%. However, since the H-bonding pattern involving the carbonyl group cannot occur at the air/water interface (the alkyl side chains would have to twist out of the most favourable all-*trans* conformation; see Chapter 5.5.1), it is not the focus of this study. Similar to 4-OH-Me, 3-OH-Me(a) has an even larger population (effectively 100%) because its H-bonding pattern involves both carbonyl groups. For the same reason as given above, this study will not focus on that kind of configuration.

For the phenolic lipids with more than one hydroxyl group on the aromatic ring, there are obviously more possibilities to construct dimer. Figure 48 shows the dimer configurations for phenolic lipids with more than one hydroxyl group on the aromatic ring.

All configurations shown in Figure 48 are minima on the potential energy surface as verified by frequency calculations, except for 3,4,5-OH-Me(a), which has an imaginary frequency of -11 cm⁻¹ corresponding to the wobble of one monomer. But when PBE0/6-31G(d) is used, no imaginary frequency is observed, and 3,4,5-OH-Pr with the same configuration with B3LYP/6-31G(d) does not show an imaginary frequency, either. We can therefore ignore the imaginary frequency.

3-OH-Me

			
	a	b	c
ΔE	0	+8.8	+9.6
ΔG	0	+7.5	+9.1

4-OH-Me

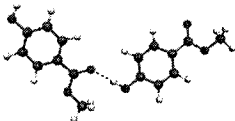
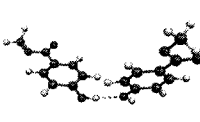
		
	a	b
ΔE	0	+3.3
ΔG	0	+3.3

Figure 47. Dimer configurations for 3-OH-Me and 4-OH-Me. Relative energies in kcal mol⁻¹.

For 3,4-OH-Me, configuration (a) which involves the carbonyl group in H-bonding again has the lowest energy. As mentioned above, this kind of arrangement is not possible to occur at the air/water interface, and is included, but not further explored. The two configurations (b) and (c) for 3,4-OH-Me have similar total energies, but as can be seen, the entropy contributions are quite different. The configuration 3,4-OH-Me(c) with the two aromatic rings parallel (but off-set) to each other and two intermolecular H-bonds is similar to the packing pattern for catechol in crystals obtained by X-ray diffraction,⁸⁴ which shows that higher energy configurations can be important in condensed phases, because of the ester group in 3,4-OH-Me, where the carbonyl oxygen atom can take part

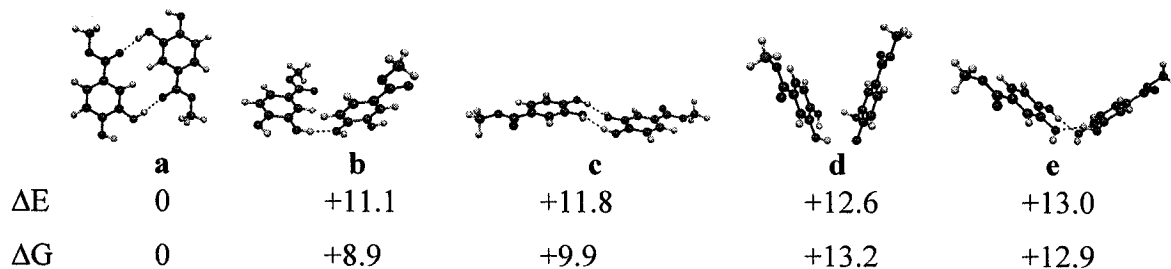
in the H-bonding network, this configuration is $11.1 \text{ kcal mol}^{-1}$ higher in energy than (a). 3,4-OH-Me(d) with its facing aromatic rings (possible π -stacking interactions) is even higher in energy. Configurations for 3,5-OH-Me and 3,4,5-OH-Me do not offer much more insight, with the possible exception of 3,5-OH-Me(b) and 3,4,5-OH-Me(c).

Figures 47 and 48 show that all phenolic lipids could adopt side-on arrangements, as e.g. in 3,5-OH(c) and (d) at the air/water interface. When lipids take the side-on arrangements, it is possible for the monomers to rotate around the H...O-H hydrogen bond axis so that all the side chains are erect normal to the air/water interface, resulting in all the side chains orienting alike. In addition, though, 3,5-OH-Me(b) and 3,4,5-OH-Me(c) are also possible at the air/water interface. For DP-3,5-HBG, an arrangement as in 3,5-OH-Me(b) would lead to different orientations of the side chains, and such arrangements would imply that the monomers occupy larger areas at the air/water interface, which could explain why the DP-3,5-HBG isotherm is shifted to a much larger molecular area compared to that of the other phenolic lipids.

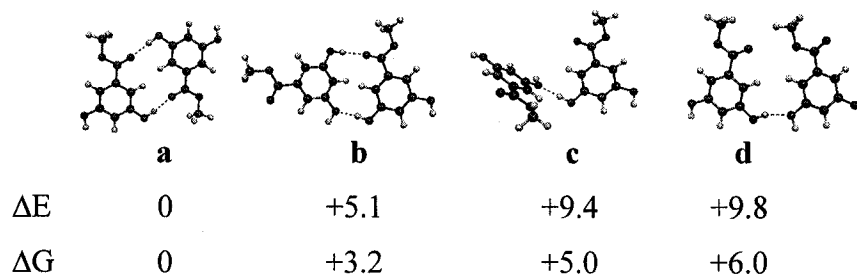
These configurations involve the carbonyl group but could occur at the air/water interface, which is especially interesting because 3,5-OH-Me(b) is a relatively low-energy configuration. In contrast, 3,4,5-OH-Me(c) is not particularly low in energy because the arrangement of the two monomers is significantly more "bent" (Figure 49) due to the extra hydroxyl group, which is absent in 3,5-OH-Me. The X-ray diffraction study on the crystal structure of 3,4,5-OH-Me (gallic acid methyl ester) by Sekine et al. stated that one of the OH group was H-bonded with the carbonyl group of the other monomer, with the O...O distance and O-H...O angle equal 2.671 \AA and 177° .⁸⁵ O...O

distance and O-H...O angle for 3,4,5-OH-Me(a) in Figure 48 are 2.80Å and 178.3°, which agree well with the experimental data.

3,4-OH-Me



3,5-OH-Me



3,4,5-OH-Me

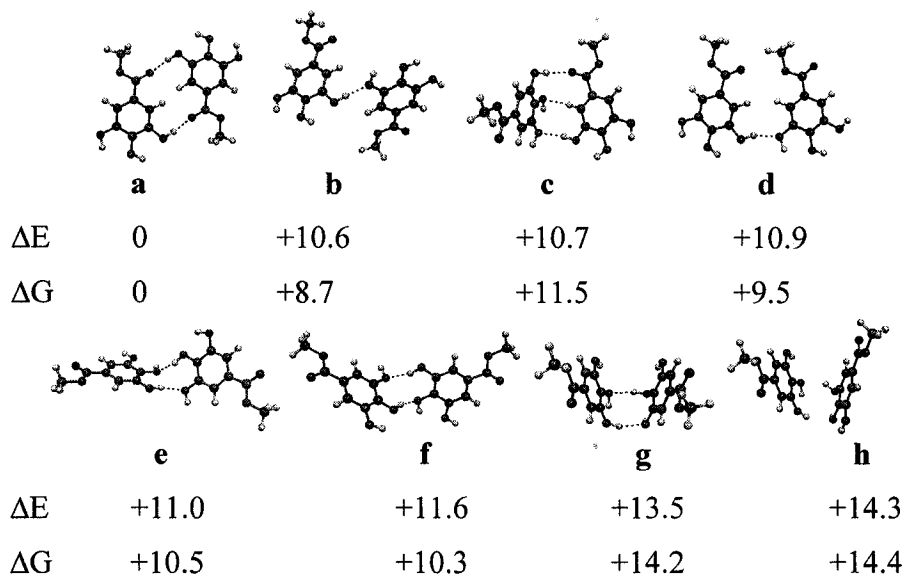


Figure 48. Dimer configurations for 3,4-OH-Me, 3,5-OH-Me and 3,4,5-OH-Me. Relative energies in kcal mol⁻¹ from B3LYP/6-31G(d).

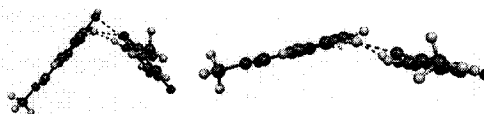


Figure 49. Dimer configurations for 3,4,5-OH-Me(**c**) (left) and 3,5-OH-Me(**b**) (right).

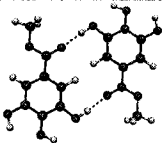
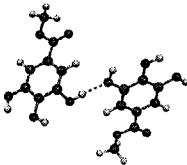
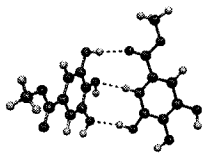
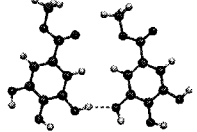
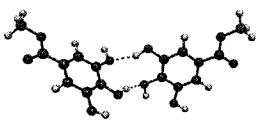
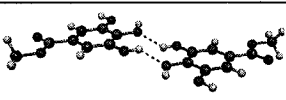

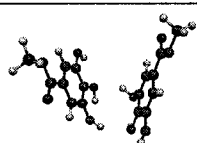
5.3.2.2. Propyl and Hexyl Esters

Dimers of propyl and hexyl esters were constructed from the methyl ester dimers by extending the chains. The aim was to identify whether this would lead to differences in relative energies, especially for those arrangements that could have chain interactions. The full set of structures is given in Appendix D. A summary of relative energies within each of the three series (methyl, propyl and hexyl) for 3,4,5-OH-alkyl is shown in Table 5. It shows that, in general, the configuration of the lowest energy structure does not change with a chain length increase, and no clear energetic effect is observed with a change in chain length.

5.3.3. Trimers

Trimers were constructed by adding one more monomer to the dimers shown in 5.3.2. As was done for the dimers, different plausible orientations were chosen and their geometries fully optimised; the potential energy surfaces have not been explored fully. Frequency calculations were used to confirm minima for methyl and propyl esters. For the hexyl ester trimers, the computational cost was too high to compute frequencies. In the figures, dashed lines correspond to H-bonds as plotted from Molekel.

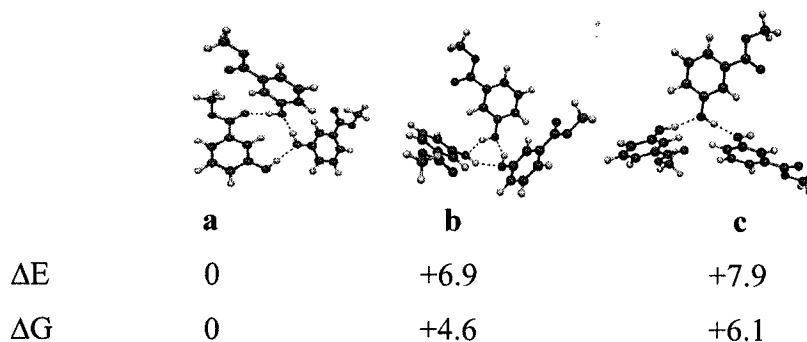
Table 5. Relative energies (kcal mol⁻¹) for chain lengths of increasing size for 3,4,5-OH-alkyl dimers calculated with B3LYP/6-31G(d). (Relative free energies are shown in parentheses.)

	Me	Pr	Hex
	0.0 (0.0)	0.0 (0.0)	0.0 (0.0)
	+10.6 (+8.7)	+10.9 (+8.5)	+10.8 (+8.6)
	+10.7 (+11.5)	10.9 (+12.0)	+10.8 (+10.9)
	+10.9 (+9.5)	+11.1 (+9.9)	+11.0 (+10.1)
	+11.0 (+10.5)	+11.6 (+10.7)	+11.5 (+10.0)
	+11.6 (+10.3)	+11.9 (+10.8)	+11.8 (+10.2)
	+ 13.5 (+14.2)	+13.8 (+14.8)	+13.8 (+15.0)
	+14.3 (+14.4)	+14.6 (+14.9)	+14.5 (+14.6)

5.3.3.1. Methyl Esters

Possible trimer configurations for 3-OH-Me and 4-OH-Me are as shown in Figure 50. Figure 51 shows possible trimer configurations for 3,4-OH-Me and 3,5-OH-Me, and Figure 52 shows possible trimer configurations for 3,4,5-OH-Me.

3-OH-Me



4-OH-Me

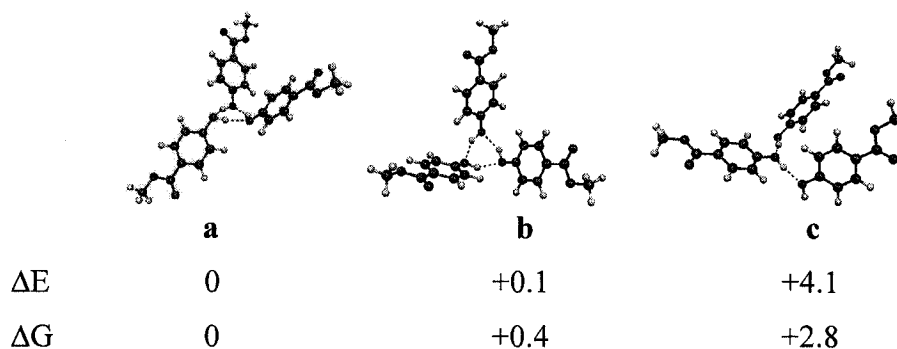


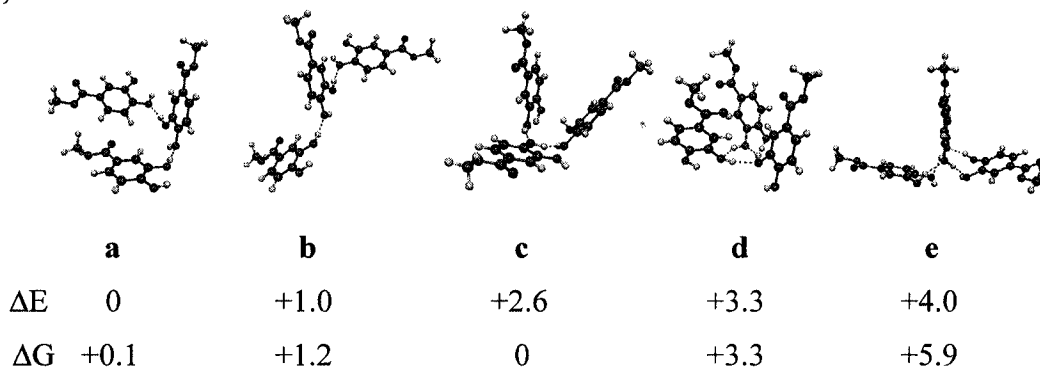
Figure 50. Trimer configurations for 3-OH-Me and 4-OH-Me. Relative energies in kcal mol⁻¹ from B3LYP/6-31G(d).

Figure 50 shows that, as for the dimers, trimers with H-bonding patterns involving a carbonyl group have lower energies. Cyclic arrangements as in 3-OH-Me(**b**) and 4-OH-

Me(a) and (b) are lower in energy than the side-on arrangements even with the corresponding loss in entropy.

As can be seen from Figure 51, 3,4-OH-Me favors the side-on over the cyclic arrangement when the third monomer joins. 3,5-OH-Me and 3,4,5-OH-Me, on the other hand, favor cyclic configurations when the third monomer is involved, because the carbonyl oxygen atom can again be involved in the H-bonding network. But the entropy cost for 3,4,5-OH-Me(a) is significant, as can be seen from the relative free energies (Figure 52).

3,4-OH-Me



3,5-OH-Me

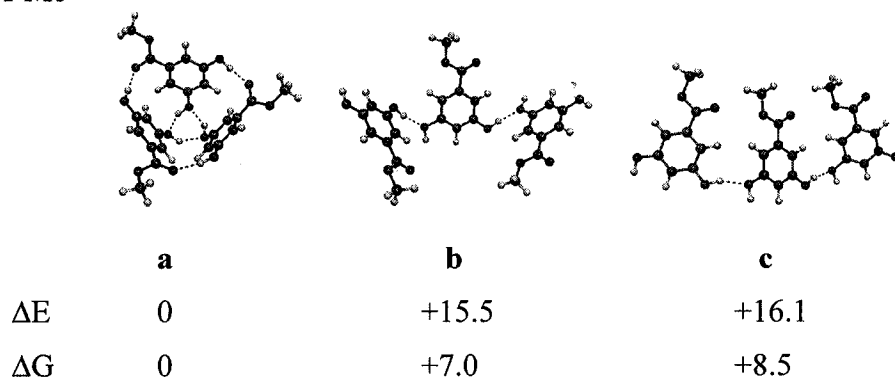


Figure 51. Trimer configurations for 3,4-OH-Me and 3,5-OH-Me. Relative energies in kcal mol⁻¹ from B3LYP/6-31G(d).

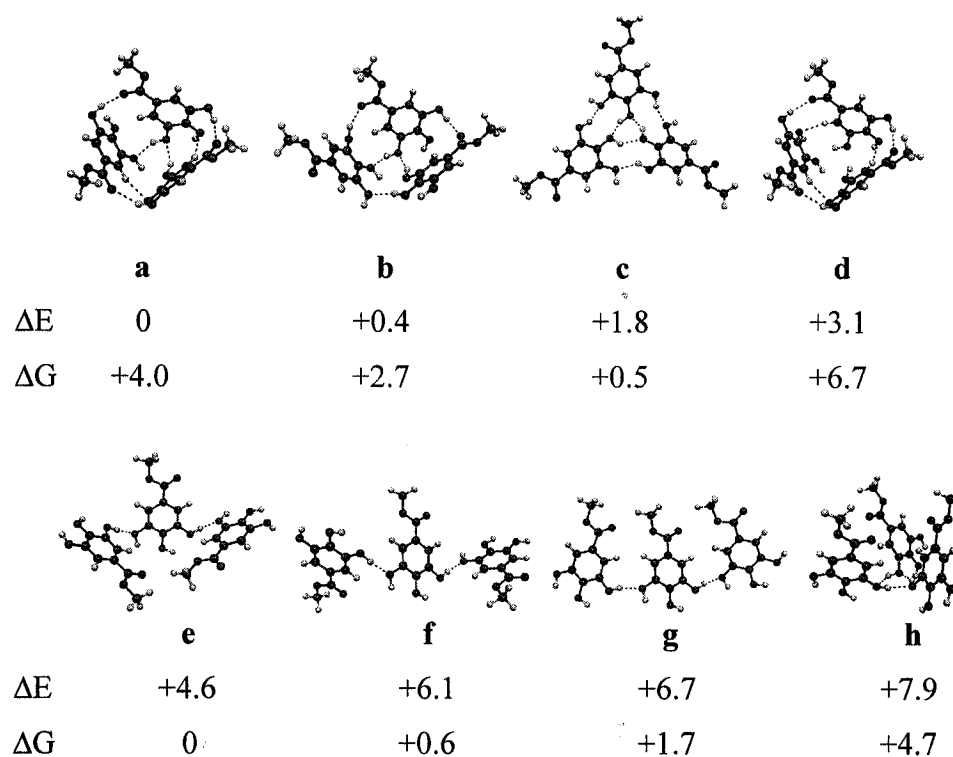


Figure 52. Trimer configurations for 3,4,5-OH-Me. Relative energies in kcal mol⁻¹ from B3LYP/6-31G(d).

5.3.3.2. Propyl and Hexyl Esters

In general and similar to dimers, with extending of the side chains from one to six carbon atoms, neither geometries nor relative energies of the trimer configurations change dramatically. But, interestingly, 3,4-OH-Hex(**c**) shows a significantly lower energy from both 3,4-OH-Hex(**d**) and 3,4-OH-Pr(**d**). This seems to be the consequence of changing one chain conformation from the preferred all-*trans* (see arrow in Figure 53) and thus achieving a better chain packing (Figure 53).

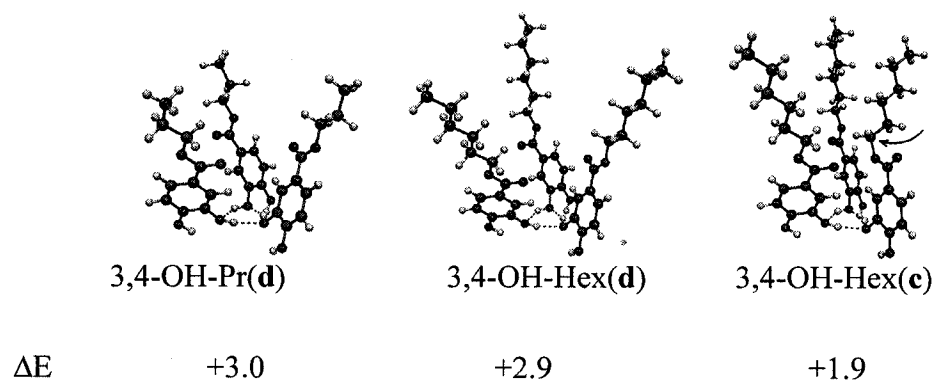


Figure 53. Chain length and conformation effect on the relative energy change of 3,4-OH trimers. Relative energies in kcal mol⁻¹ given with respect to the corresponding global minima.

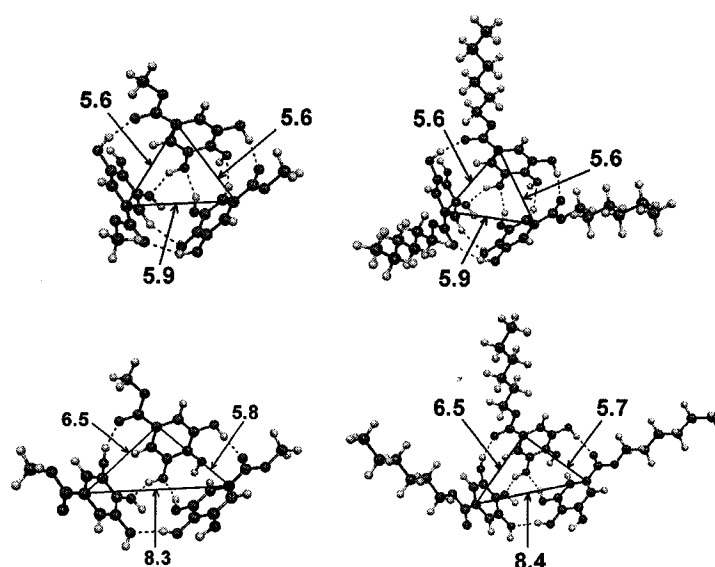


Figure 54. Geometrical change in 3,4,5-OH-alkyl (a and b in Figure 52) with extending of the side chain from one to six carbon atoms. Distances given in Å.

Subtle geometrical changes as shown in Figure 54 take place when the 3,4,5-OH-alkyl side chain is extended from one to six carbon atoms, but taking the ring carbon

atom connected to the C=O group as reference, the total distance of the triangle formed by the three carbon atoms in 3,4,5-OH-Me(**a**) and (**b**) is the same.

One interesting observation for 3,4,5-OH-alkyl is that configuration (**c**) in Figure 52 should not change in relative energy since the three side chains are far apart from each other. If we take 3,4,5-OH-alkyl(**c**) as reference and set its relative energy to zero, then with an increasing chain length, the change in relative energy of configuration (**a**) and configuration (**b**) should be due to side chain interactions. As we can see from Figure 55, both configurations are stabilised significantly as the chains get longer.

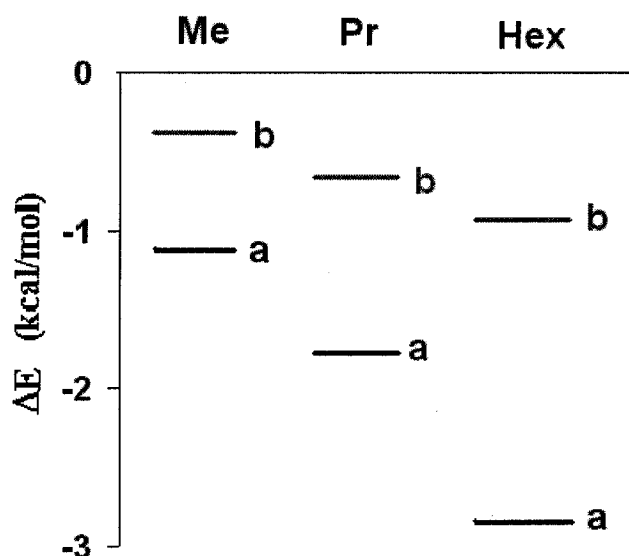


Figure 55. Relative energy changes due to side chain length increase in 3,4,5-OH-alkyl(**a**) and (**b**), when (**c**) is taken as relative zero.

Another interesting observation is that, in Figure 52, configuration (**a**) differs from configuration (**d**) only by rotating the *para*-OH group in one of the three monomers from the most preferred conformation. The total energy of (**a**) is 3.1 kcal mol⁻¹ lower than

that of configuration (d). Figure 56 shows that the configuration changes from the symmetric form of (d) to a form with one side longer than the other two, although the perimeter of the triangle does not change.

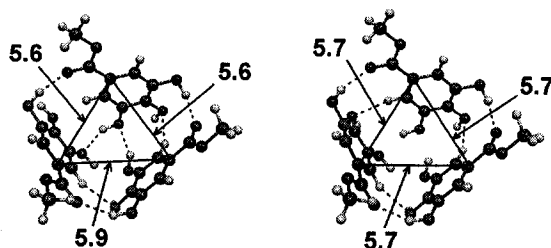


Figure 56. Conformation change of one *para*-OH group in 3,4,5-OH-Me trimers (a) left and (d) right. Distances given in Å.

5.4. Comparison between the Configurations of Dimers and Trimers Obtained from PM3 and B3LYP/6-31G(d)

Unfortunately, DFT methods are computationally rather expensive for the simulation of large systems. The optimisation of a 3,4,5-OH-Hex takes about 2 to 4 weeks. Therefore, it is not practical to simulate dimers, trimers or even higher aggregates of the phenolic lipids with two chains of sixteen carbon atoms each. Semiempirical methods, on the other hand, are less expensive and may still provide reasonable quality. Vysotsky et al. simulated the formation of 2D clusters of fatty alcohols²⁸ and n-carboxylic acids²⁹ using PM3, and the obtained thermodynamic characteristics agreed well with the experimental results.

In order to simulate monolayer fragments of phenolic lipids using semiempirical methods in the future, it is important to test the method first. Calculated geometries and

relative energies obtained from a typical semiempirical method, PM3, are therefore compared with results from B3LYP/6-31G(d) in this section. We have performed the analysis for the methyl ester dimers and trimers of the 3,4,5-OH headgroup. The results are summarised in Tables 6-8.

Table 6. Relative energies (kcal mol⁻¹) for dimers of 3,4,5-OH-Me from B3LYP/6-31G(d) and PM3. Relative free energies are shown in parentheses.

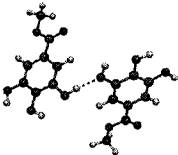
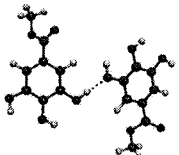
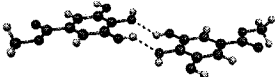

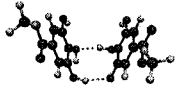
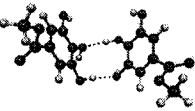
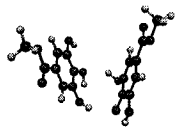
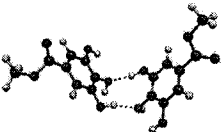
B3LYP/6-31G(d)		PM3	
Geometry	Energy	Geometry	Energy
	0.0 (0.0)		0.0 (0.0)
	+1.0 (+1.6)		+ 2.4 (+ 5.6)
	+ 2.9 (+ 5.5)		+ 2.5 (+ 6.6)
	+ 3.7 (+ 5.7)		+ 3.0 (+ 6.0)

Table 6 shows that the dimer configurations obtained for B3LYP/6-31G(d) and PM3 do not differ significantly, neither does the order in terms of relative energies as expected from our study on the phenol dimer in Section 5.2.1. Table 7, on the other hand,

shows that PM3 can be unreliable in the prediction of relative energies where larger arrangements (here trimers) of the methyl esters are concerned.

Table 7. Relative energies (kcal mol⁻¹) for trimers of 3,4,5-OH-Me from B3LYP/6-31G(d) and PM3. Relative free energies are shown in parentheses.

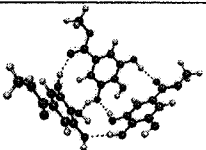
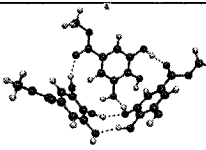
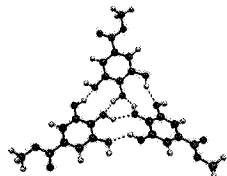
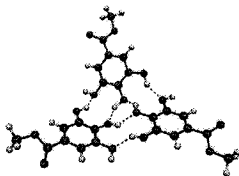
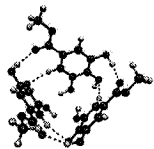
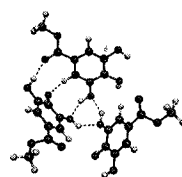
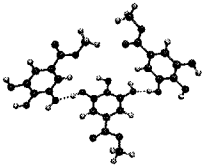
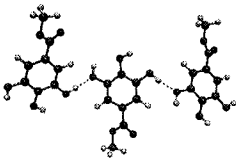
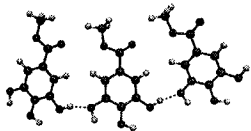
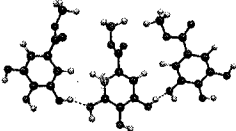
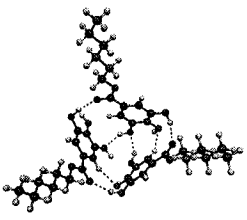
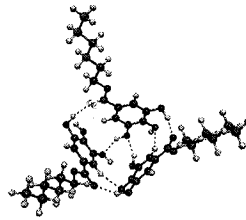
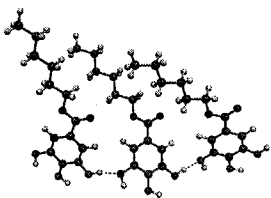
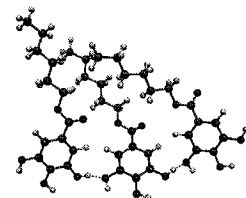
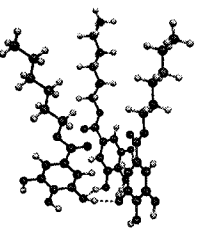
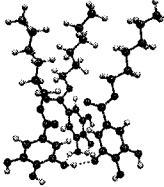
B3LYP/6-31G(d)		PM3	
Geometry	Energy	Geometry	Energy
	0 (+ 2.7)		+ 5.9 (+ 12.5)
	+ 0.8 (+ 2.4)		+ 8.1 (+ 10.5)
	+ 2.6 (+ 6.5)		+ 7.6 (+ 10.5)
	+ 5.7 (0)		+3.1 (+2.2)
	+ 6.3 (+ 1.3)		0.0 (0.0)

Table 8 shows that the calculated configurations of larger systems from B3LYP/6-31G(d) and PM3 differ even less than those of smaller systems. But the relative energies obtained from PM3 are not reliable.

Table 8. Relative energies (kcal mol⁻¹) for trimers of 3,4,5-OH-Hex from B3LYP/6-31G(d) and PM3. Relative free energies are given in parentheses.

B3LYP/6-31G(d)		PM3	
Geometry	Energy	Geometry	Energy
	0.0		+12.1
	+7.4		0.0
	+9.2		+3.3

5.5. Simulation of the Entire DPGG Molecule

5.5.1. Construction of DPGG

The DPGG molecule can be considered as an assembly of two side chains and a headgroup by taking the chiral carbon atom as a reference point. In order to build it, the two side chains and the headgroup are optimised separately. Figure 57 shows parts of

DPGG, where (b) and (c) were already built in Section 5.3.1 and the conformation with the highest population was selected.

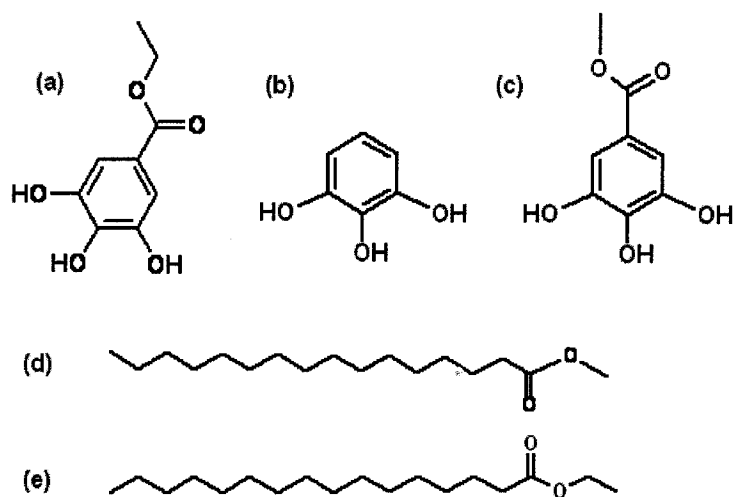


Figure 57. Constituent parts of the DPGG molecule.

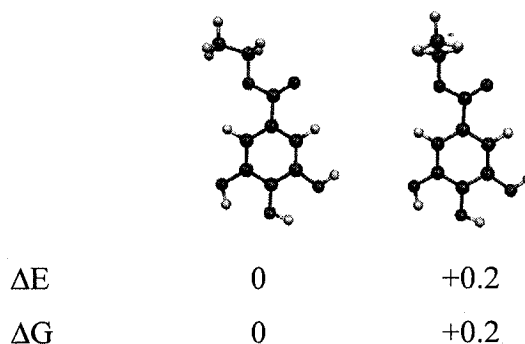


Figure 58. Relative energies (kcal mol^{-1}) for the 180° and 90° conformations of 3,4,5-OH-Et from B3LYP/6-31G(d).

For (a) in Figure 57, the extra methyl group has two possibilities for orientation, shown in Figure 58. With respect to our earlier dimer studies, it is interesting, but not

surprising, to note that the 90° conformation is only 0.2 kcal mol⁻¹ higher in energy than the preferred all-*trans* conformer. This implies that even the head-on dimers, such as 3-OH-Me(a) (Figure 63) would be feasible at the air/water interface.

Obviously, there are many conformations that result from attaching the two side chains (d) and (e) from Figure 57 to the headgroup (a). For our experimental studies, it is of particular interest to determine the preferred relative orientation of the two chains (aligned or not), and so we have performed a relaxed potential energy scan (Figure 59) by twisting the O1-C1-C2-O2 (see Figure 60 for the numbering) dihedral through 360°. The configuration at the global minimum (b) is shown in Figure 60. As can be seen from Figures 59 and 60, the orientation of the two side chains apart from each other ((b) with a O1-C1-C2-O2 dihedral angle of 300°) is preferred over the orientation with the two side chains aligned ((a) with a O1-C1-C2-O2 dihedral angle of 0°). The overall energy barrier to align the side chains is about 5.5 kcal mol⁻¹, and the question is whether this is easily achieved through compression of a monolayer. From the isotherm of DPGG in Figure 9, the energy difference calculated (see Appendix F) between the critical point and the collapse point is only about 0.7 kcal mol⁻¹. As this is an upper estimate, it indicates that, if the DPGG molecules have their two side chains apart from each other upon spreading, the alignment of the two chains will not occur by changing the O1-C1-C2-O2 dihedral angle, rather will by only rotating about one of the C-C bonds.

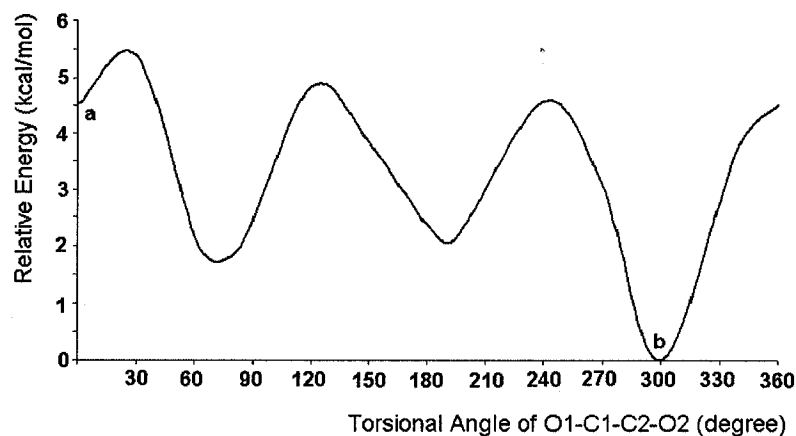


Figure 59. Potential energy profile for a twist of the O1-C1-C2-O2 torsional angle in DPGG from B3LYP/6-31G(d). The letters refer to the structures in Figure 60.

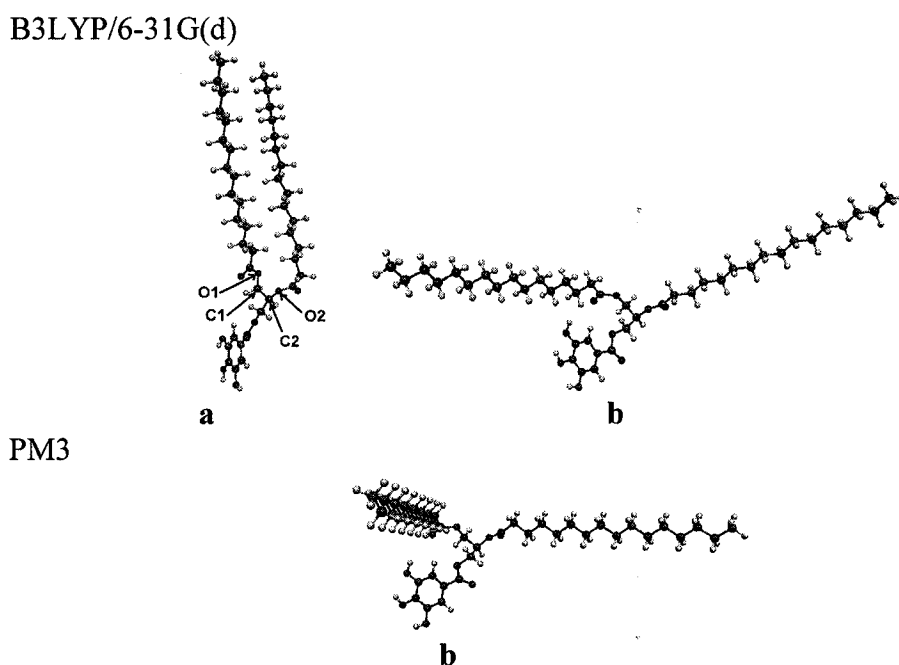


Figure 60. DPGG conformations from B3LYP/6-31G(d) and PM3.

Since DPGG is a large molecule, less expensive methods need to be used to simulate small assemblies of DPGG or even a monolayer formed by DPGG. Therefore,

here, configurations obtained from B3LYP/6-31G(d) and PM3 are compared in order to verify the accuracy of the semiempirical PM3 method. Figure 60 shows the global minimum configuration (**b**) from B3LYP/6-31G(d), and re-optimised from PM3. The two structures are qualitatively comparable.

5.5.2. Verification of Stabilising Interactions

In our study of small assemblies (dimers and trimers), in Section 5.3.2, the structures plotted from Molekel showed “H-bonding interactions” as dotted lines. In order to have more insight into the attractive interactions, AIM theory is used here to identify bonding interactions for a typical 3,4,5-OH-Me dimer configuration. Figure 61 shows the atoms and the critical points in the 3,4,5-OH-Me monomer and the 3,4,5-OH-Me(**b**) dimer. It illustrates a point discussed already in Chapter 5.2.2 for catechol. There seems to be no interaction between O10 and H18 in the monomer in Figure 61, but a small change in geometrical parameters leads to the appearance of both the BCP (CP40) and its associated ring critical point very close by (they are almost superimposed). The dimer actually shows many interactions for the two monomers, and they can be expected to vary widely in strength.

Interactions between the two 3,4,5-OH-Me not only include the O-H...O hydrogen bond identified by Molekel (CP29 in Figure 64), but also C-H...H (“dihydrogen bond”³⁵ (CP15)) and C=O...H (CP23) interactions. Electron density and Laplacian values at the BCPs are shown in Table 9 in order of decreasing interaction.

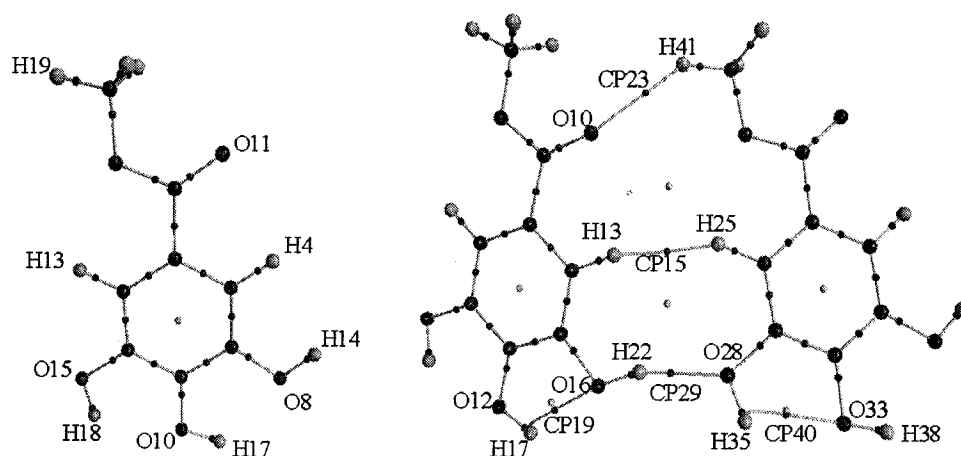


Figure 61. Molecular graphs for the 3,4,5-OH-Me monomer and its dimer 3,4,5-OH-Me(b).

Table 9. Electron density ρ (au) and Laplacian $\nabla^2\rho$ (au) at selected bond critical points for the weak interactions in the 3,4,5-OH-Me dimer. See Figure 64 for numbering.

	ρ	$\nabla^2\rho$
CP29(H22-O28)	0.0291	0.0322
CP19(H17-O16)	0.0186	0.0197
CP40(H35-O33)	0.0171	0.0198
CP23(H41-O10)	0.0079	0.0073
CP15(H13-H25)	0.0053	0.0051

Table 9 shows that the electron density and Laplacian values of CP29 are higher than those of the BCP in the phenol dimer whose ρ is 0.0280 au and $\nabla^2\rho$ is 0.0224 au, which indicates the O-H...O hydrogen bond between two 3,4,5-OH-Me molecules is stronger than that between two phenols due to the contribution of the neighboring

hydroxyl groups. Compared to the BCP in catechol with a ρ of 0.0183 au and $\nabla^2\rho$ of 0.0201 au, CP19 shows almost the same electron density value but a slightly smaller Laplacian while CP40 shows electron density and Laplacian both smaller than those of the BCP in catechol. As expected, the electron density and Laplacian values for CP23 and CP15 are much smaller than those for the BCP of the O-H...O interactions, which indicate that the interactions are much weaker.

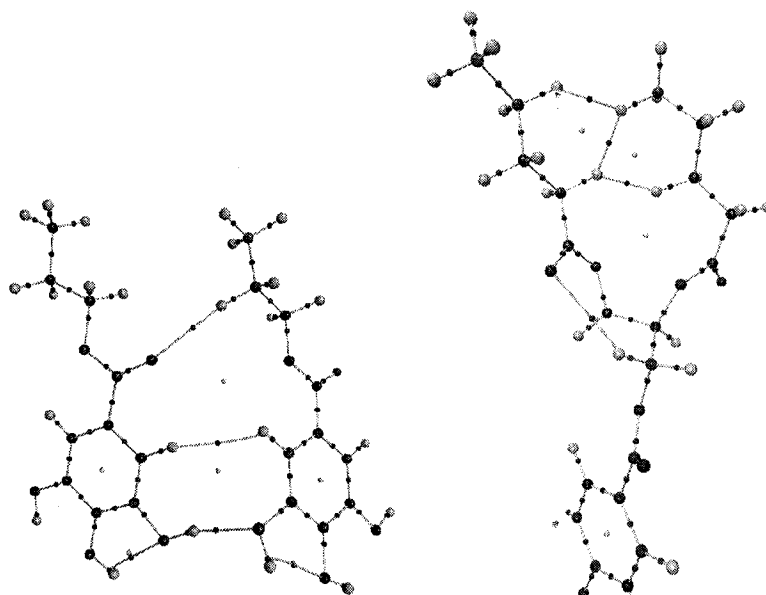


Figure 62. C-H...H and/or C=O...H interactions in a 3,4,5-OH-Pr dimer and a shortened DPGG molecule. (some atoms are hidden.)

C-H...H and C=O...H interactions are further explored for a dimer of 3,4,5-OH-Pr with its longer chains and an abbreviated DPGG molecule (with 4 carbon atoms in each chain) with the two side chains aligned with each other. Results of the interactions are shown in Figure 62. The 3,4,5-OH-Pr dimer shows the same C-H...H and C=O...H interactions, as the 3,4,5-OH-Me dimer; there are no additional C-H...H interactions

between the chains. In contrast, in the shortened DPGG molecule, there are C-H...H interactions between the two side chains, possibly leading to a stabilisation of this configuration. We expect that the full-length DPGG would show many more such interactions between the aligned chains.

5.6. Conclusions

Semiempirical PM3, ab initio HF and MP2 and DFT functional B3LYP (with varied basis sets) were tested to benchmark model chemistries. Comparison between the calculated spectroscopic properties and geometrical information with available experimental data from the literature for phenol, the phenol dimer and the phenol-water complex showed that, in general, PM3 and HF provide larger errors; and MP2 as the computationally most expensive method showed very good performances. B3LYP/6-31G(d) performed well for the systems studies and it was selected as the model chemistry to calculate small assemblies of phenolic esters and entire lipid molecules based on the consideration of both computational cost and quality of the results. A study on the intermolecular H-bond between phenol molecules and the intramolecular H-bond in catechol analysing atomic properties confirmed that B3LYP/6-31G(d) was a good choice.

The configuration of DPGG with the lowest total energy has its two side chains apart from each other rather than aligned. This is probably also true for the other phenolic lipids. The compression process of the monolayer to align the side chains needs to overcome an energy barrier of about $5.5 \text{ kcal mol}^{-1}$, which is higher than the energy of about $0.7 \text{ kcal mol}^{-1}$ used to compress the monolayer from the gas phase to the condensed phase. This indicates the alignment of the side chains only occur by rotating along the C-C bonds.

Based on the model 3,5-OH-alkyl assemblies, the DP-3,5-HBG headgroup shows a different hydrogen bonding pattern compared to that of the other phenolic lipids, which might result in a different monolayer behavior for this molecule. In general, PM3 can provide reasonable quality geometries, but the relative energies calculated at this level are not reliable.

Chapter 6. Conclusions and Future Work

6.1. Conclusions

At room temperature, all the phenolic lipids show direct transition from gaseous phase to condensed phase upon compression. Replacing the H atom in the OH group with the methyl group results in a LE-LC plateau on the isotherm. This maybe resulted by the disruption of the lateral H-bonding. The *para* OH group is critical to the monolayer properties of the phenolic lipids. Removal of the *para* OH group may cause different patterning of the lateral H-bonds and hence the different orientation of the phenolic lipids at the air/water interface.

Isotherms of enantiomerically pure DPGG shifts to larger molecular area upon equilibration. Its BAM images exhibit anisotropic aggregates whose formation is more favored at lower temperatures and longer equilibration periods.

Given enough period of equilibration, the phenolic lipids rearranged, which resulted in significant changes in the shape of the isotherms and some changes in their BAM images. Computational study showed that the phenolic lipids tended to rearrange by releasing their hydrogen bond partners (like molecules) formed in the spreading solution upon spreading at the air/water interface and form H-bonds with subphase water molecules.

Dimer and trimer simulation of the phenolic lipid headgroups show that the aggregation between the phenolic lipid headgroups are energetically favorable.

Moreover, extension of the side chains in the cyclic trimer configuration show that the longer the side chain, the more favorable for DPGG to form aggregates.

The configuration of the phenolic lipids with the lowest total energy has its two side chains apart from each other. Compression process of the monolayer to convert the side chains from the apart configuration to the relatively parallel to each other needs to overcome an energy barrier of about $5.5 \text{ kcal mol}^{-1}$.

6.2. Future Work

This thesis has verified the H-bonding between the phenolic lipids in the spreading solutions and at the air/water interface. But whether the H-bonds are formed between molecules by two OH groups or between an OH group and a C=O group is still not clear. Studying the monolayer properties of molecules without the carboxylic group from the phenolic lipid structure will be helpful in clarifying the above mentioned issue. IR and ^1H NMR studies on the molecules without the carboxylic group and comparing to the results of the phenolic lipids shown in this thesis will also be useful. Meanwhile, studies on the interactions between the phenolic lipids and proteins or metal ions will also be interesting to understand properties of the interactions between the phenolic lipid headgroups in order to use them in the design of biosensors and tether the phenolic lipids onto different substrates to explore the potential uses of the phenolic lipids.

As mentioned in chapter 4, there is a competition of H-bonding between the phenolic lipid molecules with subphase water molecules and with like molecules. The interaction of the phenolic lipids with water molecules can be further studied computationally by including water molecules in the dimer and/or trimer configurations

obtained in this study. Total energies of the systems can be compared with those of the dimers and/or trimers plus separate water molecules in order to justify which case is more favorable. Molecular dynamics studies with water molecules surrounding the dimer and/or trimer configurations are also interesting to verify if there is any change in configuration upon interaction with water molecules. This kind of simulation will also provide information on how much the phenolic lipids are submerged into the water subphase. Moreover, as proposed by Pollastri et al.¹, the interaction between the DPGG headgroups may occur through water bridges, this can be further verified computationally by inserting water molecules between two phenolic lipid molecules and compare total. "Monolayers" of a few of the phenolic lipid molecules can be constructed by PM3 to characterise the H-bonding network. Simulations with molecular mechanics for dimer and/or trimer configurations with full side chains and different number and position of OH groups on the aromatic headgroup may give us more ideas of the influence of the headgroup on the monolayer behavior of the phenolic lipids.

References

1. Pollastri, M. P.; Porter, N. A.; McIntosh, T. J.; Simon, S. A. *Chemistry and Physics of Lipids* **2000**, 104, (1), 67-74.
2. Myers, D., *Surfactant Science and Technology*. Third ed.; J. Wiley: Hoboken, N.J., 2006.
3. Schmidt, R.; DeWolf, C. E. *Langmuir* **2004**, 20, (8), 3284-3288.
4. Tueckmantel, W.; Kozikowski, A. P.; Romanczyk, L. J., Jr. *Journal of the American Chemical Society* **1999**, 121, (51), 12073-12081.
5. Ho, C. T.; Lee, C. Y.; Huang, M. T.; Editors, *Phenolic Compounds in Food and Their Effects on Health. I: Analysis, Occurrence, and Chemistry. (Developed from a Symposium Sponsored by the Division of Agricultural and Food Chemistry of the American Chemical Society at the Fourth Chemical Congress of North America (202nd National Meeting of the American Chemical Society), New York, New York, August 25-30, 1991)*. [In: *ACS Symp. Ser.*, 1992; 506]. 1992; p 338 pp.
6. Handique, J. G.; Baruah, J. B. *Reactive & Functional Polymers* **2002**, 52, (3), 163-188.
7. Shaw, D. J., *Introduction to Colloid and Surface Chemistry*. Fourth ed.; Butterworths: London; Boston, 1992.
8. Kolasinski, K. W., *Surface Science Foundations of Catalysis and Nanoscience*. Wiley: Chichester; New York, 2002.
9. Adamson, A. W.; Gast, A. P., *Physical Chemistry of Surfaces*. Sixth ed.; Wiley: New York, 1997; p 131-136.
10. Desiraju, G. R.; Steiner, T., *The Weak Hydrogen Bond in Structural Chemistry and Biology*. Oxford University Press Inc.: New York, 1999; p 507.
11. Jeffrey, G. A., *An Introduction to Hydrogen Bonding*. Oxford University Press Inc.: New York, 1997; p 303.
12. Hadži, D., *Theoretical Treatments of Hydrogen Bonding*. John Wiley & Son: Chichester; New York; Weinheim; Brisbane; Singapore; Toronto, 1997.
13. Thirumoorthy, K.; Nandi, N.; Vollhardt, D. *Journal of Physical Chemistry B* **2005**, 109, (21), 10820-10829.
14. Wang, L.; Jacobi, S.; Sun, J.; Overs, M.; Fuchs, H.; Schaefer, H. J.; Zhang, X.; Shen, J.; Chi, L. *Journal of Colloid and Interface Science* **2005**, 285, (2), 814-820.
15. Chen, X.; Wiehle, S.; Chi, L.; Mück-Lichtenfeld, C.; Rudert, R.; Vollhardt, D.; Fuchs, H.; Haufe, G. *Langmuir* **2005**, 21, (8), 3376-3383.
16. Dreger, K.; Zhang, L.; Galla, H.-J.; Fuchs, H.; Chi, L.; Wuerthwein, E.-U.; Schaefer, H. J. *Langmuir* **2006**, 22, (4), 1586-1594.
17. Beagley, B.; Chantrell, S. J.; Kirby, R. G.; Schmidling, D. G. *Journal of Molecular Structure* **1975**, 25, (2), 319-27.
18. Butler, R. N.; Duffy, J. P.; McArdle, P.; Cunningham, D.; O'Halloran, G. A. *Journal of the Chemical Society, Chemical Communications* **1989**, (17), 1210-11.
19. Yavari, I.; Staral, J. S.; Roberts, J. D. *Organic Magnetic Resonance* **1979**, 12, (6), 340-2.

20. Meij, R.; Oskam, A.; Stufkens, D. J. *Journal of Molecular Structure* **1979**, 51, (1), 37-49.
21. Romano, R. M.; Della Vedova, C. O.; Boesec, R. *Journal of Molecular Structure* **1999**, 475, (1), 1-4.
22. Muchall, H. M. *Journal of Physical Chemistry A* **2001**, 105, (3), 632-636.
23. Duchs, D.; Schmid, F. *Journal of Physics: Condensed Matter* **2001**, 13, (21), 4853-4862.
24. Kaznessis, Y. N.; Kim, S.; Larson, R. G. *Biophysical Journal* **2002**, 82, (4), 1731-1742.
25. Alper, H. E.; Bassolino, D.; Stouch, T. R. *Journal of Chemical Physics* **1993**, 98, (12), 9798-807.
26. Alper, H. E.; Bassolino-Klimas, D.; Stouch, T. R. *Journal of Chemical Physics* **1993**, 99, (7), 5547-59.
27. Foresman, J. B., *Exporing Chemistry with Electronic Structure Methods*. 2nd ed.; Pittsburgh, 1996; p 302.
28. Vysotsky, Y. B.; Bryantsev, V. S.; Fainerman, V. B.; Vollhardt, D.; Miller, R. *Journal of Physical Chemistry B* **2002**, 106, (1), 121-131.
29. Vysotsky, Y. B.; Muratov, D. V.; Boldyreva, F. L.; Fainerman, V. B.; Vollhardt, D.; Miller, R. *Journal of Physical Chemistry B* **2006**, 110, (10), 4717-4730.
30. Bader, R. F. W., *Atoms in Molecules: a quantum theory*. Oxford ; Clarendon Press: New York, 1990.
31. Pacios, L. F.; Gomez, P. C. *Journal of Computational Chemistry* **2001**, 22, (7), 702-716.
32. Koch, U.; Popelier, P. L. A. *Journal of Physical Chemistry* **1995**, 99, (24), 9747-54.
33. Popelier, P. L. A.; Logothetis, G. *Journal of Organometallic Chemistry* **1998**, 555, (1), 101-111.
34. Popelier, P. L. A.; Bader, R. F. W. *Journal of Physical Chemistry* **1994**, 98, (16), 4473-81.
35. Popelier, P. L. A. *Journal of Physical Chemistry A* **1998**, 102, (10), 1873-1878.
36. Spackman, M. A. *Chemical Physics Letters* **1999**, 301, (5,6), 425-429.
37. Espinosa, E.; Molins, E.; Lecomte, C. *Chemical Physics Letters* **1998**, 285, (3,4), 170-173.
38. Cubero, E.; Orozco, M.; Hobza, P.; Luque, F. J. *Journal of Physical Chemistry A* **1999**, 103, (32), 6394-6401.
39. Popelier, P., *Atoms in Molecules An Introduction*. 2nd ed.; Printice Hall: New Jersey, 2000.
40. <http://www.ksvlt.com/content/index/BAM300>; Last accessed on March 01, 2008.
41. Kaercher, T.; Honig, D.; Mobius, D. *International Ophthalmology* **1993**, 17, (6), 341-8.
42. Schmidt, R.; Carrigan, J. G.; DeWolf, C. E. *Canadian Journal of Chemistry* **2006**, 84, (10), 1411-1415.
43. Gaussian 98; Revision A.11.4; Frisch, M. J.; Trucks, G. W.; Schlegel, H. B.; Scuseria, G. E.; Robb, M. A.; Cheeseman, J. R.; Zakrzewski, V. G.; Montgomery, J., J. A.; Stratmann, R. E.; Burant, J. C.; Dapprich, S.; Millam, J. M.; Daniels, A.

- D.; Kudin, K. N.; Strain, M. C.; Farkas, O.; Tomasi, J.; Barone, V.; Cossi, M.; Cammi, R.; Mennucci, B.; Pomelli, C.; Adamo, C.; Clifford, S.; Ochterski, J.; Petersson, G. A.; Ayala, P. Y.; Cui, Q.; Morokuma, K.; Rega, N.; Salvador, P.; Dannenberg, J. J.; Malick, D. K.; Rabuck, A. D.; Raghavachari, K.; Foresman, J. B.; Cioslowski, J.; Ortiz, J. V.; Baboul, A. G.; Stefanov, B. B.; Liu, G.; Liashenko, A.; Piskorz, P.; Komaromi, I.; Gomperts, R.; Martin, R. L.; Fox, D. J.; Keith, T.; Al-Laham, M. A.; Peng, C. Y.; Nanayakkara, A.; Challacombe, M.; Gill, P. M. W.; Johnson, B.; Chen, W.; Wong, M. W.; Andres, J. L.; Gonzalez, C.; Head-Gordon, M.; Replogle, E. S.; and Pople, J. A.; Gaussian, I., Pittsburgh PA, 2002., In.
44. Gaussian 03; Revision C.02; Frisch, M. J.; Trucks, G. W.; Schlegel, H. B.; Scuseria, G. E.; Robb, M. A.; Cheeseman, J. R.; Montgomery, J., J. A.; ; Vreven, T.; Kudin, K. N.; Burant, J. C.; Millam, J. M.; Iyengar, S. S.; Tomasi, J.; Barone, V.; Mennucci, B.; Cossi, M.; Scalmani, G.; Rega, N.; Petersson, G. A.; Nakatsuji, H.; Hada, M.; Ehara, M.; Toyota, K.; Fukuda, R.; Hasegawa, J.; Ishida, M.; Nakajima, T.; Honda, Y.; Kitao, O.; Nakai, H.; Klene, M.; Li, X.; Knox, J. E.; Hratchian, H. P.; Cross, J. B.; Bakken, V.; Adamo, C.; Jaramillo, J.; Gomperts, R.; Stratmann, R. E.; Yazyev, O.; Austin, A. J.; Cammi, R.; Pomelli, C.; Ochterski, J. W.; Ayala, P. Y.; Morokuma, K.; Voth, G. A.; Salvador, P.; Dannenberg, J. J.; Zakrzewski, V. G.; Dapprich, S.; Daniels, A. D.; Strain, M. C.; Farkas, O.; Malick, D. K.; Rabuck, A. D.; Raghavachari, K.; Foresman, J. B.; Ortiz, J. V.; Cui, Q.; Baboul, A. G.; Clifford, S.; Cioslowski, J.; Stefanov, B. B.; Liu, G.; Liashenko, A.; Piskorz, P.; Komaromi, I.; Martin, R. L.; Fox, D. J.; Keith, T.; Al-Laham, M. A.; Peng, C. Y.; Nanayakkara, A.; Challacombe, M.; Gill, P. M. W.; Johnson, B.; Chen, W.; Wong, M. W.; Gonzalez, C.; and Pople, J. A. G., Inc., Wallingford CT, 2004., In.
 45. Stewart, J. J. P. *Journal of Computational Chemistry* **1989**, 10, (2), 209-20.
 46. Hehre, W. J.; Radom, L.; Schleyer, P. v. R.; Pople, J. A., *Ab initio molecular orbital theory*. John Wiley & Sons: New York, 1986.
 47. Lee, C.; Yang, W.; Parr, R. G. *Physical Review B: Condensed Matter and Materials Physics* **1988**, 37, (2), 785-9.
 48. Stephens, P. J.; Devlin, F. J.; Chabalowski, C. F.; Frisch, M. J. *Journal of Physical Chemistry* **1994**, 98, (45), 11623-7.
 49. Ernzerhof, M.; Burke, K.; Perdew, J. P. *Journal of Chemical Physics* **1996**, 105, (7), 2798-2803.
 50. Perdew, J. P.; Burke, K.; Ernzerhof, M. *Physical Review Letters* **1997**, 78, (7), 1396.
 51. www.chemistry.mcmaster.ca/aimpac; March 12, 2008.
 52. Biegler-Konig, F. *Journal of Computational Chemistry* **2000**, 21, (12), 1040-1048.
 53. <http://www.aim2000.de/>; Last accessed on March 03, 2008.
 54. <http://www.cscs.ch/molekel/manual/help.html>. Last accessed on March 12, 2008.
 55. Mouri, E.; Furuya, Y.; Matsumoto, K.; Matsuoka, H. *Langmuir* **2004**, 20, (19), 8062-7.
 56. Vollhardt, D. *Advances in Colloid and Interface Science* **1996**, 64, 143-71.

57. Zhao, L.; Feng, S.-S. *Journal of Colloid and Interface Science* **2004**, 274, (1), 55-68.
58. Yun, H.; Choi, Y.-W.; Kim, N. J.; Sohn, D. *Bulletin of the Korean Chemical Society* **2003**, 24, (3), 377-383.
59. Menger, F. M.; Wood, M. G., Jr.; Richardson, S.; Zhou, Q.; Elrington, A. R.; Sherrod, M. J. *Journal of the American Chemical Society* **1988**, 110, (20), 6797-803.
60. Siegel, S.; Vollhardt, D.; Brezesinski, G.; Bringezu, F.; Möhwald, H. *Materials Science & Engineering, C: Biomimetic and Supramolecular Systems* **1999**, C8-C9, 3-11.
61. Vollhardt, D.; Emrich, G.; Siegel, S.; Rudert, R. *Langmuir* **2002**, 18, (17), 6571-6577.
62. Tsukanova, V.; Grainger, D. W.; Salesse, C. *Langmuir* **2002**, 18, (14), 5539-5550.
63. Weidemann, G.; Vollhardt, D. *Biophysical Journal* **1996**, 70, (6), 2758-2766.
64. Jacobi, S.; Chi, L. F.; Plate, M.; Overs, M.; Schafer, H. J.; Fuchs, H. *Thin Solid Films* **1998**, 327-329, 180-184.
65. Dyck, M.; Krueger, P.; Loesche, M. *Physical Chemistry Chemical Physics* **2005**, 7, (1), 150-156.
66. Islam, M. N.; Kato, T. *Journal of Chemical Physics* **2004**, 121, (20), 10217-10222.
67. Vollhardt, D.; Wagner, R. *Journal of Physical Chemistry B* **2006**, 110, (30), 14881-14889.
68. Nandi, N.; Vollhardt, D. *Chemical reviews* **2003**, 103, (10), 4033-76.
69. Fairbairn, J. Effect of Subphase pH on Monolayers of Racemic and Enantiomerically Pure 1,2-Dipalmitoylglycerol Honors thesis Concordia University, 2006.
70. Pavia, D. L.; Lampman, G. M.; Kriz, G. S., *Introduction to spectroscopy: a guide for students of organic chemistry*. 3rd ed.; Fort Worth: Harcourt College Publishers: 2001.
71. Schwarz, G.; Zhang, J. *Chemistry and Physics of Lipids* **2001**, 110, (1), 35-45.
72. Studniarz, S. A. *Abstracts of Papers, 230th ACS National Meeting, Washington, DC, United States, Aug. 28-Sept. 1, 2005* **2005**, ORGN-568.
73. Wang, X. J.; Wiehler, H.; Ching, C. B. *Journal of Chemical and Engineering Data* **2003**, 48, (5), 1092-1098.
74. Ushio, T.; Endo, K.; Yamamoto, K. *Journal of the Pharmaceutical Society of Japan* **1996**, 116, (11), 866-75.
75. Connell, L. L.; Ohline, S. M.; Joireman, P. W.; Corcoran, T. C.; Felker, P. M. *Journal of Chemical Physics* **1992**, 96, (4), 2585-93.
76. Gerhards, M.; Schmitt, M.; Kleinermanns, K.; Stahl, W. *Journal of Chemical Physics* **1996**, 104, (3), 967-71.
77. Ebata, T.; Watanabe, T.; Mikami, N. *Journal of Physical Chemistry* **1995**, 99, (16), 5761-4.
78. Onda, M.; Hasunuma, K.; Hashimoto, T.; Yamaguchi, I. *Journal of Molecular Structure* **1987**, 159, (3-4), 243-8.
79. Caminati, W.; Di Bernardo, S.; Schafer, L.; Kulp-Newton, S. Q.; Siam, K. *Journal of Molecular Structure* **1990**, 240, 263-74.

80. Foti, M. C.; Barclay, L. R. C.; Ingold, K. U. *Journal of the American Chemical Society* **2002**, 124, (43), 12881-12888.
81. Foti, M. C.; DiLabio, G. A.; Ingold, K. U. *Journal of the American Chemical Society* **2003**, 125, (47), 14642-14647.
82. Ranganathan, A.; Kulkarni, G. U.; Rao, C. N. R. *Journal of Physical Chemistry A* **2003**, 107, (31), 6073-6081.
83. Eliel, E. L.; Wilen, S. H.; Mander, L. N., *Stereochemistry of organic compounds*. Wiley & Sons: New York, 1994.
84. Wunderlich, H.; Mootz, D. *Acta Crystallographica, Section B: Structural Crystallography and Crystal Chemistry* **1971**, 27, (8), 1684-6.
85. Sekine, A.; Mitsumori, T.; Uekusa, H.; Ohashi, Y.; Yagi, M. *X-Ray Structure Analysis Online* **2003**, 19, (Oct.-Dec.), 47-48.
86. Larsen, N. W. *Journal of Molecular Structure* **1979**, 51, (2), 175-90.
87. Portalone, G.; Schultz, G.; Domenicano, A.; Hargittai, I. *Chemical Physics Letters* **1992**, 197, (4-5), 482-8.
88. Hobza, P.; Riehn, C.; Weichert, A.; Brutschy, B. *Chemical Physics* **2002**, 283, (1-2), 331-339.
89. Weichert, A.; Riehn, C.; Brutschy, B. *Journal of Physical Chemistry A* **2001**, 105, (23), 5679-5691.
90. Berden, G.; Meerts, W. L.; Schmitt, M.; Kleinermanns, K. *Journal of Chemical Physics* **1996**, 104, (3), 972-82.

Appendix A. BAM Images (Refer to the Attached CD)

Appendix B. Tables for Model Chemistry Selection

Table B1. Experimental and Calculated Bond Distances (Å) and Angles (degrees) for Phenol

	C-H _{mean}	C-C _{mean}	C-O	O-H	C-C-O ^a	C-O-H
Experimental ^b	1.083±0.004	1.393±0.005	1.375±0.005	0.957±0.006	122.1±0.3	108.8±0.4
Experimental ^c		1.399±0.003	1.381±0.004	0.958±0.003	121.2±1.2	106.4±3.7
PM3	1.095	1.394	1.369	0.948	121.2	106.4
HF/6-31G(d)	1.075	1.386	1.353	0.947	122.5	110.7
MP2/6-31G(d)	1.088	1.396	1.375	0.974	122.8	108.3
B3LYP/						
6-31G(d)	1.087	1.397	1.369	0.969	122.6	108.9
6-31G(d,p)	1.086	1.396	1.368	0.966	122.6	109.0
6-311G(d,p)	1.084	1.394	1.366	0.963	122.7	109.0
6-31+G(d,p)	1.087	1.398	1.372	0.966	122.5	110.0
6-311+G(d,p)	1.084	1.394	1.370	0.962	122.5	109.8
6-311++G(d,p)	1.084	1.394	1.370	0.962	122.5	109.7
6-311+G(2d,p)	1.083	1.392	1.369	0.964	122.6	109.6
cc-pVDZ	1.093	1.399	1.367	0.969	122.7	108.6
PBE0/	1.086	1.393	1.360	0.967	122.6	108.7
6-31G(d)						

a. For the C-C bond *syn* to the O-H bond.

b. Microwave data from ref. 86

c. Electron diffraction data from ref. 87.

Table B2. Experimental and Calculated Rotational Constants (MHz) A, B and C for Phenol

	A	B	C
Experimental ^a	5650.5±1.1	2619.2±0.5	1789.9±0.3
PM3	5606.2	2640.1	1794.9
HF/6-31G(d)	5606.2	2640.2	1794.9
MP2/6-31G(d)	5641.5	2611.7	1785.2
B3LYP/6-31G(d)	5646.7	2612.7	1786.2
B3LYP/6-31G(d,p)	5649.9	2614.1	1787.2
B3LYP/6-311G(d,p)	5672.8	2619.9	1792.2
B3LYP/6-31+G(d,p)	5637.8	2607.1	1782.7
B3LYP/6-311+G(d,p)	5667.0	2617.9	1790.7
B3LYP/6-311++G(d,p)	5667.2	2618.0	1790.8
B3LYP/6-311+G(2d,p)	5688.8	2625.6	1796.5
B3LYP/cc-pVDZ	5631.2	2605.9	1781.5
PBE0/6-31G(d)	5677.5	2631.4	1798.1

a. Microwave data from ref. 86.

Table B3. Experimental and Calculated Distances (Å), Angles and Dihedral Angles (degrees) for the Phenol Dimer

	O1-O2	C8-H2	H8-H2	C1-O1-O2	O1-O2-C7	O1-O2-H7	C2-C1-O1-O2	C1-O1-O2-C7	O1-O2-C7-C8	C1-O1-O2-H7
Experimental ^a	3.00 ±0.2	2.92	2.75	108.8 ±10	117.8	131.6	0.0 ±20	-59.2	-13.7	100.7
PM3	2.74	2.76	1.71	122.6	125.9	108.1	11.2	-68.2	-48.8	162.1
HF/ 6-31G(d)	2.96	4.11	3.72	114.9	120.0	128.0	-1.7	-107.9	-5.3	83.6
MP2/ 6-31G(d)	2.88	3.23	3.11	108.9	111.7	137.2	-7.8	-69.6	-12.3	93.1
B3LYP/ 6-31G(d)	2.87	4.10	3.73	113.2	115.7	133.6	-4.5	-110.6	-4.9	80.6
6-31G(d,p)	2.86	4.09	3.73	113.1	115.4	133.8	-4.6	-110.5	4.5	80.1
6-311G(d,p)	2.86	4.12	3.75	113.4	117.4	131.2	-2.4	-113.0	6.5	81.1
6-31+G(d,p)	2.88	3.85	3.27	114.4	126.8	115.5	1.3	-105.7	-29.4	107.4
6-311+G(d,p)	2.89	3.94	3.48	113.9	128.4	117.9	4.6	-107.7	-17.7	95.5
6-311++G(d,p)	2.89	4.41	4.06	113.8	128.5	118.8	2.3	-124.6	14.0	75.6
6-311+G(2d,p)	2.90	4.01	3.48	114.2	128.2	114.5	4.0	-113.7	-28.6	99.5
cc-pVDZ	2.84	4.10	3.77	112.6	115.7	134.1	-4.0	-111.9	-3.5	76.4
PBE0/6-31G(d)	2.85	3.99	3.63	112.7	115.8	133.6	-3.8	-108.1	5.1	83.0

a. High-resolution rotational coherence spectroscopy from refs. 88 and 89.

Table B4. Experimental and Calculated Rotational Constants (MHz) for the Phenol Dimer

	A	B	C	B+C	2A-B-C	B-C
Experimental ^a	1418.6±5.7	313.5±14.0	285.5±14.0	599.0±3.0	2238.0±11.2	28.0±14.0
Experimental ^b	1414.4±0.6	313.7±0.8	287.5±0.7	610.2±0.6		26.2 ±1.0
PM3	1720.2	275.5	244.5	520.0	2920.4	31.0
HF/6-31G(d,p)	1846.5	240.8	237.0	477.8	3215.2	3.8
MP2/6-31G(d)	1366.0	325.6	305.5	631.1	2100.9	20.1
B3LYP/						
6-31G(d)	1777.4	251.6	245.1	496.7	3058.1	6.5
6-31G(d,p)	1782.8	251.9	245.2	497.1	3068.5	6.7
6-311G(d,p)	1842.5	246.5	240.1	486.6	3198.4	6.4
6-31+G(d,p)	1902.6	235.4	230.2	465.6	3339.6	5.2
6-311+G(d,p)	1926.5	231.7	229.9	461.6	3391.4	1.8
6-311++G(d,p)	1932.9	231.1	229.4	460.5	3405.3	1.7
6-311+G(2d,p)	2031.2	224.5	223.9	448.4	3614.0	0.6
cc-pVDZ	1789.3	251.7	244.3	496.0	3082.6	7.4
PBE0/6-31G(d)	1773.6	255.6	250.4	506.0	3041.2	5.2

a. High-resolution rotational coherence spectroscopy from ref. 75.

b. Time-resolved fluorescence depletion high-resolution rotational coherence spectroscopy data from refs. 88 and 89.

Table B5. Selected Experimental And Calculated Bond Distances (Å), Angles (degrees) and Rotational Constants (MHz) A, B and C for the Phenol-Water Complex (Relative differences in Figure 36 for all the properties are calculated using the microwave data).

	Φ^a	R(O-O) ^a	β^a	γ^a	A ^b	B ^b	C ^b
Experimental ^b	6.7	2.93±0.2	144.5	115.5	4291.49	1092.14	873.73
Experimental ^a	5.0	2.88	139.0	113.7	4291.50	1092	873.97
PM3	6.8	2.75	123.2	115.2	4417.58	1117.57	895.05
HF/ 6-31G(d,p)	4.0	2.90	127.3	115.4	4318.44	1112.01	890.66
MP2/ 6-31G(d)	3.1	2.85	117.8	111.9	4257.16	1113.38	886.26
B3LYP/ 6-31G(d)	4.6	2.81	112.4	114.4	4343.39	1103.08	883.33
6-31G(d,p)	3.5	2.81	115.2	113.4	4316.75	1111.75	887.74
6-311G(d,p)	4.6	2.81	112.4	114.4	4290.34	1126.54	896.01
6-31+G(d,p)	3.7	2.84	129.4	114.6	4319.70	1089.19	873.48
6-311+G(d,p)	3.2	2.85	134.3	113.9	4307.20	1096.89	877.87
6-311++G(d,p)	4.0	2.86	126.7	114.1	4314.21	1095.11	877.02
6-311+G(2d,p)	3.4	2.85	134.3	114.6	4342.87	1090.74	875.39
cc-pVDZ	1.1	2.79	122.4	110.4	4223.88	1141.60	902.50
PBE0/6-31G(d)	3.9	2.18	114.4	113.5	4349.53	1123.25	896.46

a. Geometrical parameters from microwave spectroscopy from ref. 76, see Figure 35 for symbols.

b. Rotational constants from high resolution UV spectroscopy from ref. 90.

Table B6. Population N (au), Energy E (au), radii of hydrogen and oxygen atoms r_H and r_O (Å), dipolar polarization μ (au) and volume V (Å³) for H12 in the phenol monomer and its dimer

		N	E	$r_H^{a,b}$	$r_O^{a,b}$	μ	V ^c
B3LYP/ 6-31G(d)	Monomer	0.440	-0.3723	2.20	3.30	0.170	17.10
	Dimer	0.402	-0.3511	1.30	2.29	0.138	13.37
6-31G(d,p)	Monomer	0.418	-0.3679	2.25	3.39	0.165	16.61
	Dimer	0.377	-0.3441	1.26	2.33	0.130	12.49
6-311G(d,p)	Monomer	0.443	-0.3918	2.27	3.41	0.164	17.53
	Dimer	0.398	-0.3658	1.25	2.34	0.127	13.05
6-31+G(d,p)	Monomer	0.411	-0.3618	2.24	3.37	0.167	16.63
	Dimer	0.375	-0.3421	1.27	2.34	0.129	13.01
6-311+G(d,p)	Monomer	0.438	-0.3870	2.28	3.43	0.167	17.67
	Dimer	0.396	-0.3631	1.27	2.36	0.128	13.63
6-311++G(d,p)	Monomer	0.438	-0.3869	2.28	3.43	0.167	17.65
	Dimer	0.396	-0.3630	1.27	2.36	0.128	13.62
6-311+G(2d,p)	Monomer	0.445	-0.3923	2.28	3.40	0.164	17.60
	Dimer	0.402	-0.3511	1.30	2.28	0.138	13.37
cc-pVDZ	Monomer	0.399	-0.3372	2.30	3.39	0.169	16.40
	Dimer	0.362	-0.3161	1.24	2.31	0.132	12.09
PBE0/6-31G(d)	Monomer	0.427	-0.3665	2.22	3.29	0.164	16.34
	Dimer	0.391	-0.3447	1.28	2.28	0.135	12.70
MP2/6-31G(d)	Monomer	0.426	-0.3579	2.21	3.35	0.166	16.58
	Dimer	0.386	-0.3368	1.30	2.32	0.134	12.67

a. Radius was determined in the direction of the O-H...O bond path.

b. The monomer (dimer) radius is the non-bonded (bonded) radius; the penetration derived from these is shown in Figure 39 as the monomer-dimer difference.

c. Volume has been taken to the 0.001 au contour.

Table B7. Population N (au), Energy E (au), radii of hydrogen and oxygen atoms r_H and r_O (Å), dipolar polarization μ (au) and volume V (Å³) for H12 in catechol

		N	E	$r_H^{a,b}$	$r_O^{a,b}$	μ	V ^c
B3LYP/ 6-31G(d)	In catechol isomer	0.440	-0.3726	2.24	3.23	0.170	17.11
	In catechol	0.416	-0.3600	1.64	2.39	0.154	15.07
6-31G(d,p)	In catechol isomer	0.418	-0.3683	2.27	3.23	0.164	16.60
	In catechol	0.393	-0.3541	1.65	2.39	0.149	14.56
6-311G(d,p)	In catechol isomer	0.443	-0.3918	2.27	3.33	0.164	17.54
	In catechol	0.417	-0.3776	1.66	2.36	0.147	15.31
6-31+G(d,p)	In catechol isomer	0.411	-0.3621	2.28	3.36	0.167	16.63
	In catechol	0.386	-0.3481	1.71	2.41	0.149	14.67
6-311+G(d,p)	In catechol isomer	0.438	-0.3867	2.31	3.29	0.168	17.67
	In catechol	0.411	-0.3721	1.71	2.36	0.149	15.51
6-311++G(d,p)	In catechol isomer	0.438	-0.3867	2.32	3.29	0.168	17.64
	In catechol	0.411	-0.3720	1.70	2.36	0.149	15.39
6-311+G(2d,p)	In catechol isomer	0.445	-0.3919	2.34	3.32	0.164	17.56
	In catechol	0.419	-0.3780	1.68	2.36	0.147	15.64
cc-pVDZ	In catechol isomer	0.400	-0.3376	2.29	3.24	0.168	16.44
	In catechol	0.379	-0.3255	1.71	2.36	0.154	14.51
PBE0/6-31G(d)	In catechol isomer	0.428	-0.3667	2.25	3.31	0.164	16.34
	In catechol	0.405	-0.3539	1.62	2.37	0.150	14.47
B3LYP/6- 31+G(2df,pd)	In catechol isomer	0.412	-0.3679	2.26	3.24	0.166	16.53
	In catechol	0.390	-0.3560	1.71	2.36	0.149	14.82

- Radius of oxygen atom was determined in the direction of the extension of C-O bond; radius of hydrogen atom was determined in the direction of the extension of O-H bond.
- The monomer (dimer) radius is the non-bonded (bonded) radius; the penetration derived from these is shown in Figure 41 as the monomer-dimer difference.
- Volume has been taken to the 0.001 au contour.

**Appendix C. Internal Coordinates, Total Energies and Free
Energies for Benchmark Molecules. Total Energy are Zero-
Point Energy Corrected (Refer to the Attached CD)**

**Appendix D. Total Energy, Free Energy and Configurations for
Model Ester Dimers and Trimers**

D1 Total Energy and Free Energy for (Poly)phenolic Lipid Dimers and Trimers

D1.1 Total Energy and Free Energy for (Poly)phenolic Lipid Dimers

Table D1. 1. 1 Total and Free Energies for Methyl Ester Dimers

		Total energy (au)	Free energy (au)
3-OH-Me	a	-1070.397085	-1070.473620
	b	-1070.383093	-1070.461719
	c	-1070.381732	-1070.459043
4-OH-Me	a	-1070.390778	-1070.469002
	b	-1070.385539	-1070.463797
3,4-OH-Me	a	-1220.829255	-1220.909631
	b	-1220.811592	-1220.895433
	c	-1220.810473	-1220.893907
	d	-1220.809114	-1220.888571
	e	-1220.808499	-1220.889033
3,5-OH-Me	a	-1220.819797	-1220.896846
	b	-1220.811656	-1220.891814
	c	-1220.804752	-1220.888854
	d	-1220.804225	-1220.887242
3,4,5-OH-Me	a	-1371.250546	-1371.336075
	b	-1371.233612	-1371.322259
	c	-1371.233562	-1371.317786
	d	-1371.233121	-1371.320928
	e	-1371.233024	-1371.319394
	f	-1371.232055	-1371.319622
	g	-1371.228907	-1371.313399
	h	-1371.227767	-1371.313174

Table D1. 1. 2 Total and Free Energies for Propyl Ester Dimers

		Total energy (au)	Free energy (au)
3-OH-Pr	a	-1227.543266	-1227.632759
	b	-1227.528940	-1227.621630
	c	-1227.527629	-1227.620193
4-OH-Pr	a	-1227.536706	-1227.630214
	b	-1227.531283	-1227.623488
3,4-OH-Pr	a	-1377.975366	-1378.069604
	b	-1377.957380	-1378.054831
	c	-1377.956201	-1378.052386
	d	-1377.954852	-1378.048229
	e	-1377.954216	-1378.049581
3,5-OH-Pr	a	-1377.965162	-1378.061310
	b	-1377.957725	-1378.052541
	c	-1377.950599	-1378.048425
	d	-1377.950214	-1378.047352
3,4,5-OH-Pr	a	-1528.396809	-1528.497198
	b	-1528.379491	-1528.478145
	c	-1528.379478	-1528.483607
	d	-1528.379080	-1528.481446
	e	-1528.378711	-1528.479232
	f	-1528.377810	-1528.479959
	g	-1528.374799	-1528.473610
	h	-1528.373574	-1528.473455

Table D1. 1. 3 Total and Free Energies for Hexyl Ester Dimers

		Total energy (au)	Free energy (au)
3-OH-Hex	a	-1463.246642	-1463.353629
	b	-1463.231313	-1463.344168
	c	-1463.229426	-1463.342430
4-OH-Hex	a	-1463.239191	-1463.351931
	b	-1463.233766	-1463.347100
3,4-OH-Hex	a	-1613.677881	-1613.792769
	b	-1613.659807	-1613.778595
	c	-1613.658645	-1613.776073
	d	-1613.658256	-1613.769770
	e	-1613.656789	-1613.772911
3,5-OH-Hex	a	-1613.667578	-1613.783573
	b	-1613.660142	-1613.775568
	c	-1613.653125	-1613.772770
	d	-1613.652806	-1613.770587
3,4,5-OH-Hex	a	-1764.099175	-1764.219693
	b	-1764.081988	-1764.202315
	c	-1764.081937	-1764.205916
	d	-1764.081604	-1764.203669
	e	-1764.080891	-1764.203740
	f	-1764.080308	-1764.203430
	g	-1764.077208	-1764.195738
	h	-1764.076057	-1764.196489

D1.2 Total Energy and Free Energy for (Poly)phenolic Lipid Trimers

Table D1. 2. 1 Total and Free Energies for Methyl Ester Trimers

		Total energy (au)	Free energy (au)
3-OH-Me	a	-1605.596485	-1605.701765
	b	-1605.585490	-1605.694413
	c	-1605.583871	-1605.691987
4-OH-Me	a	-1605.590754	-1605.698908
	b	-1605.590587	-1605.698199
	c	-1605.584249	-1605.694410
3,4-OH-Me	a	-1831.227186	-1831.341471
	b	-1831.225612	-1831.339490
	c	-1831.222999	-1831.341641
	d	-1831.221924	-1831.336322
	e	-1831.220757	-1831.332106
3,5-OH-Me	a	-1831.236577	-1831.341692
	b	-1831.211893	-1831.330565
	c	-1831.210987	-1831.328079
3,4,5-OH-Me	a	-2056.866084	-2056.977046
	b	-2056.865428	-2056.979099
	c	-2056.863233	-2056.982653
	d	-2056.861196	-2056.972775
	e	-2056.858791	-2056.982416
	f	-2056.856320	-2056.983393
	g	-2056.855406	-2056.980742
	h	-2056.853563	-2056.975960

Table D1. 2. 2 Total and Free Energies for Propyl Ester Trimers

		Total energy (au)	Free energy (au)
3-OH-Pr	a	-1841.315486	-1841.442053
	b	-1841.304241	-1841.433951
	c	-1841.300375	-1841.431821
4-OH-Pr	a	-1841.309396	-1841.438386
	b	-1841.309215	-1841.438607
	c	-1841.303601	-1841.431695
3,4-OH-Pr	a	-2066.945276	-2067.080730
	b	-2066.944253	-2067.078244
	c	-2066.941743	-2067.081972
	d	-2066.940553	-2067.076351
	e	-2066.939459	-2067.072431
3,5-OH-Pr	a	-2066.956104	-2067.081797
	b	-2066.930649	-2067.071929
	c	-2066.929895	-2067.067837
3,4,5-OH-Pr	a	-2292.585306	-2292.717750
	b	-2292.584370	-2292.719755
	c	-2292.582665	-2292.720812
	d	-2292.580063	-2292.713052
	e	-2292.575063	-2292.723895
	f	-2292.574383	-2292.719341
	g	-2292.572221	-2292.716237

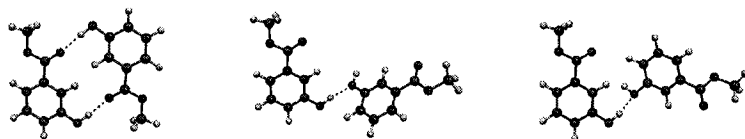
Table D1. 2. 3 Total and Free Energies for Hexyl Ester Trimers

		Total energy (au) (not zero-point energy corrected)
3-OH-Hex	a	-2195.799869
	b	-2195.788060
	c	-2195.783933
4-OH-Hex	a	-2195.793648
	b	-2195.793351
	c	-2195.786426
3,4-OH-Hex	a	-2421.445162
	b	-2421.443740
	c	-2421.442064
	d	-2421.440480
3,5-OH-Hex	a	-2421.456596
	b	-2421.430011
	c	-2421.429199
3,4,5-OH-Hex	a	-2647.101794
	b	-2647.100441
	c	-2647.097292
	d	-2647.093211
	e	-2647.090073
	f	-2647.087156

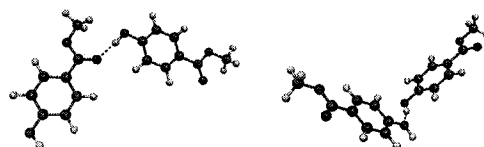
D2 Dimers Configurations

D1.1 Methyl Esters

D1.1.1 Methyl Esters with One Hydroxyl Group

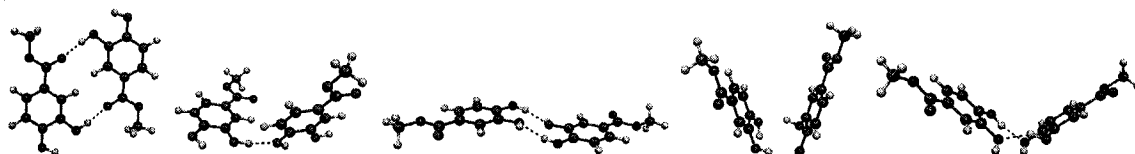


	a	b	c
ΔE	0	+8.8	+9.6
ΔG	0	+7.5	+9.1

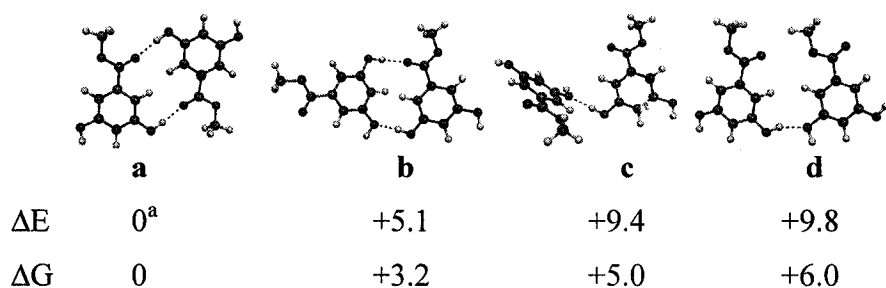


	a	b
ΔE	0	+3.3
ΔG	0	+3.3

D1.1.2 Methyl Esters with Two Hydroxyl Groups

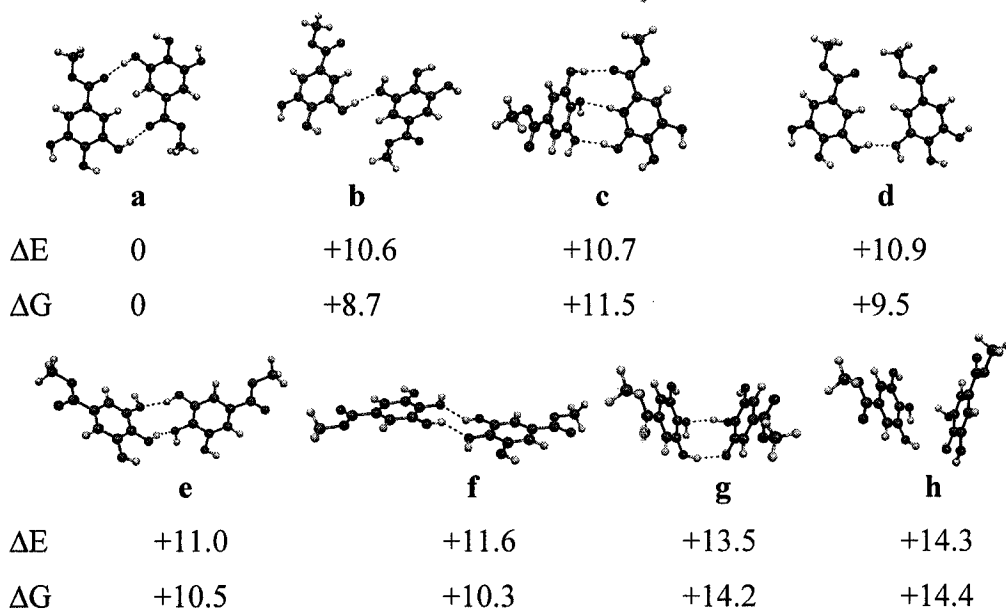


	a	b	c	d	e
ΔE	0	+11.1	+11.8	+12.6	+13.0
ΔG	0	+8.9	+9.9	+13.2	+12.9



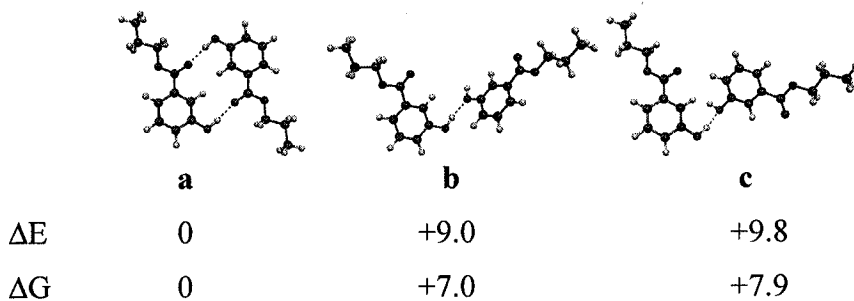
a. Imaginary frequency -3 cm^{-1} , wagging of the whole dimer.

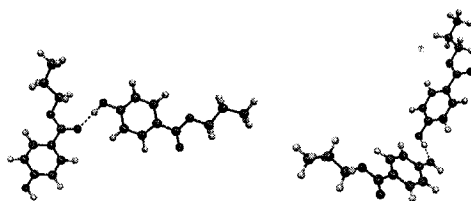
D1.1.3 Methyl Esters with Three Hydroxyl groups



D1.2 Propyl Esters

D1.2.1 Propyl Esters with One Hydroxyl Group



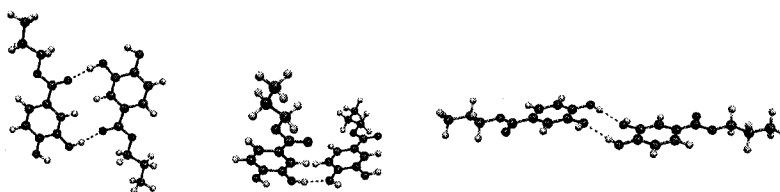


a

b

ΔE	0	+3.4
ΔG	0	+4.2

D1.2.2 Propyl Esters with Two Hydroxyl Groups

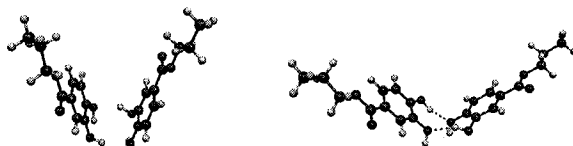


a

b

c

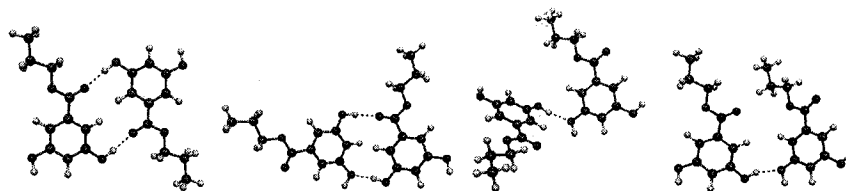
ΔE	0	+11.3	+12.0
ΔG	0	+9.3	+10.8



d

e

ΔE	+12.9	+13.3
ΔG	+13.4	+12.6



a

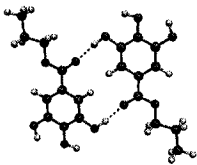
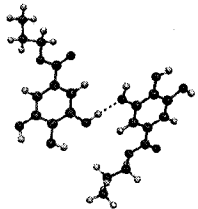
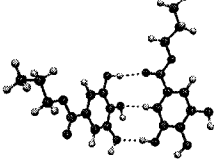
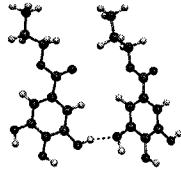
b

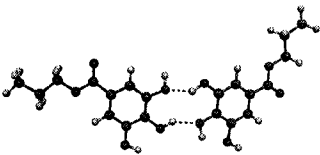
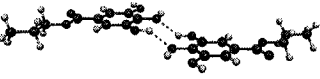
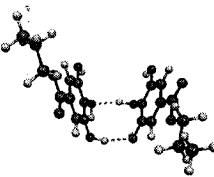
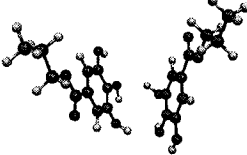
c

d

ΔE	0	+4.7	+9.1	+9.4
ΔG	0	+5.5	+8.1	+8.8

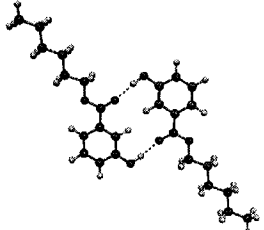
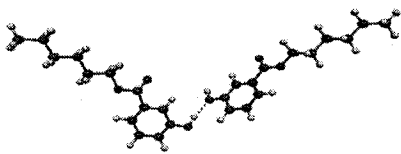
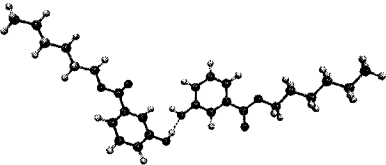
D1.2.3 Propyl Esters with Three Hydroxyl Groups

							
a		b		c		d	
ΔE	0		+10.9		+10.9		+11.1
ΔG	0		+8.5		+12.0		+9.9

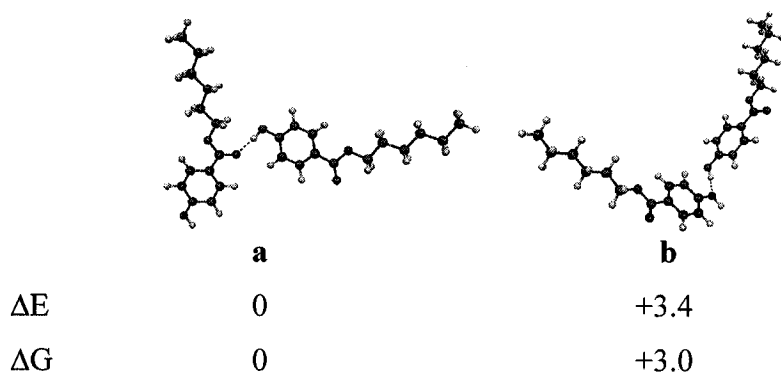
							
e		f		g		h	
ΔE	+11.6		+11.9		+13.8		+14.6
ΔG	+10.7		+10.8		+14.8		+14.9

D1.3 Hexyl Esters

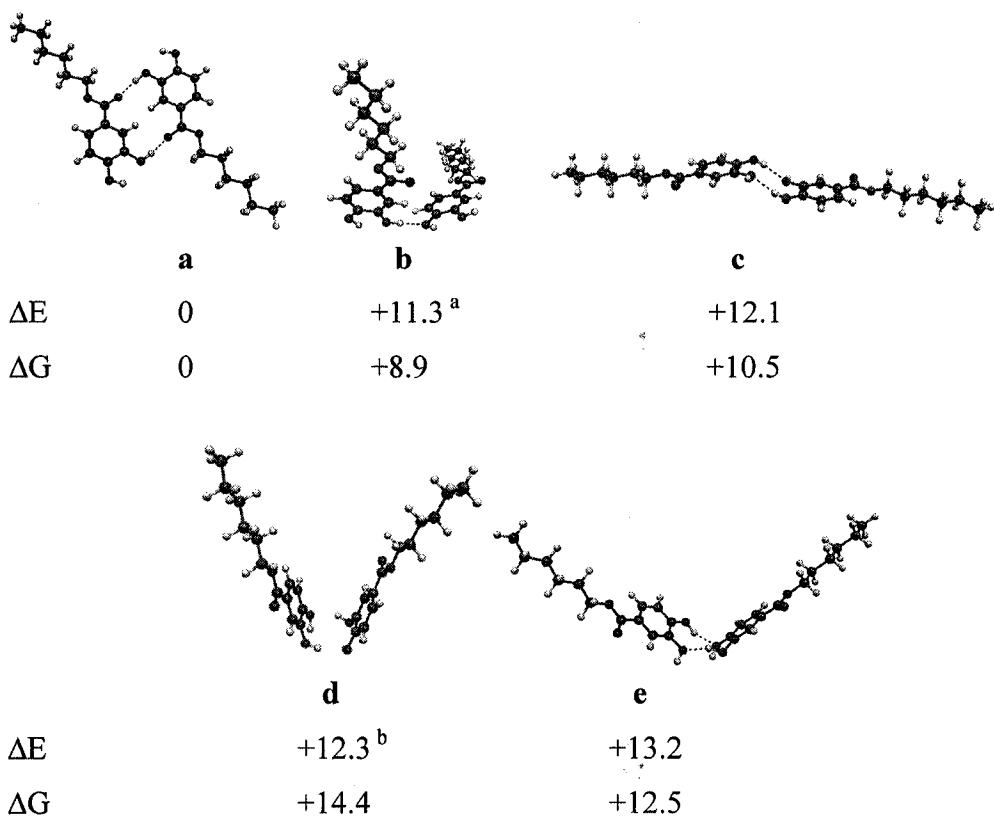
D1.3.1 Hexyl Esters with One Hydroxyl Group

					
a		b		c	
ΔE	0 ^a		+9.6		+10.8
ΔG	0		+5.9		+7.0

a. Imaginary frequency -4 cm^{-1} , folding of the two monomers.

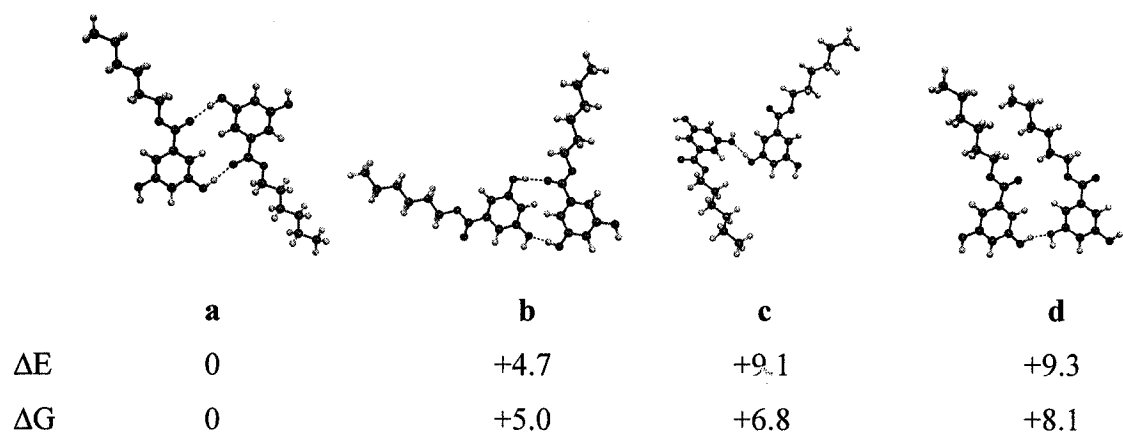


D1.3.2 Hexyl Esters with Two Hydroxyl Groups

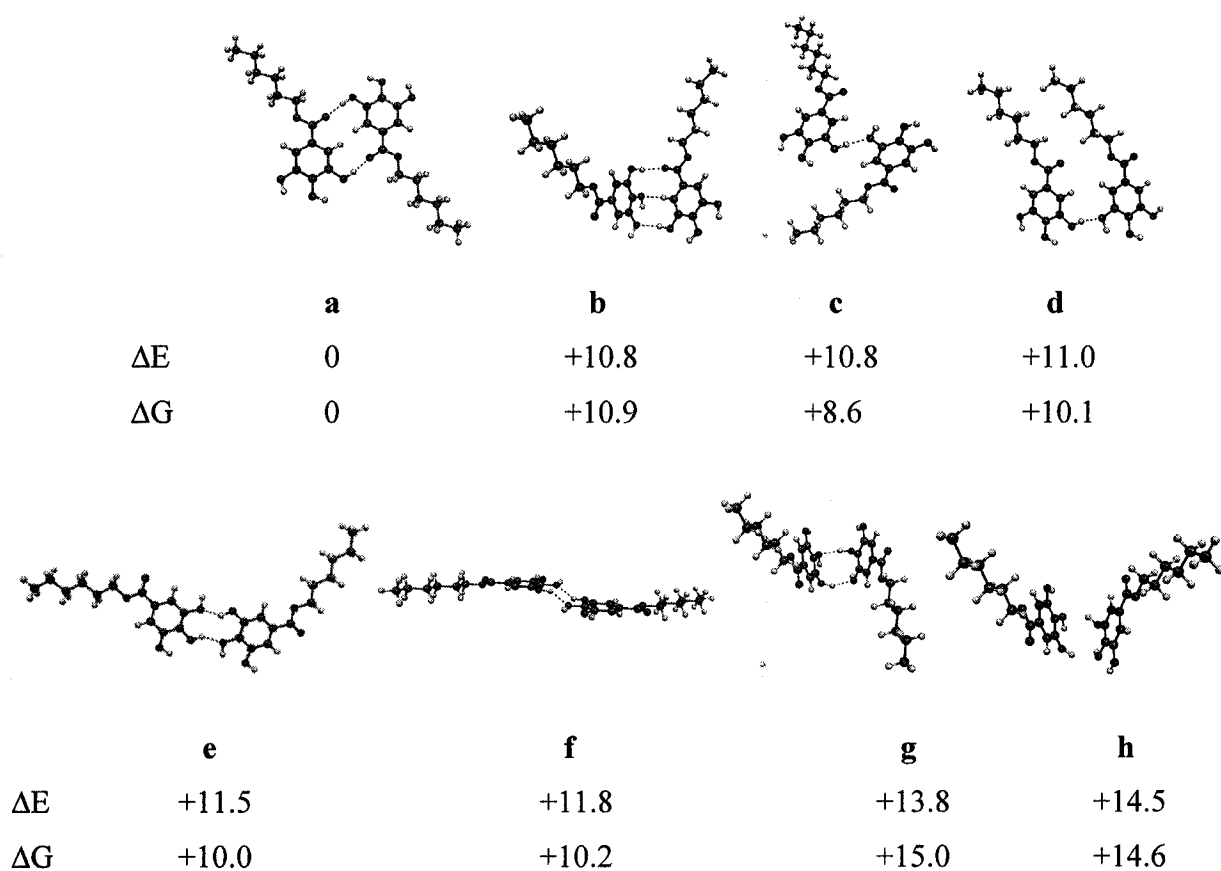


a. Imaginary frequency -5 cm^{-1} , wobbling of the two monomers.

b. Imaginary frequency -2 cm^{-1} , wobbling of the two monomers.



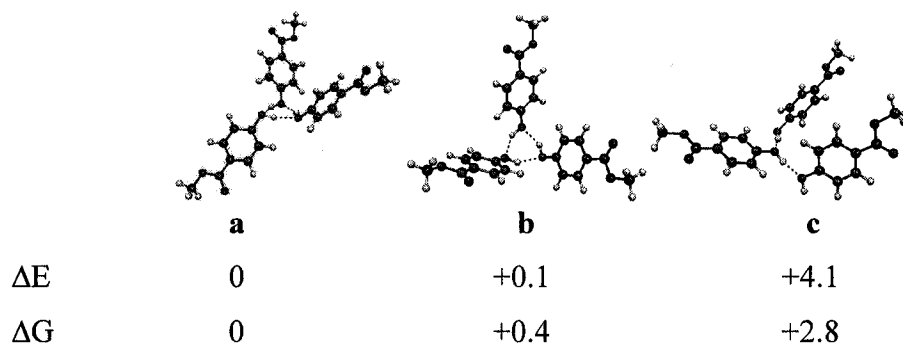
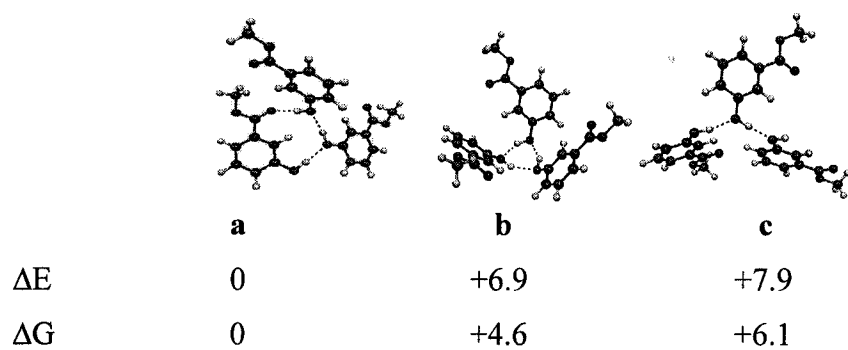
D1.3.3 Hexyl Esters with Three Hydroxyl Groups



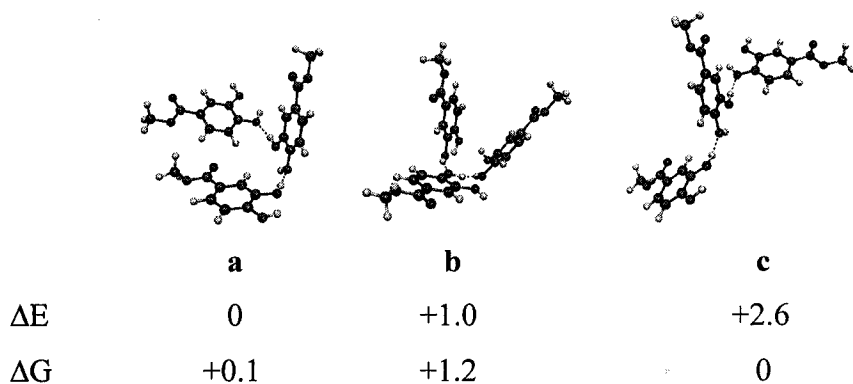
D2 Trimers

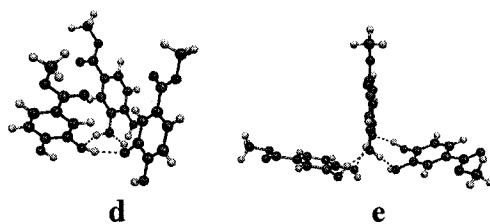
D2.1 Methyl Esters

D2.1.1 Methyl Esters with One Hydroxyl Group

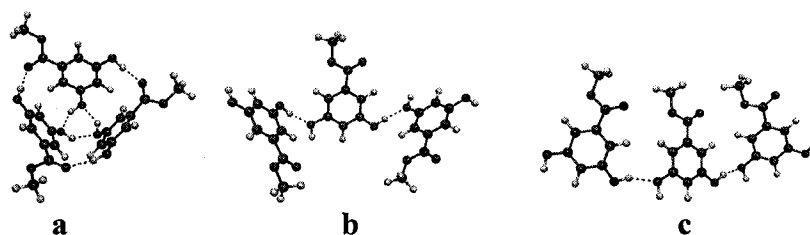


D2.1.2 Methyl Esters with Two Hydroxyl Groups



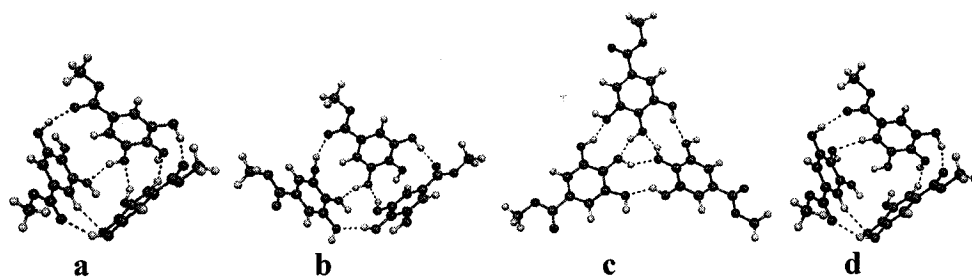


ΔE	+3.3	+4.0
ΔG	+3.3	+5.9

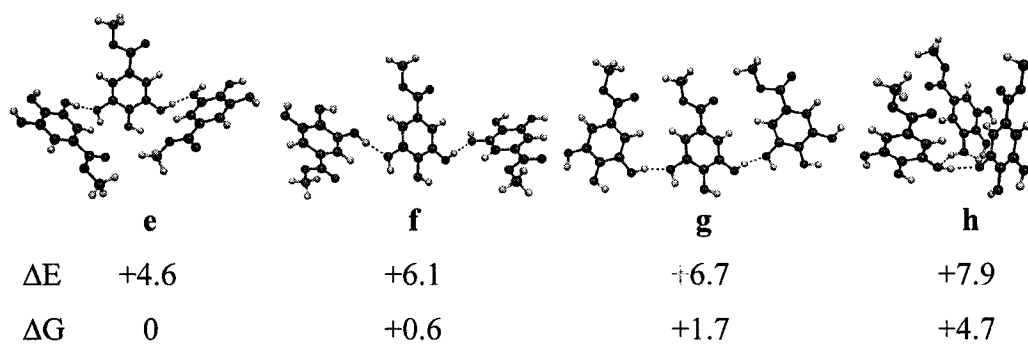


ΔE	0	+15.5	+16.1
ΔG	0	+7.0	+8.5

D2.1.3 Methyl Esters with Three Hydroxyl Groups

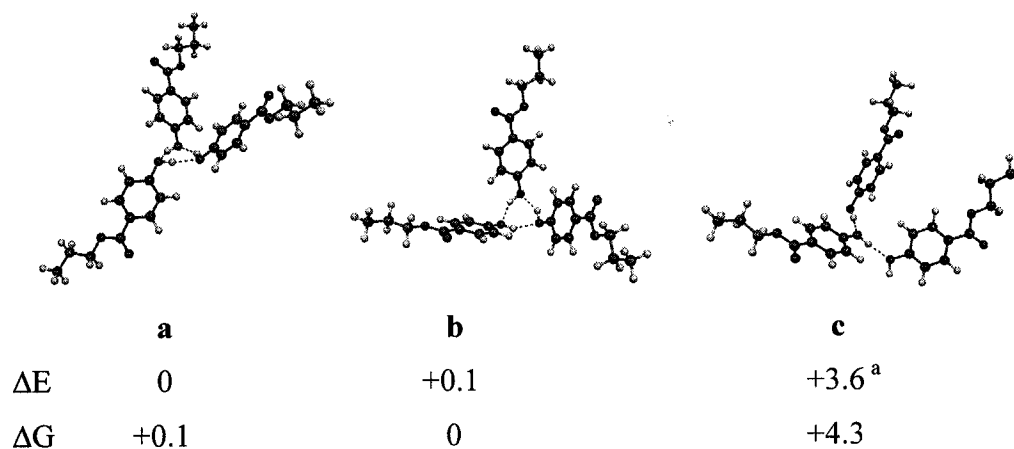
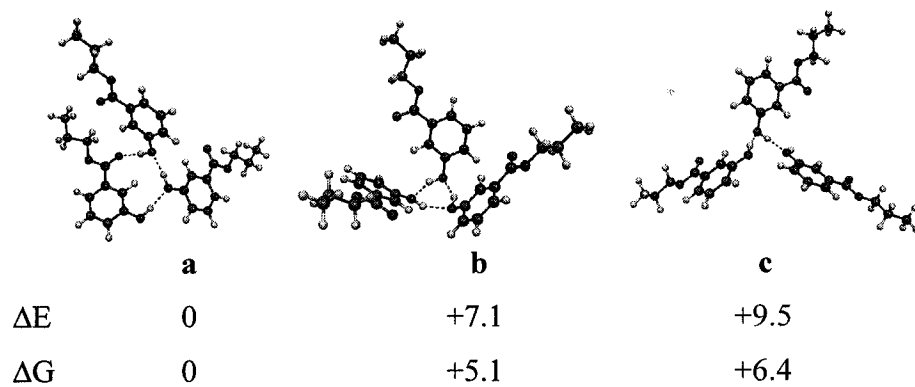


ΔE	0	+0.4	+1.8	+3.1
ΔG	+4.0	+2.7	+0.5	+6.7



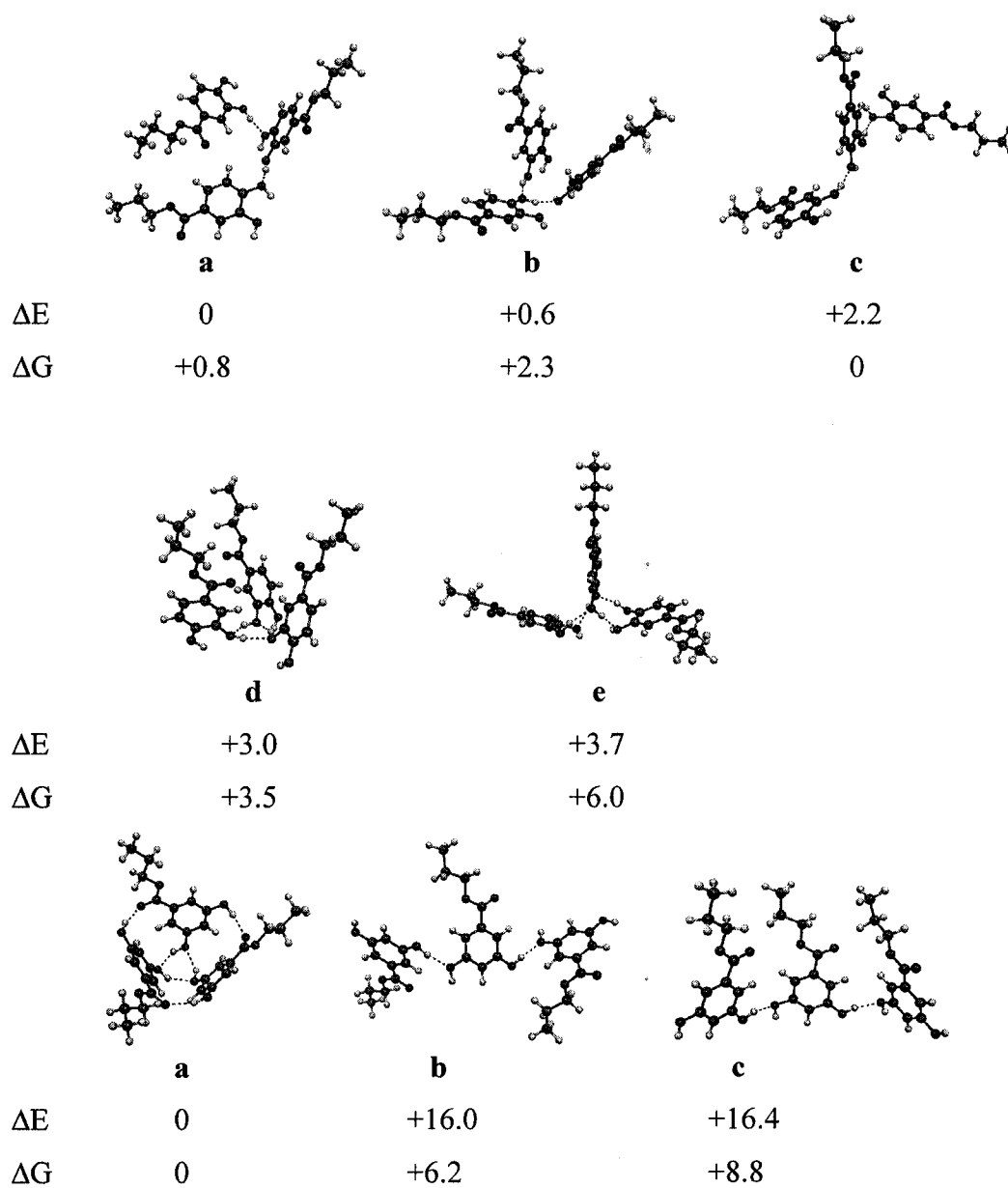
D2.2 Propyl Esters

D2.2.1 Propyl Esters with One Hydroxyl Group

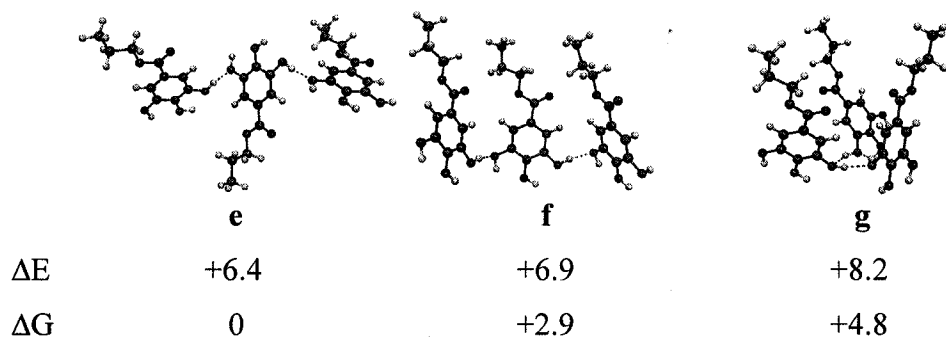
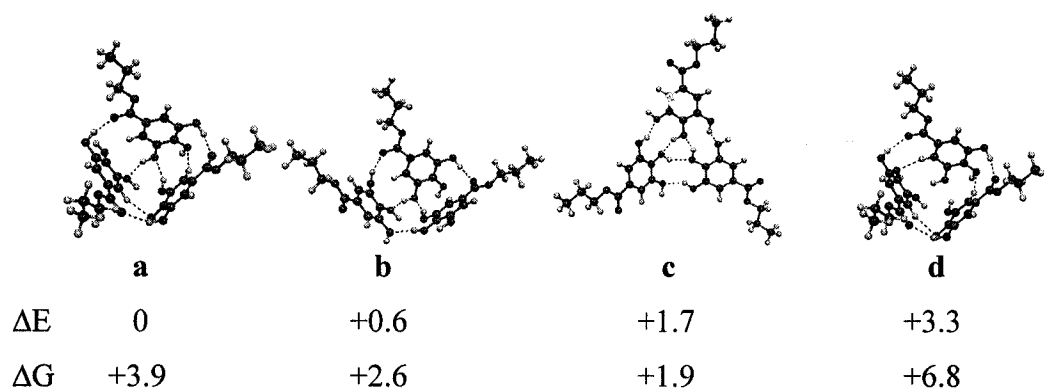


a. Imaginary frequency of -2 cm^{-1} , rotation of one monomer.

D2.2.2 Propyl Esters with Two Hydroxyl Groups

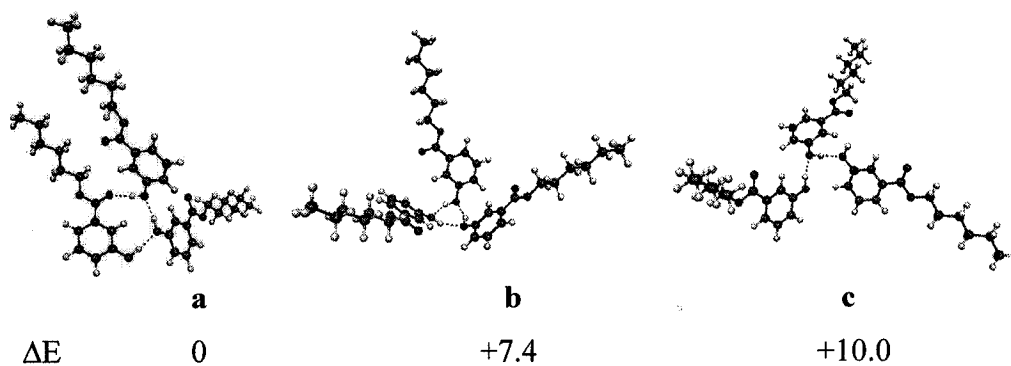


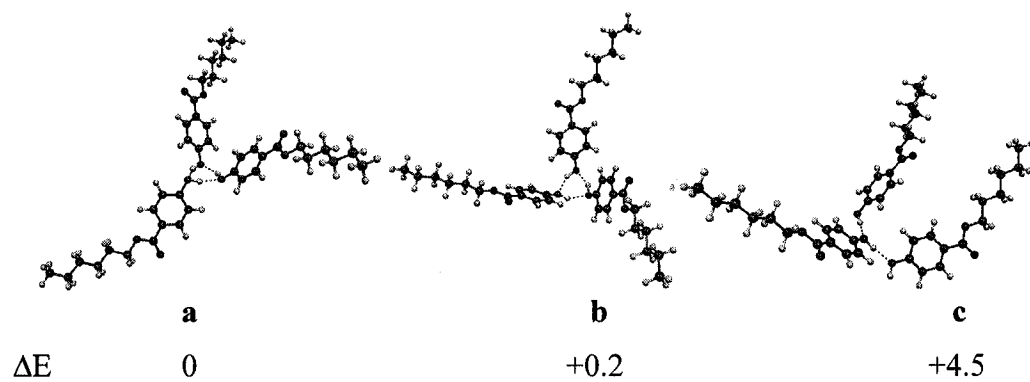
D2.2.3 Propyl Esters with Three Hydroxyl Groups



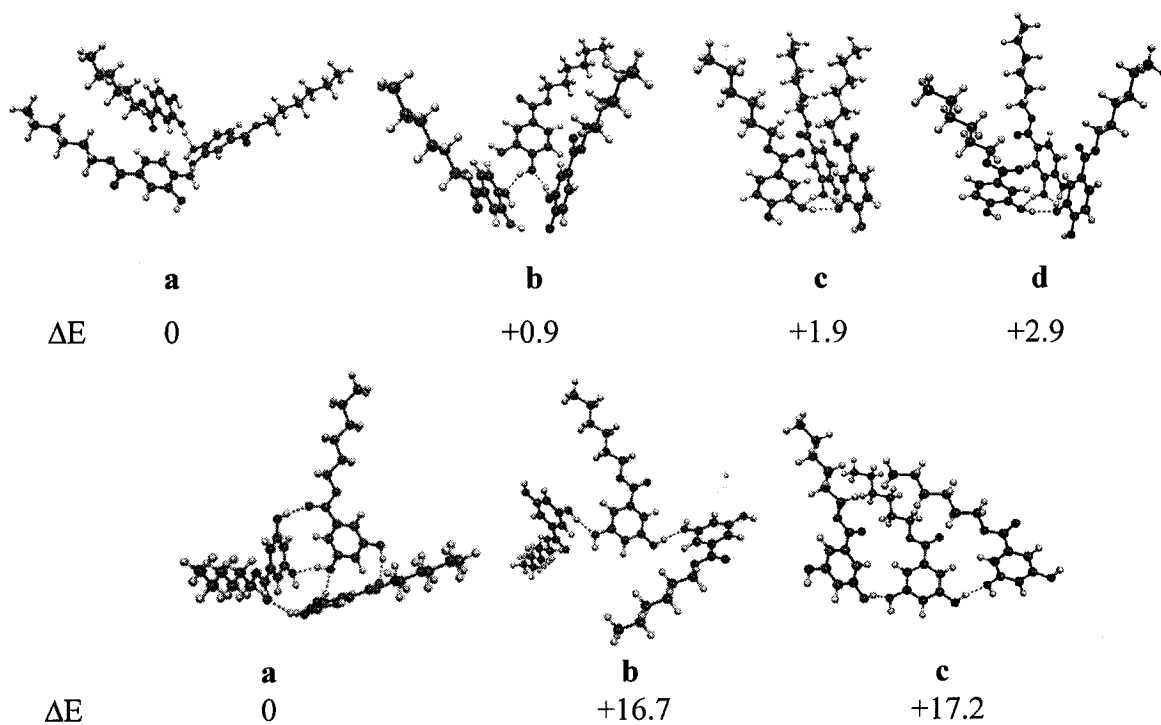
D2.3 Hexyl Esters

D2.3.1 Hexyl Esters with One Hydroxyl Group

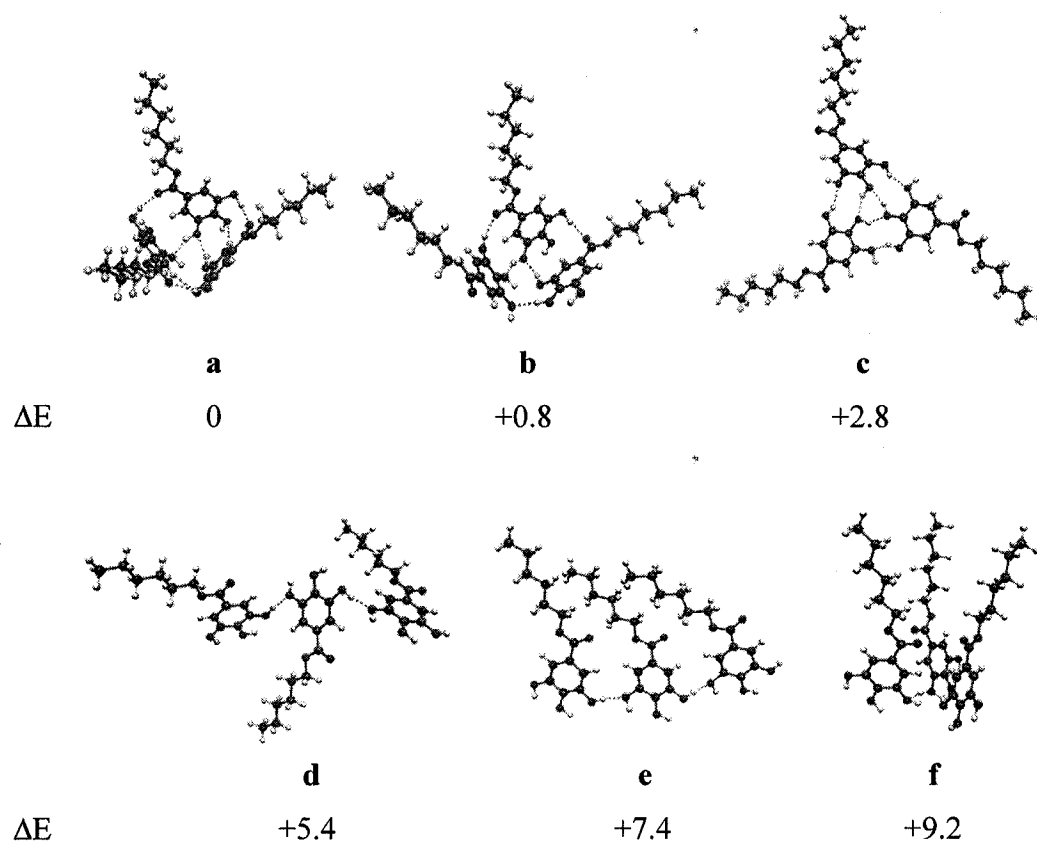




D2.3.2 Hexyl Esters with Two Hydroxyl Groups



D2.3.3 Hexyl Esters with Three Hydroxyl Groups



**Appendix E. Z-Matrix Files for Dimers and Trimers for Model
Esters. All Total and Free Energies are in Kcal/mol (Refer to
the Attached CD)**

**Appendix F. Sample Calculation of the Energy Cost to Erect
the Side Chains for the Phenolic Lipids**

Take the isotherm of DPGG in Figure 9 as an example, the isotherm started to lift-off when the surface area was 50 \AA^2 per molecule, and the isotherm collapse when the surface area is 38 \AA^2 per molecule at surface pressure of 45 mN m^{-1} . According to the energy calculation equation of monolayers:

$$E = \pi \times A$$

therefore,

$$\Delta E = \Delta \pi \times \Delta A$$

$$= (45 \text{ mN m}^{-1} - 0 \text{ mN m}^{-1}) \times (50 \text{ \AA}^2 \text{ per molecule} - 38 \text{ \AA}^2 \text{ per molecule})$$

$$\times 6.02 \times 10^{23} \text{ molecules mol}^{-1}$$

$$= 3250 \text{ N mol}^{-1}$$

$$= 0.7 \text{ kcal mol}^{-1}$$